

REPORT DOCUMENTATION PAGE				Form Approved OMB No. 0704-0188							
Public reporting burden for this collection of information is estimated to average 1 hour per response, including the time for reviewing instructions, searching data sources, gathering and maintaining the data needed, and completing and reviewing the collection of information. Send comments regarding this burden estimate or any other aspect of this collection of information, including suggestions for reducing this burden to Washington Headquarters Service, Directorate for Information Operations and Reports, 1215 Jefferson Davis Highway, Suite 1204, Arlington, VA 22202-4302, and to the Office of Management and Budget, Paperwork Reduction Project (0704-0188), Washington, DC 20503. PLEASE DO NOT RETURN YOUR FORM TO THE ABOVE ADDRESS.											
1. REPORT DATE (DD-MM-YYYY) 3/21/2011		2. REPORT TYPE Final Report		3. DATES COVERED (From - To) 5/1/2005 - 12/31/2010							
4. TITLE AND SUBTITLE Shallow Water Acoustic Experiments and Preliminary Planning for FY06 Fieldwork				5a. CONTRACT NUMBERS N/A 5b. GRANT NUMBER N00014-04-1-0146 5c. PROGRAM ELEMENT NUMBER N/A							
6. AUTHOR(S) James F. Lynch				5d. PROJECT NUMBER 130146SP 5e. TASK NUMBER N/A 5f. WORK UNIT NUMBER N/A							
7. PERFORMING ORGANIZATION NAME(S) AND ADDRESS(ES) Woods Hole Oceanographic Institution 98 Water Street, MS-11 Woods Hole, MA 02543				8. PERFORMING ORGANIZATION REPORT NUMBER N/A							
9. SPONSORING/MONITORING AGENCY NAME(S) AND ADDRESS(ES) Office of Naval Research (ONR) CODE 3210A One Liberty Center, RM 1076 675 North Randolph Street Arlington, VA 22203-1995				10. SPONSORING/MONITORING ACRONYM(S) N/A 11. SPONSORING/MONITORING AGENCY REPORT NUMBER N/A							
12. DISTRIBUTION/AVAILABILITY STATEMENT Approved for public release; distribution is unlimited											
13. SUPPLEMENTARY NOTES None											
14. ABSTRACT As a result of work on this proposal and the subsequent SW06 experiment, the following papers have been published to date (see attached).											
15. SUBJECT TERMS Shallow Water Acoustics; Oceanography; Coastal Processes											
16. SECURITY CLASSIFICATION OF: <table border="1" style="width: 100%; border-collapse: collapse;"> <tr> <td style="width: 33%; padding: 2px;">a. REPORT</td> <td style="width: 33%; padding: 2px;">b. ABSTRACT</td> <td style="width: 33%; padding: 2px;">c. THIS PAGE</td> </tr> <tr> <td style="text-align: center; padding: 2px;">U</td> <td style="text-align: center; padding: 2px;">U</td> <td style="text-align: center; padding: 2px;">U</td> </tr> </table>			a. REPORT	b. ABSTRACT	c. THIS PAGE	U	U	U	17. LIMITATION OF ABSTRACT U		16. NUMBER OF PAGES
a. REPORT	b. ABSTRACT	c. THIS PAGE									
U	U	U									
19a. NAME OF RESPONSIBLE PERSON Dr. James F. Lynch			19 b. TELEPHONE NUMBER (Include area code) 508-289-2230								

20110324066

- [1] D.J. Tang, J. Moum, J. Lynch, P. Abbot, R. Chapman, P. Dahl, G. Gawarkiewicz, S. Glenn, J. Goff, H. Graber, J. Kemp, A. Maffei, J. Nash, A. Newhall, "Shallow water '06 – a joint acoustic propagation/nonlinear internal wave physics experiment", *Oceanography*, 20 (4), 156-167 (2007).
- [2] J.M. Collis, T.F. Duda, J.F. Lynch, and H.A. DeFerrari, "Observed limiting cases of horizontal field coherence and array performance in a time-varying internal wavefield," *JASA-EL*, 124 (3), EL97-EL103 (2008).
- [3] B. Katsnelson, V. Grigorev, J.F. Lynch, and D. Tang, "Intensity fluctuations of mid-frequency sound signals passing through moving nonlinear internal waves," *JASA-EL*, 124(3), EL78-84 (2008).
- [4] J. Luo, M. Badiey, E.A. Karjadi, B. Katsnelson, A. Tskhoidze, J.F. Lynch, and J.N. Moum, "Observation of sound focusing and defocusing due to propagating nonlinear internal waves," *JASA-EL* 124 (3), EL66-EL72 (2008).
- [5] G.R. Potty, J.H. Miller, P.S. Wilson, J. F. Lynch, and A. Newhall, "Geoacoustic inversion using combusive sound source signals," *JASA-EL* 124 (3), EL146-EL150 (2008).
- [6] H. DeFerrari, J. Lynch and A. Newhall, "Temporal coherence of mode arrivals," *JASA-EL* 124(3), EL 104-EL109 (2008)
- [7] J. Lynch and D.J. Tang, "Overview of Shallow Water 2006 JASA-EL Special Issue Papers," *JASA-EL* 124(3), EL 63-EL65 (2008).
- [8] Y.T. Lin, T.F. Duda, and J.F. Lynch, "Acoustic mode radiation from the termination of a truncated nonlinear internal gravity wave duct in a shallow ocean area", *J. Acoust. Soc. Am.* 124 (4), pp. 1752-1765 (2009).
- [9] J. Lynch, Y.T. Lin, T.F. Duda, and A.E. Newhall, "Acoustic ducting, reflection, refraction, and dispersion by curved nonlinear internal waves in shallow water", *IEEE J. Oceanic Eng'g.* 35(1), pp. 12-27 (2010)
- [10] Song, A.J., M. Badiey, A.E. Newhall, J.F. Lynch, H.A. Deferrari, B. Katsnelson, "Passive time reversal acoustic communications through shallow water internal waves", in press *IEEE J. Ocean. Eng.* (2010.)

- [11] B. Katznelson, J. Lynch and A. Tsoidze, "Space-frequency distribution of sound field intensity in the vicinity of the temperature front in shallow water", *Acoustical Physics*, 53(5), 611-617 (2007).
- [12] Badiy, M., B.G. Katznelson, Y.T. Lin, and J.F. Lynch, "Horizontal Lloyd's mirror effect due to the interaction between acoustic waves and nonlinear internal waves." In press, *JASA-EL*. (2011.)

Acoustic mode radiation from the termination of a truncated nonlinear internal gravity wave duct in a shallow ocean area

Ying-Tsong Lin, Timothy F. Duda, and James F. Lynch

Department of Applied Ocean Physics and Engineering, Woods Hole Oceanographic Institution, Woods Hole, Massachusetts 02543

(Received 26 January 2009; revised 20 June 2009; accepted 8 July 2009)

Horizontal ducting of sound between short-wavelength nonlinear internal gravity waves in coastal environments has been reported in many theoretical and experimental studies. Important consequences arising at the open end of an internal wave duct (the termination) are examined in this paper with three-dimensional normal mode theory and parabolic approximation modeling. For an acoustic source located in such a duct and sufficiently far from the termination, some of the propagating sound may exit the duct by penetrating the waves at high grazing angles, but a fair amount of the sound energy is still trapped in the duct and propagates toward the termination. Analysis here shows that the across-duct sound energy distribution at the termination is unique for each acoustic vertical mode, and as a result the sound radiating from the termination of the duct forms horizontal beams that are different for each mode. In addition to narrowband analysis, a broadband simulation is made for water depths of order 80 m and propagation distances of 24 km. Situations occur with one or more modes absent in the radiated field and with mode multipath in the impulse response. These are both consistent with field observations.

© 2009 Acoustical Society of America. [DOI: 10.1121/1.3203268]

PACS number(s): 43.30.Re, 43.20.Bi, 43.20.Mv, 43.30.Bp [JAC]

Pages: 1752–1765

I. INTRODUCTION

Theoretical and experimental studies have revealed that propagating sound can be trapped and ducted between pairs of nonlinear internal waves of depression commonly observed in coastal areas. Here, we examine what happens when such a duct gradually or abruptly relaxes to the background conditions and the sound exits the duct. The horizontal ducting of sound between internal waves can be understood in terms of the horizontal rays of acoustic vertical modes bending and focusing in the duct, or by spiraling rays. Katsnel'son and Pereselkov¹ theoretically studied the effect using the theory of "horizontal rays and vertical modes."² Another study by Oba and Finette³ which included results obtained with a computer code for three-dimensional (3D) sound propagation, FOR3D,⁴ also predicted this ducting phenomenon. In another of their papers,⁵ these investigators numerically investigated the consequences of this effect on horizontal array beamforming and also performed a modal decomposition of the sound field to explain its structure in the duct. Observations by Badiey *et al.*⁶ and Franks *et al.*⁷ from the SWARM'95 experiment off New Jersey confirmed these predictions. Typical internal wave packets capable of causing this effect have inter-wave distances of 300–1000 m and modal refractive index anomalies of a few tenths of a percent to 3%.⁸

Work to date has addressed these internal wave ducts as "infinite length pipelines" for sound, i.e., the internal wave crests are straight and endless. However, this is not the case in the real world. Many satellite and *in-situ* observations have shown internal wave packets (ducts) to be finite and localized, having total along-crest lengths as short as a few kilometers near an internal wave source region.⁹ Prior work

does not address what happens to internal-wave ducted sound when the duct terminates in the horizontal and the sound is emitted. The goal of this paper is to investigate this radiation from the duct termination. Analytical and numerical approaches are taken. In the analytical approach, an idealized internal-wave shape (square waveform) and the assumption of adiabatic mode propagation give a 3D normal mode solution for the sound field in the duct. Then Huygens' principle is adopted to calculate the radiation field. As for the numerical approach, a computer code¹⁰ implementing a 3D parabolic approximation in Cartesian coordinates is employed to calculate the acoustic field and broadband impulses within and emitted from a duct. The use of this 3D parabolic approximation model allows more complicated (or more realistic) internal-wave shapes. Also, since this numerical model allows mode coupling, it can be used to verify the adiabatic mode assumption used in the analytical computation.

Both the analytical and numerical computations show horizontal interference patterns within the duct. Richly detailed sound radiation fields are predicted at locations far from the termination of a truncated internal wave duct, having mode-dependent patterns with strong azimuthal and temporal variability. Thus, effects of ducting are found at locations with no evidence of a ducting condition. Similar radiation effects were found in the data collected in the SW06 shallow water acoustic experiment.¹¹ Though we will not completely prove it in this paper (as this involves other analyses which are future work), the results shown here make a plausible explanation for at least some of the data variability measured in the field. As examples, the tempo-

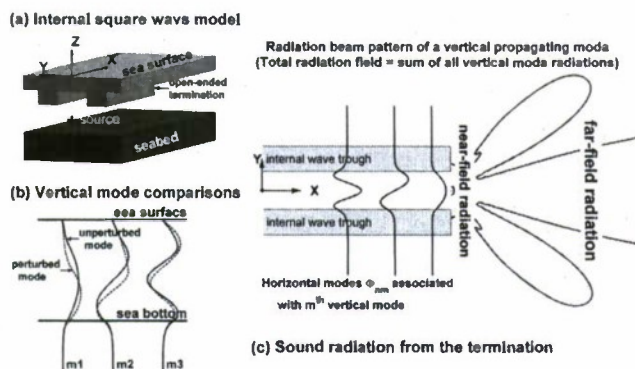


FIG. 1. Simplified internal-wave duct model used for theoretical analysis. (a) Internal waves of depression with square waveforms and parallel wavefronts are considered. The waves abruptly terminate to the background state. (b) Comparisons of acoustic vertical modes before and after being perturbed by the internal-square wave. (c) A depiction of sound radiation from the termination. Total radiation field equals to the sum of all vertical mode radiations.

rally varying modal contents of sound and mode multipath were observed and compare well qualitatively with the predictions made here.

The contents of this paper are as follows: Sec. II contains the derivation and evaluation of a 3D normal mode solution for an idealized environment. Section III contains a numerical parabolic equation solution for a more complex environment. Section IV contains field observation of the effects similar to those predicted by the theory. Section V has a discussion and Sec. VI contains a summary.

II. NORMAL MODE SOLUTION

The horizontal ducting of acoustic energy between internal waves can lead to a rather complicated horizontal eigenvalue problem if realistic detailed shapes of the internal waves that form the duct are considered. Also, the sound radiation from a real, irregular duct termination is not simple to handle by a theoretical means. So, rather than addressing a complicated case, we will begin with a simple duct model which will still retain most of the physics associated with the ducting and radiation effects. The detailed model configuration is provided below, along with the explanations for two assumptions used in deriving the normal mode solution.

A. Simplified physical model and assumptions

The model used for the theoretical analysis has two homogeneous water column layers bounded below by a homogeneous bottom, as shown in Fig. 1(a). The sound speed in the upper water column layer is slightly faster, and sound absorption is neglected in both the water column layers, but is included in the bottom. Two internal waves of depression are introduced by deepening the interface between the two aqueous layers from the ambient state to a perturbed state. Simplified internal waves with square and equal waveforms in the y direction, equal perturbation amplitudes, and parallel wave crests along the x -axis are used, forming an acoustic duct with slow normal velocity in the center, as will be shown. The waves abruptly terminate at a selected location in the x direction, forming an open end of the duct. Although

the acoustic horizontal ducting modes in this square-wave approximate model may differ from the ones seen in realistic cases, the physical characteristics of these ducting modes can still be captured in the approximate model. In addition, if it is required, one can more carefully design an internal square-wave model to fit a realistic waveform such that the resultant horizontal ducting modes are comparable to the realistic ones. The coordinate origin of the Cartesian coordinate system is placed in the middle between the internal waves on the sea surface. The z axis is positive upward. At x locations less than termination position $x=L$ solutions valid in a ducted environment will be found. At $x>L$ solutions in a homogeneous layered environment will be computed using Huygens' principle, which is done by employing the Green's function method.

For the theoretical analysis, we make two following assumptions about sound propagation. (1) Mode propagation is adiabatic, with no energy exchange between modes. This assumption would be invalid if the addressed problem was sound propagation across the internal waves.^{12,13} (2) Total transmission at the open-ended termination is assumed so that no sound energy is reflected back into the duct. This is justified by the fact that the termination width normal to the duct (300–1000 m across in a common situation) is very large compared to the underwater acoustic wavelength of frequencies greater than 50 Hz, which produces a large ka value (acoustic wavenumber multiplying the gap aperture) and thus should yield only tiny reflected sound by analogy with the unflanged, open pipe problem.¹⁴ A final caution should be made here: for high grazing-angle penetration (at x near that of the source) the assumption of adiabatic mode propagation is violated, and the solution in terms of the resultant mode sum is not strictly correct. The horizontal leaky modes are included in the following derivation, but they only describe the barrier penetration and tunneling effect that occurs when the trapped sound strikes the internal waves at low grazing angle and radiates out of the duct in the y direction.

B. Derivation of an analytical solution

The sound pressure field excited by a harmonic point source located at (x_s, y_s, z_s) in the physical model described above is governed by the inhomogeneous 3D Helmholtz equation with a Dirac delta source function

$$\rho(z) \nabla \cdot \left(\frac{1}{\rho(z)} \nabla P(x, y, z) \right) + \frac{\omega^2}{c^2(x, y, z)} P(x, y, z) = -4\pi \delta(x - x_s) \delta(y - y_s) \delta(z - z_s), \quad (1)$$

where $c(x, y, z)$ is the medium sound speed (this is a complex number with imaginary component enumerating absorption), $\rho(z)$ is the medium density (its horizontal variations are neglected), and $\omega = 2\pi f$ is the acoustic frequency (f enumerates this in Hertz). To solve Eq. (1), begin with a vertical mode decomposition of the sound field

$$P(x, y, z) = \sum_m \Gamma_m(x, y) \Psi_m(x, y, z), \quad (2)$$

where $\Gamma_m(x, y)$ is the (complex) mode amplitude and $\Psi_m(x, y, z)$ is the m th vertical normal mode at (x, y) that

satisfies the following local mode equation with appropriate boundary conditions on the sea surface and the bottom:

$$\rho(z) \frac{d}{dz} \left(\frac{1}{\rho(z)} \frac{d}{dz} \Psi_m(x, y, z) \right) + \left(\frac{\omega^2}{c^2(x, y, z)} - \zeta_m^2(x, y) \right) \Psi_m(x, y, z) = 0, \quad (3)$$

where ζ_m is the horizontal wavenumber of the m th vertical mode. Deriving analytic expressions for such vertical modes in the simplified, three-layer model considered here can be done by matching the interface conditions, and the details are omitted here. As shown in Fig. 1(b), the vertical mode functions are perturbed by the internal waves that comprise the duct. Also, the horizontal wavenumbers of vertical modes may be affected by the internal waves.

After replacing the sound pressure function in the 3D Helmholtz wave equation with the vertical mode decomposition and employing the assumption of adiabatic mode propagation, one can see that the vertical modal amplitude is governed by a two-dimensional (2D) Helmholtz equation, which is often called the horizontal refraction equation,¹⁵ given by

$$\left(\frac{\partial^2}{\partial x^2} + \frac{\partial^2}{\partial y^2} \right) \Gamma_m + \zeta_m^2(x, y) \Gamma_m = -4\pi \frac{\Psi_m(x_s, y_s, z_s)}{\rho(z_s)} \delta(x - x_s) \delta(y - y_s). \quad (4)$$

This equation was employed in Ref. 5 for studying the focusing/defocusing structure in a straight and endless internal wave duct. Note how the horizontal wavenumber of the m th vertical mode, ζ_m , mimics the wavenumber $k = \omega/c$ in Eq. (1). In addition, the internal waves may alter the values ζ_m , yielding interface/boundary conditions across the waves in the y direction. In the model considered here the internal waves of depression have perturbed wavenumbers that are lower than the unperturbed values so that an incident vertical mode from the inside of the duct impinging horizontally onto the internal waves may encounter a situation where total reflection occurs and vertical modes are ducted in the horizontal plane, as shown in Fig. 1(c).

Solving the horizontal refraction equations for the vertical modal amplitudes allows the sound pressure field to be computed via mode summation. A two-step procedure is implemented. The first step is to obtain the ducted sound field between the simplified internal waves, and the second step is to apply Huygens' principle to obtain the radiation field due to the sound pressure distributed at the open-ended termination.

1. Ducted sound field

We begin by solving for the field at $x \leq L$, where ducted horizontal modes will exist. To solve Eq. (4) in this region, we can utilize many of the methods used in solving boundary value problems in shallow water acoustics, such as the well-known Pekeris waveguide mode problem. But, instead of looking at the constructive interferences of up- and down-going plane waves to get vertical modes, we are now seeking

horizontal modes associated with each vertical mode Ψ_m . Due to barrier penetration and tunneling effects, which cause sound transmission through the internal wave "walls" and radiation outward in the y direction, Eq. (4) is not a proper Sturm-Liouville problem, so we cannot use an exact eigenfunction expansion to generate a solution. Instead, a wave-number integration technique is employed, and a generalized eigenfunction expansion can be achieved for the vertical modal amplitude Γ_m if the branch-line integral is neglected. The detailed derivation is described below. Beforehand, note that the generalized expansion is of the form

$$\Gamma_m(x, y) = \sum_n A_{nm}(x) \Phi_{nm}(y), \quad (5)$$

where Φ_{nm} are the horizontal modes associated with each vertical mode Ψ_m , and A_{nm} are their (complex) amplitudes. A combination of indices (n, m) is required for the horizontal ducted modes. The complete solution for the ducted sound field will be of the form $P(x, y, z) = \sum_m \sum_n A_{nm}(x) \Phi_{nm}(y) \times \Psi_m(x, y, z)$. The horizontal mode functions only depend on y since the environment in the duct area does not have x -dependency. The amplitude A_{nm} depends on x only and will mainly vary due to modal phase delays and modal attenuation, with no geometric spreading loss for the trapped modes.

The wavenumber integration technique of solving Eq. (4) for the vertical modal amplitude Γ_m at $x \leq L$ is now described in detail. First, the assumption of total transmission at the open-ended termination allows us to reformat the problem to be an infinitely long duct problem, and the solution of the reformatted problem at the positions where $x \leq L$ (the internal waves terminate at $x = L$) is valid for representing the ducted sound field. Note that after we get the radiation field solution in Sec. II B 2, we will justify the assumption of total transmission. Since the horizontal wavenumber of the m th vertical mode, ζ_m , does not have x -dependency in the reformatted problem, we can apply the following plane-wave spectral integral or spatial Fourier transform to decompose the vertical modal amplitude in terms of a set of infinite plane waves:

$$\Gamma_m(x, y) = \frac{1}{\sqrt{2\pi}} \int_{-\infty}^{\infty} G_m(k_x, y) e^{ik_x x} dk_x, \quad (6a)$$

$$G_m(k_x, y) = \frac{1}{\sqrt{2\pi}} \int_{-\infty}^{\infty} \Gamma_m(x, y) e^{-ik_x x} dx, \quad (6b)$$

where $G_m(k_x, y)$ is the plane-wave component of the m th vertical modal amplitude with wavenumber k_x . Applying the inverse transform operator to both sides of Eq. (4) yields a one-dimensional, y -dependent Helmholtz equation that is comparable to the depth-dependent Green's function equation in the wavenumber integration technique,¹⁵

$$\begin{aligned} \frac{d^2}{dy^2} G_m(k_x, y) + (\zeta_m^2 - k_x^2) G_m(k_x, y) \\ = -2\sqrt{2\pi} \frac{\Psi_m(x_s, y_s, z_s)}{\rho(z_s)} e^{-ik_x x_s} \delta(y - y_s), \end{aligned} \quad (7)$$

which is subject to interface conditions on the internal-wave

“walls” that can be expressed as plane-wave reflection coefficients.

To determine $G_m(k_x, y)$ (and thence Γ_m) for $x \leq L$, we first obtain a solution for the domain bounded by the internal waves $-D/2 \leq y \leq D/2$, where $y = \pm D/2$ are the inner

boundaries of the internal waves, and then extend the bounded domain solution to the external domain by matching the interface condition at $y = \pm D/2$. Utilizing the endpoint method,¹⁶ the plane-wave component $G_m(k_x, y)$ in the bounded domain ($|y| \leq D/2$) can be found as

$$G_m(k_x, y) = \begin{cases} i\sqrt{2\pi} \frac{\Psi_m(x_s, y_s, z_s)}{\rho(z_s)} e^{-ik_x x_s} \frac{[e^{-ik_y y} + R_{Lm} e^{ik_y D} e^{ik_y y}][R_{Rm} e^{ik_y D} e^{-ik_y y_s} + e^{ik_y y_s}]}{k_y [1 - R_{Lm} R_{Rm} e^{2ik_y D}]} & \text{for } -D/2 \leq y \leq y_s, \\ i\sqrt{2\pi} \frac{\Psi_m(x_s, y_s, z_s)}{\rho(z_s)} e^{-ik_x x_s} \frac{[e^{-ik_y y_s} + R_{Lm} e^{ik_y D} e^{ik_y y_s}][R_{Rm} e^{ik_y D} e^{-ik_y y} + e^{ik_y y}]}{k_y [1 - R_{Lm} R_{Rm} e^{2ik_y D}]} & \text{for } y_s \leq y \leq D/2, \end{cases} \quad (8)$$

where $k_y^2 = \zeta_m^2 - k_x^2$, and R_{Lm} and R_{Rm} are the plane-wave reflection coefficients at $y = -D/2$ and $D/2$, respectively, as a function of k_x and the m th vertical modal phase speeds inside and outside the internal waves. The plane-wave reflection coefficients can be obtained using the usual formulas for plane-wave reflections from horizontally stratified multilayered media. Note that there is no horizontal density contrast in the system we are considering. To complete the solution for the vertical modal amplitude Γ_m , we insert Eq. (8) into Eq. (6a) and employ a complex contour integration technique. This immediately gives us the equation for the eigenvalues:

$$1 - R_{Lm} R_{Rm} \exp(2i\sqrt{\zeta_m^2 - k_x^2} D) = 0. \quad (9)$$

Since the plane-wave reflection coefficients R_{Lm} and R_{Rm} depend on which vertical mode is being considered, solving this eigenvalue equation leads to a set of horizontal mode wavenumbers for each vertical mode considered. There are two kinds of horizontal modes: trapped modes forming the ducted sound field and leaky modes forming the sound penetrating the internal waves and radiating laterally outward in the y direction. By selecting the Pekeris branch cut and neglecting the branch-line integral, the vertical modal amplitude Γ_m in the domain bounded by the internal waves ($-D/2 \leq y \leq D/2$) is found to be

$$\Gamma_m(x, y) = 2\pi i \frac{\Psi_m(x_s, y_s, z_s)}{\rho(z_s)} \sum_n \frac{\Phi_{nm}(y_s)}{\kappa_{nm} w_{nm}} e^{i\kappa_{nm}(x-x_s)} \Phi_{nm}(y), \quad (10a)$$

where w_{nm} is the normalization factor for the unnormalized horizontal mode function Φ_{nm} ,

$$w_{nm} = i[d(1 - R_{Lm} R_{Rm} e^{2ik_y D}) / dk_y]_{k_x = \kappa_{nm}}^{k_y^2 = \zeta_m^2 - k_x^2} \times [R_{Lm} e^{i\sqrt{\zeta_m^2 - \kappa_{nm}^2} D}], \quad (10b)$$

$$\Phi_{nm}(y) [e^{-i\sqrt{\zeta_m^2 - \kappa_{nm}^2} y} + R_{Lm} e^{i\sqrt{\zeta_m^2 - \kappa_{nm}^2} (y+D)}] \quad \text{for } -D/2 \leq y \leq D/2, \quad (10c)$$

and κ_{nm} is the x -component wavenumber of the n th horizontal mode resulting from the eigenvalue equation, Eq. (9),

given that we have m th vertical mode excited. The normalization factor w_{nm} can be found numerically by employing a series of chain rules. This involves finding the first derivatives of the reflection coefficients with respect to k_y . In addition, taking a total derivative of the eigenvalue equation, Eq. (9), with respect to the frequency ω at $k_x = \kappa_{nm}$ yields the group slowness of the horizontal modes ($dk_x/d\omega$) and hence the group velocities. To extend the solution shown in Eq. (10a)–(10c) to $|y| > D/2$ with the assumption of adiabatic mode propagation, one can determine the unnormalized horizontal mode function outside the bounded domain by satisfying the continuity and smoothness conditions across all of the horizontal interfaces. For the horizontal ducted modes of interest, the horizontal trapped mode functions are sinusoids within the bounded domain and decay exponentially to vanish outward in the y direction. Note that, in the complex contour integration, without compensation of the branch-line integral for the exponential growth of the horizontal leaky modes in the y direction, the solution does not converge along the y -axis when the x -coordinate of a calculation point is close to the source. However, the boundary of this diverging area gets further and further out in the y direction as the x -coordinate of the calculation point moves away from the source, and so the branch-line integral can generally be neglected when the computation domain of interest expands reasonably in the x direction. After all, in the domain of small x and large y the sound field is dominated by the mode coupling effect occurring as the sound penetrates the internal waves at high grazing angles. This coupling is beyond the limitation of our 3D normal mode theory, so the branch-line integral failure is inconsequential.

2. Radiation field

The contribution of each vertical mode to the sound field at the termination of the duct ($x=L$) can now be computed from Eq. (10a)–(10c), and then used to obtain the radiation field from the termination by adopting Huygens' principle. Under the prior assumptions, the ducted sound will pass through the termination and radiate outward, with vertical modal energy staying in the same mode (adiabatic mode propagation). Hence, the total radiation field can be obtained by summing up all the vertical mode radiations.

The amplitude of the m th vertical mode at every termination position ($x=L$) is given by Eq. (10a)–(10c). According to Huygens' principle, solutions at ($x>L$) must be consistent with an infinite number of "modal" point sources adjoining each other across the termination, radiating the modal energy outward. Mathematically, the solution is found using the Green's function method. The required Green's function $\mathcal{G}_m(x,y;\xi,\eta)$, where (ξ,η) indicates the termination position, i.e., $\xi=L$, is symmetric and equals $\mathcal{G}_m(\xi,\eta;x,y)$ by the principle of reciprocity. This is governed by

$$\left(\frac{\partial^2}{\partial \xi^2} + \frac{\partial^2}{\partial \eta^2}\right) \mathcal{G}_m(\xi,\eta;x,y) + \zeta_m^2 \mathcal{G}_m(\xi,\eta;x,y) = -\delta(\xi-x, \eta-y). \quad (11)$$

Note that since the m th vertical modal amplitude at the termination provides a Dirichlet boundary condition for the radiation field, a homogeneous Dirichlet boundary condition for the Green's function ($\mathcal{G}_m(\xi,\eta;x,y)=0$) is required at $\xi=L$. The method of images yields

$$\mathcal{G}_m(x,y;\xi,\eta) = \frac{i}{4} H_0^{(1)}(\zeta_m \sqrt{(\xi-x)^2 + (\eta-y)^2}) - \frac{i}{4} H_0^{(1)}(\zeta_m \sqrt{(\xi+x-2L)^2 + (\eta-y)^2}), \quad (12)$$

where $H_0^{(1)}$ is the zeroth order Hankel function of the first kind. With this Green's function, it is straightforward to obtain the radiated mode amplitude at $x>L$, i.e., $\Gamma_m(x,y) = \int \Gamma_m(L,\eta) \partial \mathcal{G}_m(x,y;\xi,\eta) / \partial \xi|_{\xi=L} d\eta$, and $\Gamma_m(L,\eta)$ is the m th vertical modal amplitude across the termination. Substituting the necessary terms yields

where $H_1^{(1)}$ is the first order Hankel function of the first kind, resulting from differentiation of $H_0^{(1)}$. It is numerically straightforward to implement this Hankel integral, which is done in Sec. II C. Alternatively, with the assistance of the principal asymptotic form of the Hankel function for large arguments, the far-field approximation is given by

$$\Gamma_m(x,y) = 2\pi e^{i(\pi/4)} \sqrt{\zeta_m} \frac{\Psi_m(x,y,z_s)}{\rho(z_s)} \times \sum_n \frac{\Phi_{nm}(y_s)}{\kappa_{nm} w_{nm}} e^{i\kappa_{nm}(L-x_s)} \Omega_{nm}(r,\theta), \quad (14)$$

where $r = \sqrt{(x-L)^2 + y^2}$, $\theta = \tan^{-1}[y/(x-L)]$, $\Omega_{nm}(r,\theta) = r^{-1/2} e^{i\zeta_m r} \sin \theta \hat{\Phi}_{nm}(\theta)$, and $\hat{\Phi}_{nm}(\theta) = (2\pi)^{-1/2} \int_{-\infty}^{\infty} \Phi_{nm}(\eta) \times e^{-i2\pi u \eta} d\eta$, where the u in the exponent equals $\zeta_m \sin \theta / (2\pi)$.

The normal mode solutions for the ducted field and the radiation field have been obtained, and now we shall re-visit the prior assumption of total transmission at the open-ended termination. Remember that since the termination gap is very large compared to the underwater acoustic wavelength of interest in a common case, the ka value (acoustic wavenumber multiplying the gap aperture) is large and thus only tiny amount of reflection energy is yielded, which means that the

assumption of total transmission should be valid. In addition, we can examine the continuity of the normal derivative of the pressure field solution (the smoothness) across the termination, as we notice there is only pressure continuity condition being used in deriving the radiation field solution. If the assumption of total transmission is sustained, the pressure field solution should be smooth across the termination, as shown in the next computational example.

C. Computational example

A numerical integration scheme is utilized to compute the analytic solution shown in Eq. (13), and the environmental model considered here is illustrated in Fig. 1(a). To remind the reader, a 3D Cartesian coordinate system (x - y - z) is chosen for positioning (see the figure for the orientation). The water column has two homogeneous layers; the sound speed in the upper layer is 1520 m/s, faster than the lower layer, where the sound speed is 1480 m/s. The density in the water column (in both layers) is 1.0 g/cm³. The water depth is 80 m, and the thickness of the upper water layer is 20 m. Two nonlinear internal waves with square waveform disturb the water column, and their wavefronts are both parallel to the x -axis. These internal square waves have the same amplitude, 20 m, and wavelength, 200 m, and they both abruptly terminate at $x=20$ km. The gap between the internal waves is 300 m wide. The bottom is considered to be homogeneous, with sound speed of 1700 m/s, sound attenuation coefficient of 0.5 dB/ λ , and density of 1.5 g/cm³.

The first result shown here is the dependence of the radiation patterns of the vertical modes on the acoustic source position. A sinusoidal 100-Hz source is considered, and Fig. 2 shows the intensity contours of the first and second vertical modes excited by the source located at four different x - y positions in the gap between nonlinear internal waves. The internal waves form a horizontal duct at positions $0 \leq x \leq 20$ km where the sound transmitted from the source is trapped. The waves terminate at $x=20$ km, and the trapped sound radiates away at this position. Note that the source depth is fixed ($z_s=-70$ m), and the internal waves have a square shape so that excitation of vertical modes is the same for each of the four source positions. There are more than two vertical modes excited by the source, but only the first two of them are shown in the plot. As shown in the figure, each vertical mode has its unique radiation pattern. That is because the across-duct energy distribution of each vertical mode at the termination is unique [see Eq. (13)]. Note also that the radiation pattern of each vertical mode differs dramatically for different source positions in the duct between the waves. The reason is that for a given vertical mode the excitation of the horizontal modes in the duct strongly depends on the source position in the y -axis [see Eq. (10a)–(10c)], so the across-duct energy distribution of the given vertical mode at the termination is a function of source position, and thus the radiation pattern is a function of source position.

The next computational result shows broadband sound radiation from the termination of an identical truncated internal square-wave duct. The previous harmonic source is re-

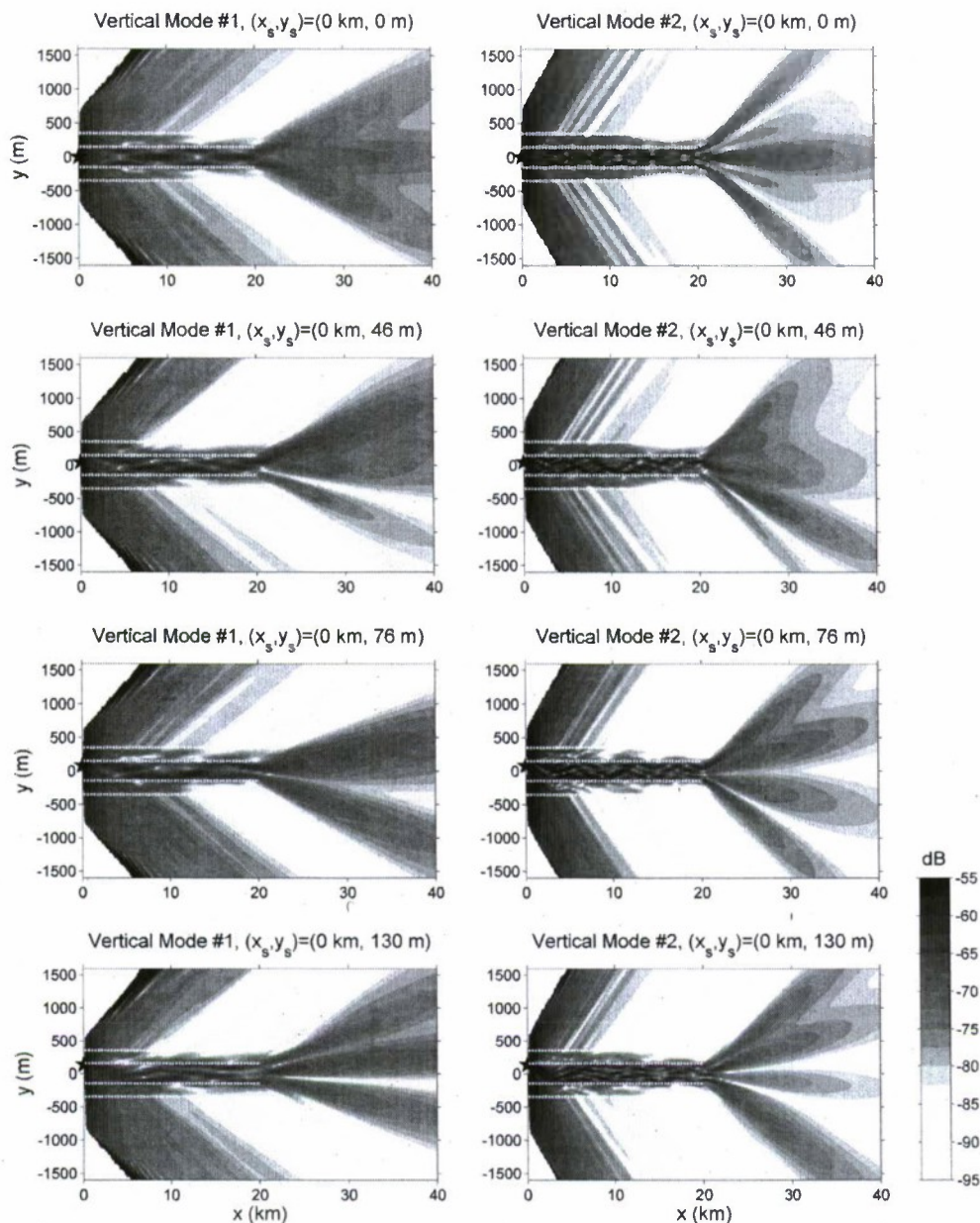


FIG. 2. (Color online) Intensity is shown for the first two vertical modes excited by a sinusoidal 100-Hz source located at four different y positions (shown from top to bottom). The source is always in the gap between the nonlinear internal waves, and the simplified model of Fig. 1 is used. Mode 1 intensity is shown on the left, mode 2 on the right. The source depth is fixed. The edges of internal waves are indicated by dashed lines. See the main text for the detailed environmental and acoustic source parameters.

placed by a source emitting a broadband signal which contains 16 periods of a 100-Hz sine wave and is tapered by the Hann window. Note that 99.95% of the source energy is contained in the 25-Hz bandwidth centered at 100 Hz. This broadband source is fixed at a position of $(x_s, y_s, z_s) = (0 \text{ km}, 0 \text{ m}, -70 \text{ m})$, and a hydrophone array is placed at $x=30 \text{ km}$ (10 km distant from the termination of the internal-wave duct). The array has a vertical component [vertical line array (VLA)] covering the whole water column and located at $y=0 \text{ m}$ and a horizontal component [horizontal line array (HLA)] placed on the bottom and extending along the negative y -axis for 1000 m.

The internal waves form a horizontal acoustic duct at positions $0 \leq x \leq 20 \text{ km}$. Horizontal modal dispersion in the duct is examined here because this phenomenon affects the

broadband result. The dispersion of horizontal modes can be quantified by modal group velocities. Figure 3 shows how, for this duct configuration, the group velocities of the horizontal modes associated with the second vertical mode vary with the horizontal mode number and the frequency. The group velocities of horizontal modes have upper limits given by the group velocity computed using profiles in the wave crests (i.e., away from the wave duct region, which happens to be the profile in the duct itself for this idealized configuration). However, when the horizontal mode angle with respect to the internal-wave crests, determined from $\cos^{-1}(\kappa_{nm}/\zeta_m)$, nears the critical grazing angle for total internal reflection, the horizontal modal energy tunnels through the internal-wave trough, where the vertical modal phase and

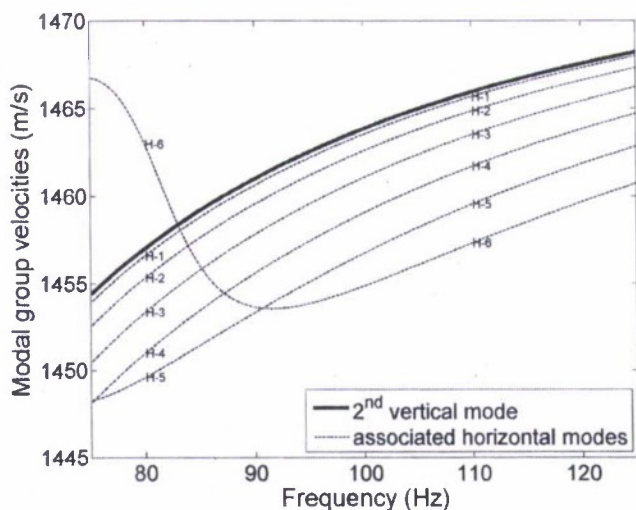


FIG. 3. Group velocities of the unperturbed second vertical mode (solid line) and six of its associated horizontal ducting modes (dashed lines) are shown for the simplified model of Fig. 1. The six horizontal modes are labeled by numbers.

group velocities are higher, and thus the horizontal modal group velocity increases and exceeds that limit (see the sixth horizontal mode in Fig. 3).

The four panels in Fig. 4 illustrate the magnitude of the broadband acoustic time series received on the hydrophone

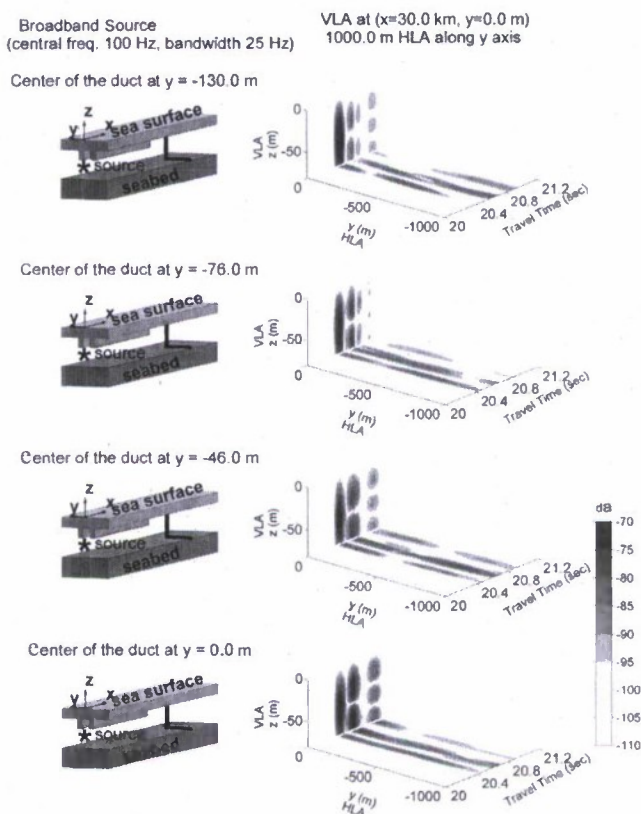


FIG. 4. (Color online) Broadband sound radiation from the termination of the internal-wave duct in the simplified model. From top to bottom, the y position of the source with respect to the waves differs. The right panels illustrate the pulse intensity received at the horizontal and vertical arrays, denoting by thick lines in the left panels. See the main text for the detailed information about the model parameters.

arrays (both on the VLA and the HLA) when the truncated internal-wave duct is located at four different positions along the y -axis. As shown in the plot, each vertical mode arrival is well separated in time at the array; the arrivals on the VLA nicely represent the vertical mode shapes, and the arrivals on the HLA provide a means for us to observe the energy distribution of each vertical mode along the y -axis. Due to the change in source position in the internal-wave duct, modal radiation patterns at these four cases are different, and we do see the intensity of modal arrivals changing. This broadband source calculation does show the effect of horizontal modal dispersion (see the multiple arrivals of the second vertical mode in the top two panels of the plot). This is indeed a nice illustration in the time domain that the modal field now has vertical and horizontal mode numbers.

III. 3D PARABOLIC EQUATION MODELING

In the ocean, background sound speed profiles and nonlinear internal waves are not as simple as in the previous simplified model, and it would be challenging if not impossible to obtain an analytical solution for the 3D sound field. In order to handle a more realistic case, an acoustical propagation program¹⁰ using the 3D parabolic approximation is employed here. The modeling technique utilized in this program is discussed briefly below, and the reader is referred to the technical report¹⁰ for further details. Note that the parabolic approximation is more complete than the approach of Sec. II because it allows mode coupling, which has been observed to occur in the field, but is not expected to occur near the termination which we are modeling.

A. Split-step Fourier algorithm

The acoustical propagation program we use employs the split-step Fourier (SSF) technique¹⁷ to solve the 3D parabolic acoustic wave equation (PE) for one-way propagating waves from a harmonic source in a Cartesian coordinate system. The SSF technique divides propagation over each distance increment through a heterogeneous sound speed environment into step-by-step "free space" propagation through a medium having a fixed reference wavenumber and periodically introduced (at each step) phase fluctuations consistent with departures from that fixed speed. The free space propagation is handled in the wavenumber domain, and the phase anomalies are introduced in the spatial domain. Amplitude effects such as absorption are introduced with the phase anomalies. Thus, each step (defined to be in the x direction) requires a 2D Fourier transform and an inverse 2D Fourier transform. Note that the wide-angle variant of the propagation operator¹⁸ is used.

B. Numerical simulation example

The environmental conditions for the numerical simulation using the Cartesian 3D PE program are illustrated in the upper-left panel of Fig. 5 and are described here. The water depth is 80 m, and a typical downward refracting sound speed profile observed in the ocean is considered. The bottom geoaoustic properties are listed in the figure. Note that the bottom density is set to be 1 g/cm^3 because the current

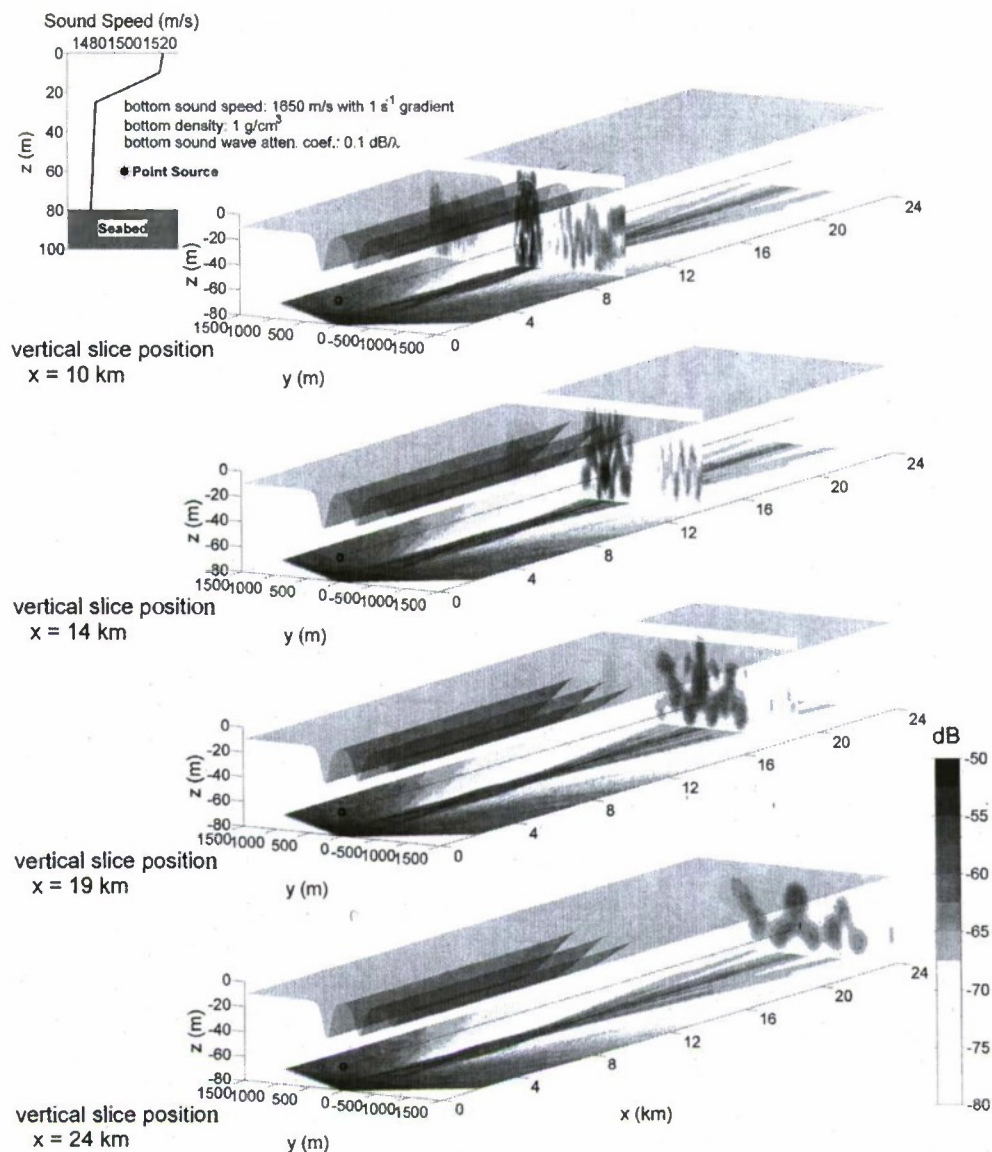


FIG. 5. (Color online) Numerical simulation of 3D sound propagation in an internal-wave duct model. (a) Upper left panel: environmental conditions in the numerical calculation. The sound speed profile represents a downward refracting situation in shallow water ocean. A sinusoidal 200-Hz source is located at 60-m depth. (b) Lower right panel: illustrations of 3D sound pressure fields. On the bottom of the visualization volume a 2D distribution of depth-averaged sound intensity is shown. The vertical slices show intensity on the slice. The transparent surface illustrates the displacement of the top of thermocline layer, i.e., internal waves.

version of this Cartesian 3D PE program does not allow medium density to vary; however, the conclusion drawn from the simulation result should still be valid. The nonlinear internal-wave chain moving in the y direction consists of three solitons, which depress the thermocline into the deeper water column. Although the solitons have different amplitudes, they all satisfy the Korteweg-de Vries (KdV) nonlinear internal-wave equation. Along the soliton wavefront (see the transparent surface shown in the lower-right panels of Fig. 5), the internal-wave waveform extends to $x=10$ km distant from the acoustic source with a permanent shape and then gradually diminishes to zero within a 4 km distance (14 km total).

The first numerical calculation is for narrowband sound propagation. The acoustic source, emitting 200-Hz sound, is placed between the biggest two solitons and at 60-m depth in

the water, close to a node of the third acoustic mode. The calculation domain of the 3D PE program is configured in such a way that we can simulate sound propagating in the nonlinear internal-wave duct and radiating outward from the termination of the duct. A mode filtering is employed to obtain acoustic mode amplitudes at each (x,y) position from the full-field solution. The 3D visualization volume in Fig. 5 shows the simulation results. On the bottom of the visualization volume a 2D distribution of depth-averaged sound intensity is presented, and a vertical slice slides through the field to show detailed 3D structure. The mode amplitudes resulting from mode filtering are shown in Fig. 6 as horizontal contours, from which the following is observed.

Within the first 10-km propagation distance, despite some of the sound energy escaping at high angles with respect to the duct direction, the modal interference process

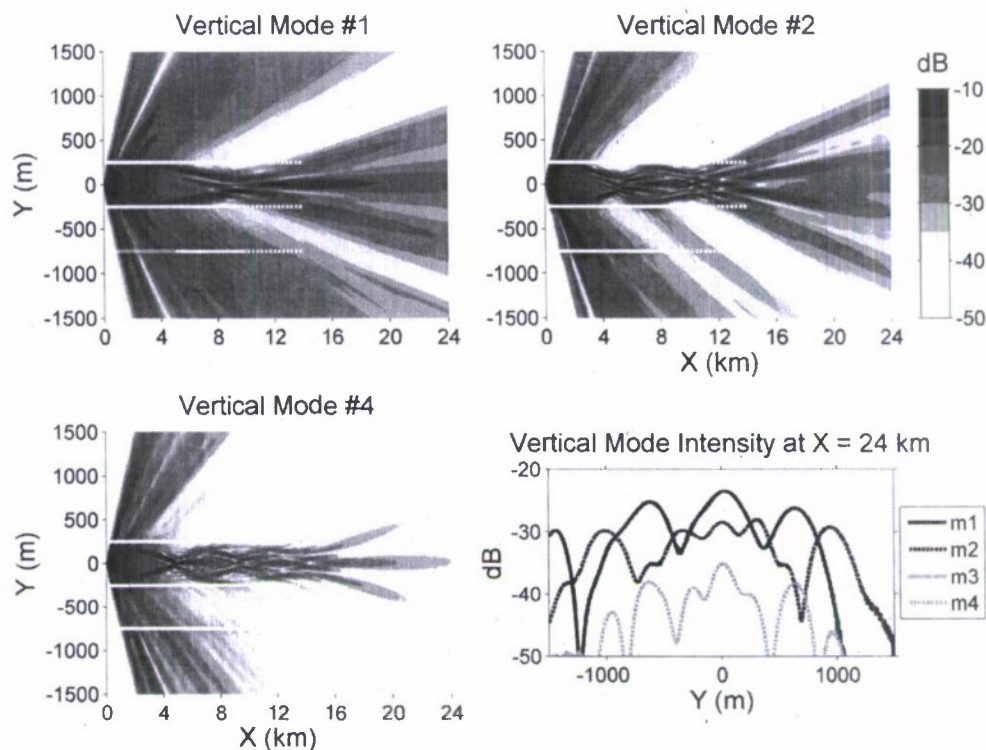


FIG. 6. (Color online) Vertical mode intensity is shown for propagation in the environmental model of Fig. 5. The solid lines are along internal-wave troughs, and the dashed lines indicate the “diminishing region” of the internal waves. See the main text for detailed discussions. At the lower right, the modal intensity at the right hand edge of other panels is plotted.

yields a strong focusing effect in the internal-wave duct, which is consistent with what has been reported in the literature.^{1,3,5-7} The radiation beam pattern, unique to each mode, starts to develop in the diminishing region of internal waves and becomes fully developed after the sound exits the duct with the features suggested by the simplified analytic model in Sec. II. Note that from the plot of mode amplitudes (Fig. 6) no mode-coupling effect is observed in both the ducted sound area and the radiation field, which confirms the assumption of adiabatic mode propagation used in deriving the normal mode solution.

The next case is broadband sound propagation, and the previous narrowband source is replaced by a source emitting a broadband signal which contains 16 periods of a 200-Hz sine wave and is tapered by a Hann window. Since 99.95% of the source energy is contained in the 50-Hz band centered at 200 Hz, one can calculate the fields for frequencies from 175 to 225 Hz (at N -Hz spacing) and sum them to produce a N^{-1} -second-long broadband reception at any receiving point. The four panels in Fig. 7 illustrate the magnitude of the broadband signals received at four VLAs distributed across the wavefront at the end of the propagation distance ($X = 24$ km). The VLA locations are chosen to reveal the spatial variability of broadband sound radiation from the open end of the nonlinear internal-wave duct. A good reference VLA is the one located at the source axis (labeled as $Y = 0$ m), where all vertical modes except for the third mode are distinct. Note that since the source is placed close to a depth null of the third mode, insignificant modal energy is excited. First we see that at $Y = 300$ m the fifth mode fades out, and (more dramatically) at $Y = 1101$ m only the second mode is observ-

able. In addition, as seen in the previous analytical computation, multiple arrival of the same mode is also observed in this numerical calculation (mode 1 at $Y = -1251$ m). All of these plots truly convey the complexity of the sound field due to the modal radiation effect.

IV. EXPERIMENTAL DATA

In Secs. II and III theoretical and numerical analyses have been implemented to study acoustic mode radiation

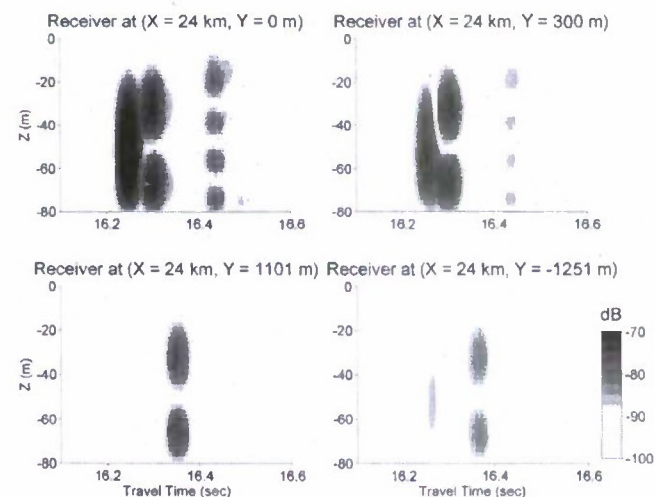


FIG. 7. (Color online) Simulation results for broadband sound (50-Hz bandwidth centered at 200-Hz) propagation in the environmental model of Fig. 5. These four panels show the intensity of the broadband signals received at four vertical hydrophone line arrays distributed across the wavefront at $X = 24$ km.

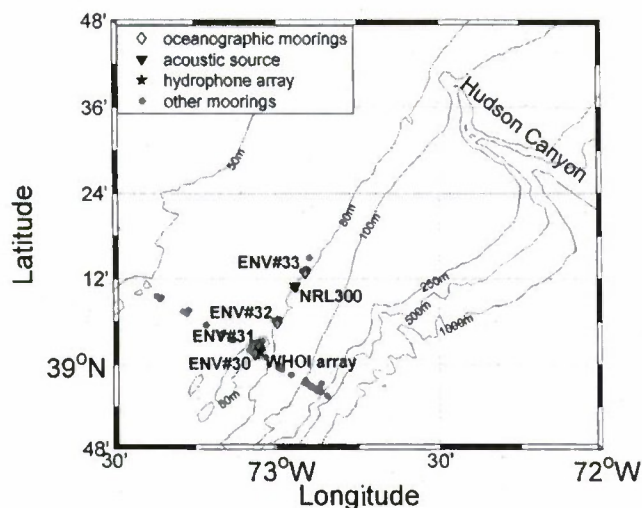


FIG. 8. Study area of the SW06 experiment. The depth of each isobath line is labeled. A total of 62 moorings was deployed in a "T" geometry to create an along-shelf path and an across-shelf path. The data collected from the six labeled moorings on the along-shelf path are used in this paper.

from the terminations of idealized square-wave and KdV-model internal-wave ducts. Here we shall examine acoustic signals measured in the coastal ocean for evidence of features similar to those seen in the computational examples. In the summer of 2006 a large multi-disciplinary experiment, SW06,¹¹ was conducted on the Mid-Atlantic Bight continental shelf at a location about 160 km east of the New Jersey coast and about 80 km southwest of the Hudson Canyon (Fig. 8). A total of 62 acoustic and oceanographic moorings

was deployed in a "T" geometry to create an along-shelf track (following the 80-m isobath line) and an across-shelf track (depths changing from 50 to 500 m). In this paper, we will focus on the data collected from some of the moorings deployed on the along-shelf track. At the southern end of the along-shelf track, an underwater hydrophone-array system (labeled by "WHOI array" as it was deployed by the acoustics group from the Woods Hole Oceanographic Institution) was positioned. This system has two arrays: one is a 16-channel VLA covering the water column from depth 13.5 m to the bottom, and the other is a 465-m-long HLA with 32 uniformly-spaced hydrophones deployed on the bottom in a strict N-S orientation. There were many acoustic sources deployed in the water during the SW06 experiment, and the specific source of interest on the along-shelf track is a source transmitting a frequency modulated (FM) sweep sound centered at frequency of 300 Hz with 60-Hz bandwidth (labeled by "NRL300" as this source is owned by the U.S. Naval Research Laboratory). Water temperature data collected at the NRL300 source mooring and the WHOI array will be used to identify internal waves. Four oceanographic moorings deployed on the along-shelf track (labeled by ENV#30-33) also provide other useful environmental measurements, including water temperature and current speeds.

The environmental data indicate that a strong nonlinear internal-wave packet with a somewhat straight wavefront started passing through the along-shelf mooring track at about 10:00 Greenwich mean time (GMT) on August 20 (see Fig. 9). The angle between the wavefront and the along-shelf track was about 6 deg. The environmental data also indicate

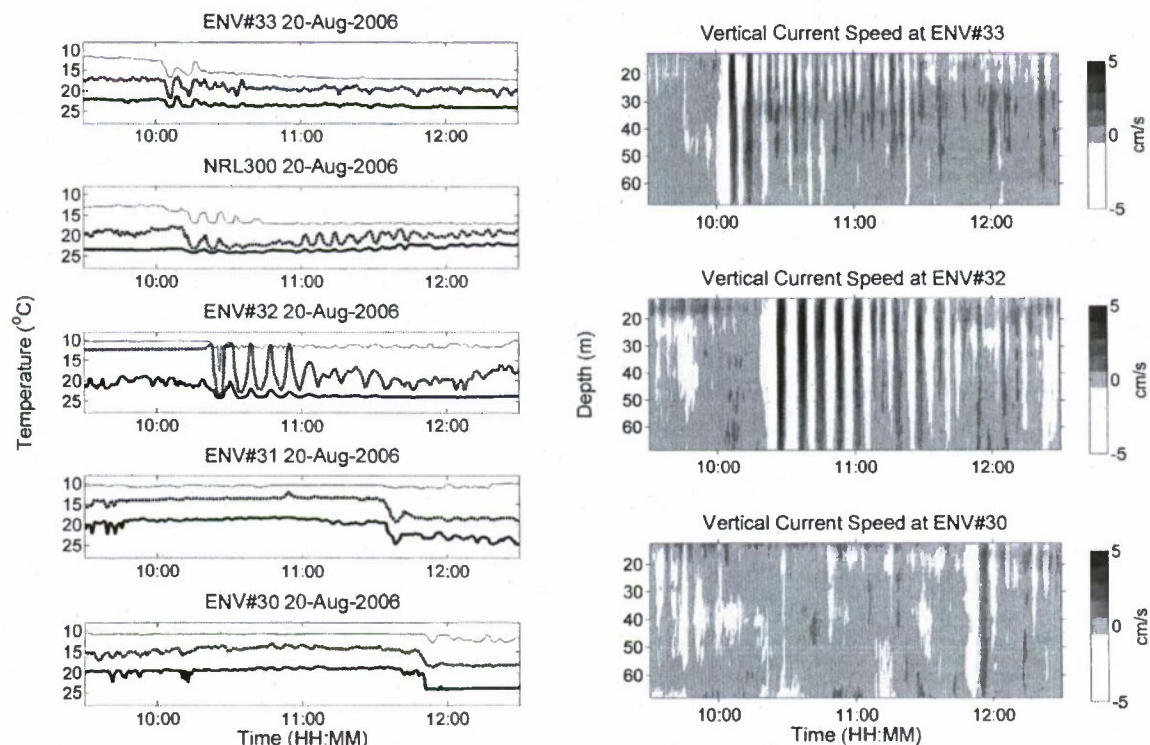


FIG. 9. (Color online) Environmental data collected from the moorings distributed along the 80-m-isobath track (total 30 km long) in the SW06 experiment on August 20 from 8:00 to 14:00 (GMT). Left panels: temperature data at three different depths about 10 m (thick line), 20 m (dashed line), and 30 m (thin line). Right panels: vertical current speeds measured by the acoustic Doppler current profilers. Both temperature and current speed data show that a truncated nonlinear internal-wave packet, terminating between moorings ENV#32 and ENV#31, passed through the mooring track.

that this internal-wave packet terminated between moorings ENV#32 and ENV#31, and that the exact terminating point should be around 13 km distant from the NRL300 source and 5 km distant from the WHOI array. The NRL300 source was designed to transmit sound for 7.5 min at every hour and half-hour. At the next transmission (10:30 GMT) after the internal-wave packet reached the NRL300 source, the source was still in the packet. Hence it can be expected that the sound transmitted from the source would be trapped in the duct formed by the internal waves and propagate toward the termination of the internal-wave packet between moorings ENV#32 and ENV#31. The trapped sound would then radiate out from the termination and finally reach the WHOI array. In the following, we will see that the sound field received at the array was structured in a way that suggests that ducting and radiation from the duct had strong influences.

The NRL300 source linearly swept over 270–330 Hz in exactly 2.048 s every 4.096 s for 110 times, which yielded a 7.5-min-long transmission, at every hour and half-hour. Each sweep was tapered with a 0.2048-s amplitude taper (10% cosine taper) at the beginning and the end to allow gradually ramping on and off. A standard matched filter can compress the sweep to 33 ms, but with significant side-lobe ripples that could mask the multi-modal arrivals in this case. To reduce the side lobes, one can apply a taper window on the replica waveform of the matched filter¹⁹ at the cost of increasing the (compressed) pulse length. In this data analysis the Hamming window function is applied, and the matched filter with such a tapered replica waveform produces 66-ms-long compressed pulses with side lobes less than –30 dB. Three of the 110 pulses are shown in Fig. 10, where one can clearly see complicated temporal and spatial variability. To further analyze the data and quantify the variability, the following modal analyses are performed.

Modal excitation by the NRL300 source during the transmission period encountering the truncated internal-wave packet is calculated by the acoustic normal mode program KRAKEN.²⁰ The *in situ* water sound speed measurements on the NRL300 source mooring and a bottom model provided by a previous study²¹ are used in the program. The calculation results, shown in Fig. 11, indicate that the variation in modal energy excitation caused by the local water-column fluctuations is less than 3 dB, with the maximum variation occurring in the first mode. A series of broadband mode filterings is performed next to examine the vertical modal content of the received pulses on the WHOI VLA. The vertical mode functions used in the filter are calculated by the KRAKEN program, and the *in situ* water sound speed measurements on the WHOI VLA and the same bottom model for modal excitation calculation are used. Figure 12 shows the vertical mode functions of frequency 300 Hz at 10:32:30 GMT. The mode-filter outputs, shown in Fig. 13, reveal a very interesting mode-dependent variation pattern; one can see that modal arrival levels can vary up to 30 dB in 3 min, and also that modal arrivals alternately diminish. This is quite striking. Examining possible causes of this, given the good coverage of the WHOI VLA in the water column (see Fig. 12), there should not be a serious modal cross-talking defect in the mode filtering process, especially for the lowest

three modes. Hence the modal variation seen in the filter outputs is not due to imperfect signal processing. Another possible explanation is variable modal excitation. A modal excitation calculation suggests that less than 3-dB variation should be expected, which cannot explain the 30-dB variations in modal arrival levels, not even if one placed considerable uncertainty on the modal excitation prediction. Invoking known mechanisms for mode coupling is also unreasonable because the fairly straight wavefront of the truncated internal-wave packet is only about 6 deg to the propagation path from the source to the receiver, which is smaller than the typical angles causing coupling (although the very largest waves measured in the SW06 area, 20-m amplitude, may cause coupling at 8 deg²²). Thus, the modal arrivals are most consistent with time-variable of acoustic mode radiation from the internal-wave duct termination. As the internal-wave duct passed over the NRL300 source the relative source position in the duct changed, causing horizontal modal radiation pattern fluctuation in the manner illustrated by the examples.

V. DISCUSSIONS

The theoretical and numerical calculations clearly show that variable acoustic mode radiation from the termination of an internal-wave duct can be a significant source of spatial and temporal fluctuations of sound outside the duct. The spatial fluctuations result from the narrow angular extent of the radiation beams, for each mode, that emerge from the termination. One consequence is that the sound intensity in the areas not covered by radiation beams is reduced. The beams have temporal variability because passage of a truncated internal-wave duct over a fixed source causes the source position in the duct to vary in time, thus giving a time-dependence to the excitation of horizontal mode and thus to the emerging beams.

The real oceanic environment is often more complicated than the modeled environments used in this paper, and there are other acoustic effects that cause acoustic fluctuation patterns that are similar to the modal beam effect and that we shall be aware of. For instance, the effect of mode coupling on changing received modal intensity can be similar to the modal beam effect. To distinguish these two effects, one may need to carefully examine environmental data and determine which effect is more likely to occur in the environmental condition, as done here for the NRL300 signals. The following is another example. The calculations herein show that horizontal modal dispersion within the duct may cause multiple arrival of a mode (see the top two panels of Fig. 4 and the lower right panel of Fig. 7). However, in sound transmission data collected in the 1988 Hudson Canyon Experiment,²³ Cederberg *et al.*²⁴ observed that a deep sub-bottom duct may produce two different modes with almost identical wavenumbers and with shapes that are similar in the water column. Separate arrival of the two modes may be mistaken for multiple arrival of the same mode, particularly when noise is present. This sub-bottom ducting effect presents an alternative explanation of the double (repeat) mode features.

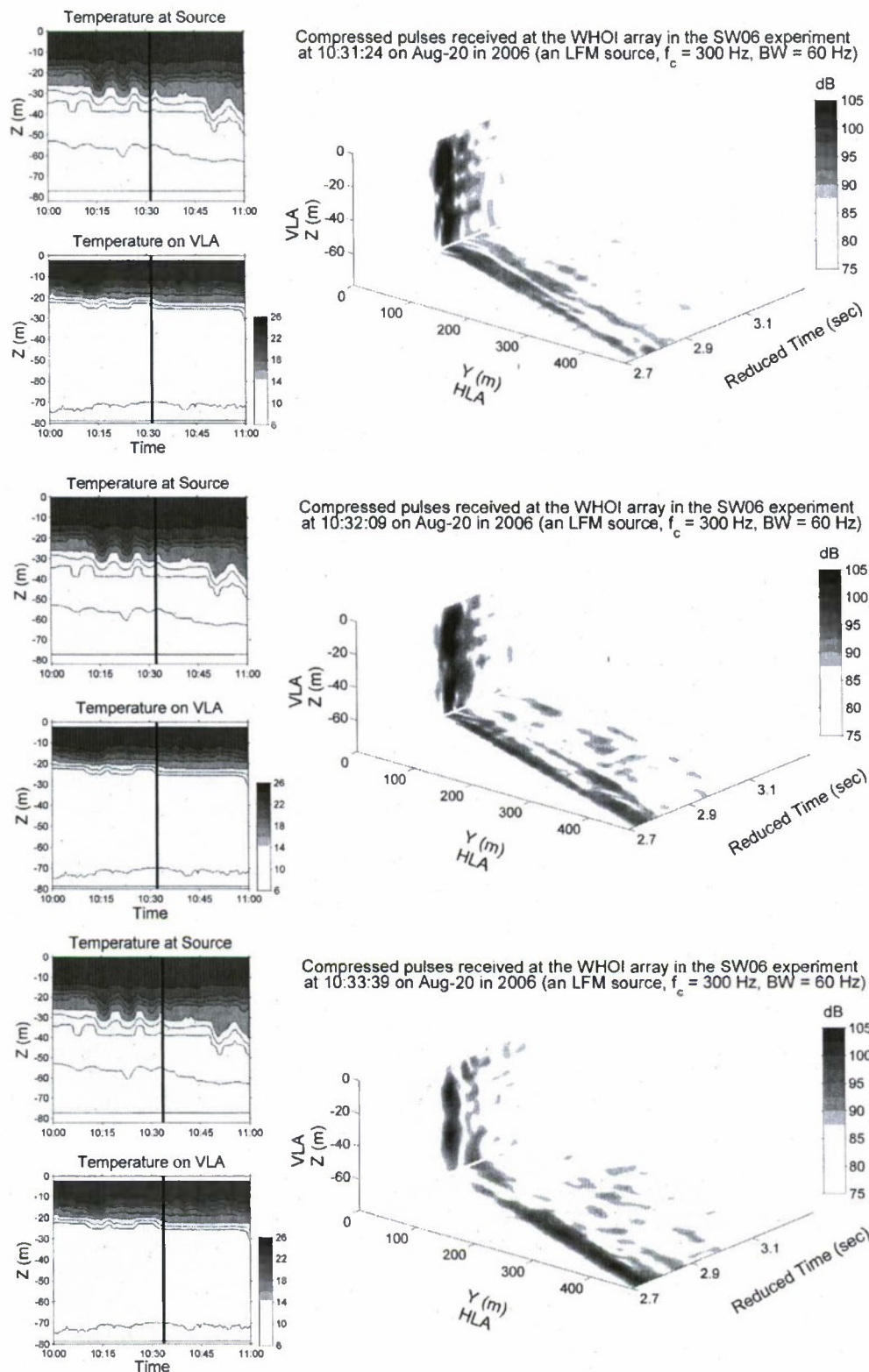


FIG. 10. (Color online) Compressed pulses of the NRL300 sweep signals received on the SW06 WHOI array. (Right) Pulse arrivals at three times are shown, from top to bottom. To the left of each pulse plot, temperature vs depth time series for the source and receiver positions are shown. The line indicates the condition at the time of transmission. At these times, the source was in the truncated internal-wave packet shown in Fig. 9.

During the SW06 experiment, other internal-wave ducting situations were observed, such as curved waves or fragmented waves. In the interesting curved wave situation, sound initially trapped in the duct may escape due to the change in the grazing angles of trapped sound. That is, hori-

zontal modes that are sub-critical may become supercritical and escape. As for a fragmented internal-wave field, sound will encounter multiple processes of trapping and radiating, and the single truncation case reported in this paper may serve as a starting point toward understanding that multiple-

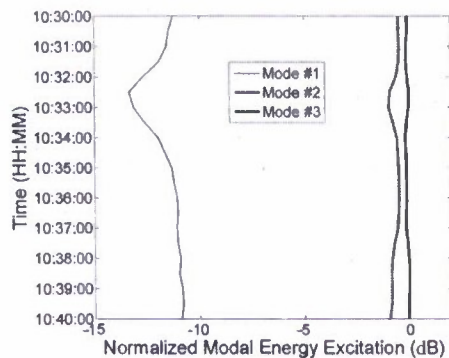


FIG. 11. Time series of theoretical estimates of the energy excitation of first three modes by the NRL300 source during the truncated internal-wave event shown in Fig. 9 on August 20.

scatter case. It is also worth mentioning that when an acoustic source is just outside and close to a truncated internal-wave duct, the significance of the mode radiation effect depends on how far the source is away from the duct. If it is close, a certain amount of energy may still be trapped in the duct after the sound refracts into the duct, and so at the termination one can still observe significant radiation effects.

The modal radiation may affect horizontal array beamforming. The simulations show that the termination acts like a sound projector, and horizontal beamforming may show incorrect sound source bearing directed toward the termination. Note that narrow beams are not plane waves, and standard beamforming with arrays larger than the beam width may be inconclusive. Also, because of the interference of the radiation patterns of different modes, the array coherent length in the radiation field may be much shorter than what would be expected at array locations far from internal waves (a typical value in the SW06 site is 15 wavelengths at 100 Hz, according to the measurement of Collis *et al.*²⁵ during quiescent periods. Further analysis of a larger portion of this data set shows higher values of 25–30 wavelengths during the first week of the experiment).

VI. CONCLUSIONS

The sound radiation from the termination of a truncated internal-wave duct has been studied with both analytical and

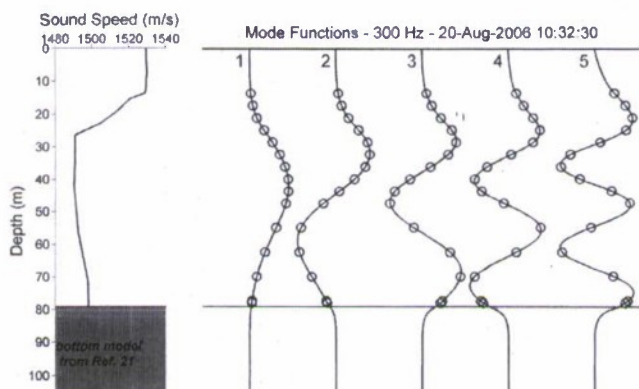


FIG. 12. Estimates of the mode functions of frequency 300 Hz at the location of WHOI VLA at 10:32:30 GMT on August 20 in the SW06 experiment. The *in situ* water-column sound speed profile and a bottom model derived from Ref. 21 are used for calculating the modes. The circles on the curves indicate the hydrophone depths on the VLA.

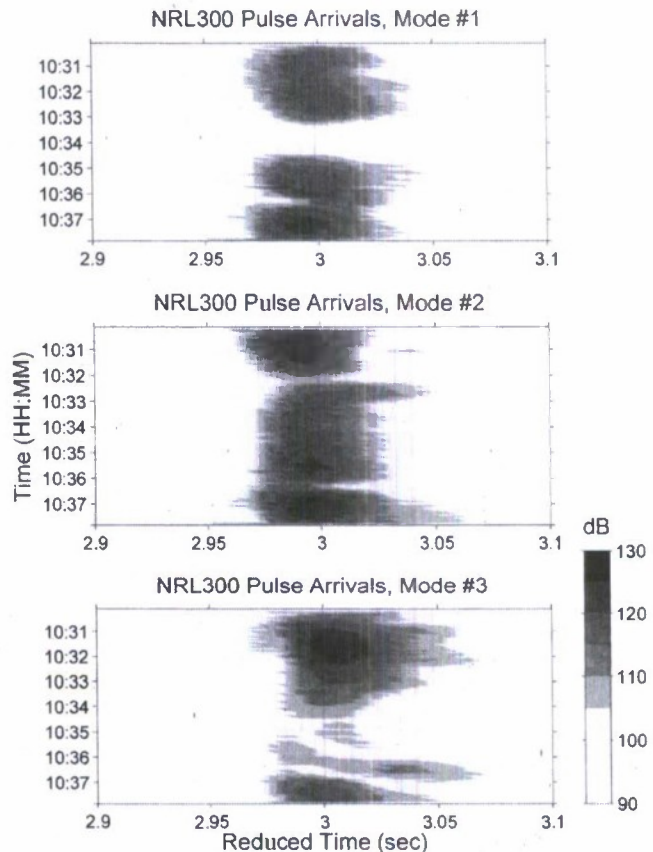


FIG. 13. (Color online) Broadband mode-filtered outputs of the received NRL300 pulses on the WHOI VLA during the truncated internal-wave event on August 20 in the SW06 experiment. The first three modes are shown, and a total of 110 pulses is analyzed. The mode intensities fluctuate in time.

numerical approaches. A 3D normal mode solution has been derived to describe the radiation field in a simplified truncated internal-wave duct model, and a computer code implementing 3D PE approximation is employed to investigate the radiation effects in a more realistic shallow-water ocean environment. Both of the analytical and numerical calculations predict anomalous sound radiation fields at locations far from the termination of a truncated internal-wave duct. The radiation patterns are unique to each mode and show strong spatial and temporal variability. The studies also show that the cause of this is a strong dependence on the position of an acoustic source in the duct, which changes in time for a moving wave and a moving or fixed source. Broadband simulations made in this paper reveal situations where one or more modes are completely absent on a fixed VLA because the strongly localized modal radiation beams cannot just reach the fixed array and mode multipath arising from dispersive propagation within the horizontal waveguide.

ACKNOWLEDGMENTS

The 3D PE program used in this paper was derived from a trial version written by Dr. John Colosi of the Naval Postgraduate School, CA, USA, and the authors acknowledge his valuable efforts to the original code. The authors must also thank all of SW06 participants for their efforts to make this large multi-disciplinary shallow-water ocean experiment suc-

cessful; heartfelt thanks must be offered to the acoustics and physical oceanography program managers from the Office of Naval Research (ONR), Ellen Livingston and Terry Paluszkiwicz, for their support. This work was supported under ONR Grant No. N00014-05-1-0482 and the ONR postdoctoral fellowship award, Grant No. N00014-08-1-0204.

- ¹B. G. Katsnel'son and S. A. Pereselkov, "Low-frequency horizontal acoustic refraction caused by internal wave solitons in a shallow sea," *Acoust. Phys.* **46**, 684–691 (2000).
- ²R. Burridge and H. Weinberg, "Horizontal rays and vertical modes," in *Wave Propagation and Underwater Acoustics*, edited by J. B. Keller and J. S. Papadakis (Springer, Berlin, 1977), pp. 86–152.
- ³R. Oba and S. Finette, "Acoustic propagation through anisotropic internal wave fields: Transmission loss, cross-range coherence, and horizontal refraction," *J. Acoust. Soc. Am.* **111**, 769–784 (2002).
- ⁴D. Lee and M. H. Schultz, *Numerical Ocean Acoustic Propagation in Three Dimensions* (World Scientific, Singapore, 1995).
- ⁵S. Finette and R. Oba, "Horizontal array beamforming in an azimuthally anisotropic internal wave field," *J. Acoust. Soc. Am.* **114**, 131–144 (2003).
- ⁶M. Badiey, B. G. Katsnel'son, J. F. Lynch, S. Pereselkov, and W. L. Siegmman, "Measurement and modeling of three-dimensional sound intensity variations due to shallow-water internal waves," *J. Acoust. Soc. Am.* **117**, 613–625 (2005).
- ⁷S. D. Franks, M. Badiey, J. F. Lynch, and W. L. Siegmman, "Experimental evidence of three-dimensional acoustic propagation caused by nonlinear internal waves," *J. Acoust. Soc. Am.* **118**, 723–734 (2005).
- ⁸D. B. Reeder, T. F. Duda, and B. Ma, "Short-range acoustic propagation variability on a shelf area with strong nonlinear internal waves," in *Oceans'08 (Kobe) Conference Proceedings* (IEEE, New York, 2008).
- ⁹C. R. Jackson, *An Atlas of Internal Solitary-Like Waves and Their Properties*, 2nd ed. (Global Ocean Associates, Alexandria, VA, 2004) (available at http://www.internalwaveatlas.com/Atlas2_index.html (Last viewed 6/17/2009)).
- ¹⁰T. F. Duda, "Initial results from a Cartesian three-dimensional parabolic equation acoustical propagation code," Technical Report No. WHOI-2006-041, Woods Hole Oceanographic Institution, Woods Hole, MA, 2006.
- ¹¹D. J. Tang, J. N. Moum, J. F. Lynch, P. Abbot, R. Chapman, P. H. Dahl, T. F. Duda, G. Gawarkiewicz, S. Glenn, J. A. Goff, H. Graber, J. Kemp, A. Maffei, J. D. Nash, and A. Newhall, "Shallow Water '06, A joint acoustic propagation/nonlinear internal wave physics experiment," *Oceanogr.* **20**, 156–167 (2007).
- ¹²J. C. Preisig and T. F. Duda, "Coupled acoustic mode propagation through continental-shelf internal solitary waves," *IEEE J. Ocean. Eng.* **22**, 256–269 (1997).
- ¹³J. Zhou, X. Zhang, and P. H. Rogers, "Resonant interaction of sound wave with internal solitons in the coastal zone," *J. Acoust. Soc. Am.* **90**, 2042–2054 (1991).
- ¹⁴H. Levine and J. Schwinger, "On the radiation of sound from an unflanged circular pipe," *J. Acoust. Soc. Am.* **73**, 383–405 (1948).
- ¹⁵F. B. Jensen, W. A. Kuperman, M. B. Porter, and H. Schmidt, *Computational Ocean Acoustics* (AIP, Woodbury, NY, 1994).
- ¹⁶G. V. Frisk, *Ocean and Seabed Acoustic: A Theory of Wave Propagation* (Prentice-Hall, Englewood Cliffs, NJ, 1994).
- ¹⁷R. H. Hardin and F. D. Tappert, "Applications of the split-step Fourier method to the numerical solution of nonlinear and variable coefficient wave equations," *SIAM Rev.* **15**, 423 (1973).
- ¹⁸D. J. Thomson and N. R. Chapman, "A wide-angle split-step algorithm for the parabolic equation," *J. Acoust. Soc. Am.* **74**, 1848–1854 (1983).
- ¹⁹T. F. Duda, "Analysis of finite-duration wide-band frequency sweep signals for ocean tomography," *IEEE J. Ocean. Eng.* **18**, 87–94 (1993).
- ²⁰M. B. Porter, "The KRAKEN normal mode program," SACLANTECN Memorandum No. SM-245 (SACLANT Undersea Research Centre, La Spezia, Italy, 1991).
- ²¹Y.-M. Jiang, N. R. Chapman, and M. Badiey, "Quantifying the uncertainty of geoacoustic parameter estimates for the New Jersey self by inverting air gun data," *J. Acoust. Soc. Am.* **121**, 1879–1894 (2007).
- ²²T. F. Duda, "Examining the validity of approximations to fully three-dimensional shallow-water acoustic propagation through nonlinear gravity waves," in *Oceans'07 (Aberdeen) Conference Proceedings* (IEEE, New York, 2007).
- ²³W. M. Carey, J. Doult, R. B. Evans, and L. M. Dillman, "Shallow-water sound transmission measurements on the New Jersey continental shelf," *IEEE J. Ocean. Eng.* **20**, 321–336 (1995).
- ²⁴R. J. Cederberg, W. M. Carey, and W. L. Siegmman, "Modal analysis of geoacoustic influences on shallow-water propagation," *IEEE J. Ocean. Eng.* **22**, 237–244 (1997).
- ²⁵J. M. Collis, T. F. Duda, J. F. Lynch, and H. A. Deferrari, "Observed limiting cases of horizontal field coherence and array performance in a time-varying internal wave field," *J. Acoust. Soc. Am.* **124**, EL97–EL103 (2008).

Shallow Water '06

A Joint Acoustic Propagation/ Nonlinear Internal Wave Physics Experiment

BY DAJUN TANG, JAMES N. MOUM, JAMES F. LYNCH, PHIL ABBOT, ROSS CHAPMAN,
PETER H. DAHL, TIMOTHY F. DUDA, GLEN GAWARKIEWICZ, SCOTT GLENN, JOHN A. GOFF,
HANS GRABER, JOHN KEMP, ANDREW MAFFEI, JONATHAN D. NASH, AND ARTHUR NEWHALL

SINCE THE END of the Cold War, the US Navy has had an increasing interest in continental shelves and slopes as operational areas. To work in such areas requires a good understanding of ocean acoustics, coastal physical oceanography, and, in the modern era, autonomous underwater vehicle (AUV) operations.

Each area presents challenges for both the scientist and the Navy. In physical oceanography, a complex interplay among winds, rivers, tides, and local bathymetry drives a nonstationary, shelf-break front and the nonlinear internal wave (NLIW) field. These strongly affect acoustic systems but are not adequately understood. A key oceanographic challenge is to model the fully four-dimensional ocean from the large-scale circulation down to fine scales, which include NLIW packets, internal tides, jets, and density fronts. Both Navy

acoustics systems and Navy operations need the "local ocean weather" as well as the "ocean climate" as part of the routine forecast, but the former is not yet available.

In ocean acoustics, the Navy wishes to operate both at low frequencies (100–1000 Hz) and mid frequencies (1000–10,000 Hz), which poses questions on a variety of spatial and temporal scales. For low-frequency acoustics, it has become obvious that fully three-dimensional (spatial) oceanography is necessary for propagation prediction. A bit more surprisingly, it appears that fully three-dimensional (spatial) acoustics codes might be necessary as well, a big divergence from the two-dimensional slice between source and receiver that has been adequate for ocean acoustics to date. At medium frequency, the effects of NLIWs on sonar systems are predicted

to be large and critical, but precious little experimental data combining acoustics with a well-characterized coastal ocean is to be found. Another challenge is to try to extrapolate the routinely measured "single bounce" acoustic paths (those with one surface or bottom interaction) to predict how multiple-bounce sonar systems would perform.

In using autonomous vehicles, rapidly and efficiently sampling the oceanography, particularly the temperature field, so as to optimize the placement and performance of acoustics systems is a major technical hurdle to be cleared. The Navy is increasingly interested in using AUVs and gliders for such work, as they can operate persistently over large areas, comparatively inexpensively.

To pursue these questions, the Office of Naval Research (ONR) sponsored a large, multidisciplinary, multi-

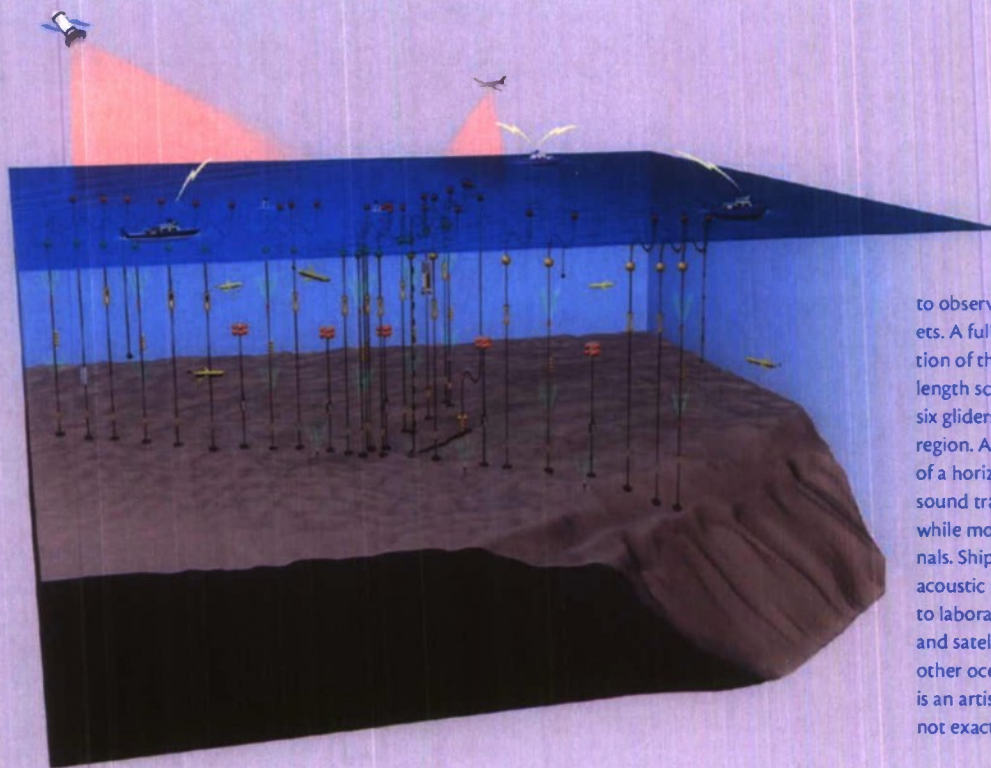


Figure 1. A graphic overview of the SW06 experiment. Moored instrumentation is deployed in lines in the along-shelf and across-shelf directions to observe shelf-break front and internal wave packets. A fully three-dimensional array at the intersection of the "T" is designed to study the wave-front length scales of nonlinear internal waves. A fleet of six gliders monitors mesoscale oceanography in the region. An "L"-shaped array of hydrophones consists of a horizontal and a vertical line array, and monitors sound transmissions throughout the experiment, while moored and shipboard sources transmit signals. Ships carry out oceanographic, geologic, and acoustic research while networked to each other and to laboratories ashore to share information. Planes and satellites overhead image internal waves and other ocean processes. The bathymetry in the figure is an artist's rendition showing generally correct but not exact features.

institution, multinational experiment off the coast of New Jersey in summer 2006, designated "Shallow Water '06" (SW06). This large-scale experiment had three named components corresponding to the three major research and technology thrusts: in acoustics, LEAR (for Littoral Environmental Acoustics Research); in physical oceanography, NLIWI (the Non Linear Internal Waves Initiative); and in vehicles, AWACS (for Acoustic Wide Area Coverage for Surveillance).

EXPERIMENTAL SETUP AND LOGISTICS

Over its two-month duration (mid-July to mid-September), the SW06 experiment entrained enormous resources: seven ships, 62 moorings, aircraft overflights and satellite coverage, a fleet of ten oceanographic gliders, data-assimilating numerical modeling,

real-time data communication from a number of shipboard experiments, and dozens of principal investigators tending to their parts of this coordinated effort.

Two of the logistical components of this effort merit special attention due to their sheer size and novelty: (1) mooring layout, construction, deployment, and recovery, and (2) real-time data and experiment-status communications via the SW06 Web site.

Moorings

The core measurement suite of the SW06 experiment was an array of 62 acoustics and physical oceanography moorings (57 long term, 5 short term) that were deployed in a "T" geometry, with the stem of the T stretching 30 km along-shelf at the 80-m isobath, and the top of the T stretching 50 km across-shelf from the 500-m isobath to the 60-m isobath

(see Figure 1). The geometry and placement of the T were arranged to provide good along- and across-shelf views of the shelf-break front, the local eddy field, and the nonlinear internal wave field, three oceanographic quantities of primary interest. A small ($10 \times 10 \text{ km}^2$) moored oceanography array was placed at the crossing of the T to look at fully three-dimensional (spatially) nonlinear internal wave structure.

The T geometry was very efficient for notifying fishermen and other mariners where our equipment was located—we simply had to specify the endpoints and crossing of the T. As a result, no gear was lost to fishing activity. Amazingly, we recovered every mooring that we deployed, with about 95% data return, despite having one lithium battery pack explode and one mooring drift out to sea after Hurricane Ernesto.

Web Site

New challenges in the area of oceanographic experiment logistics, real-time field communication, and data fusion and exchange led to the creation of Web-based software tools to enable coordinated, real-time collaboration between researchers at sea and ashore. SW06 researchers could monitor the location of several ships, dozens of moorings,

deployment; ship, glider and aircraft tracks; daily reports; weather information; CODAR (Coastal Ocean Dynamics Applications Radar) and satellite imagery; and ocean-model results. These Web tools allowed us to collect and organize this information into a usable form, and also provided a searchable, time-based archive of the entire experiment. The development of these tools was an

SW06 researchers could monitor the location of several ships, dozens of moorings, assorted underwater vehicles, and other platforms in near real time.

assorted underwater vehicles, and other platforms in near real time. Information gathered off the Internet was merged with information collected during operations at sea and inserted into a basic framework to provide additional support. A primarily wireless network comprised of satellite, shipboard, and global Internet links was used to synchronize Web sites on five ships and multiple shore-based servers so that all participants in the experiment could contribute and monitor platform locations/

important contribution to the experiment, providing the means for using research vessels on scientific expeditions as parts of a real-time ocean observatory.

PHYSICAL OCEANOGRAPHY (NLIWI)

One of the principal foci of the experiment was internal waves. These come in two general types: (1) linear internal waves that include long-wavelength (tens of kilometers) entities such as internal tides and near-inertial waves, and follow

a linear wave equation, and (2) nonlinear internal waves that have short length scales (hundreds of meters), are characterized by large particle velocities, and follow nonlinear wave equations such as the Korteweg-deVries equation. These nonlinear waves have a large acoustical effect, and we now know that they can be found all over the world's ocean shelves. Indeed, they are nearly as common as surface waves, given stratified waters.

Internal-wave activity on the New Jersey slope is particularly well documented through both satellite synthetic aperture radar (SAR) imagery (Jackson and Apel, 2004) and previous in situ experiments (Apel et al., 2006). SAR imagery clearly reveals the surface signatures of wave packets (Figure 2) that appear to originate near the shelf break and propagate shoreward. But this picture is not a totally simple one. Irregular bathymetry near the shelf break, such as canyons, can produce circular wave fronts that combine with the planar ones from the shelf break and with each other. Along the New Jersey coast, the ambient stratification is also complicated by the existence of a shelf-break front (a salinity-density front/current combination that meanders near the shelf edge), the frequent presence of warm-

DAJUN TANG is Senior Engineer, Applied Physics Laboratory, University of Washington, Seattle, WA, USA. JAMES N. MOUM is Professor, Oregon State University, Corvallis, OR, USA. JAMES F. LYNCH (jlynch@whoi.edu) is Senior Scientist, Woods Hole Oceanographic Institution, Woods Hole, MA, USA. PHIL ABBOT is President, OASIS, Inc., Lexington, MA, USA. ROSS CHAPMAN is Professor, University of Victoria, Victoria, British Columbia, Canada. PETER H. DAHL is Principal Engineer, Applied Physics Laboratory, University of Washington, Seattle, WA, USA. TIMOTHY F. DUDA is Associate Scientist, Woods Hole Oceanographic Institution, Woods Hole, MA, USA. GLEN GAWARKIEWICZ is Senior Scientist, Woods Hole Oceanographic Institution, Woods Hole, MA, USA. SCOTT GLENN is Professor, Rutgers University, New Brunswick, NJ, USA. JOHN A. GOFF is Senior Research Scientist, University of Texas at Austin, Austin, TX, USA. HANS GRABER is Professor, University of Miami, Miami, FL, USA. JOHN KEMP is Senior Engineering Assistant II, Woods Hole Oceanographic Institution, Woods Hole, MA, USA. ANDREW MAFFEI is Senior Information Systems Specialist, Woods Hole Oceanographic Institution, Woods Hole, MA, USA. JONATHAN D. NASH is Associate Professor, Oregon State University, Corvallis, OR, USA. ARTHUR NEWHALL is Information Systems Specialist, Woods Hole Oceanographic Institution, Woods Hole, MA, USA.

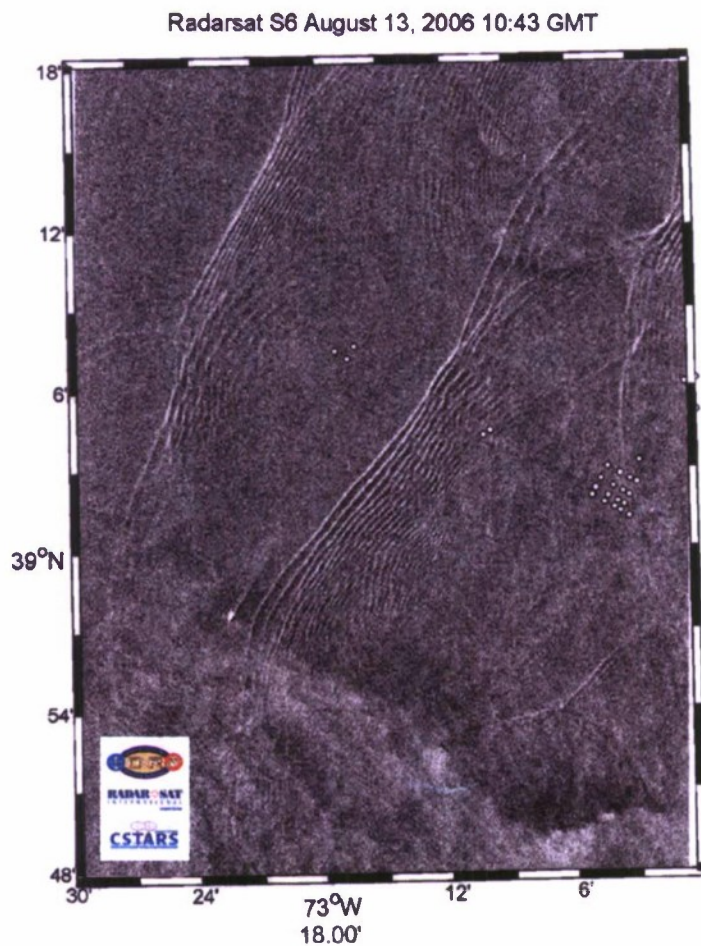


Figure 2. Radarsat observation from August 13, 2006. Part of the across-shelf mooring array is shown in the figure to provide scale. The structure of the nonlinear internal wave packets, including some pronounced curvature of the wave fronts, is clearly visible. Understanding the correlation of these surface images with subsurface observations is one of the objectives of SW06.

core eddies shed from the Gulf Stream, strong freshwater influences, near-inertial wave activity, and the frequent passage of tropical storms. The complexity that all this variability induces into the internal wave field is important to acoustics. As a matter of physical oceanography/acoustics synergy, the suite of moored instruments was designed not only to focus on fundamental aspects of internal-wave physics but also to support the acoustics measurements by

defining both the space/time variability of the sound-speed field and the propagation of individual nonlinear internal wave trains through the acoustics array. Numerous local shipboard measurements were made to investigate the evolving wave structure and energetics and to support short-range acoustics experiments. A considerable modeling effort combining oceanography, acoustics, and Navy needs augments these observations. These models encompass

mesoscales to NLIW scales, representing an ambitious drive to cover yet more of the full-ocean spectrum with data-assimilating models.

From an observational perspective, the primary objectives were (1) to understand and describe the two- and three-dimensional structures of NLIWs in sufficient detail to aid in improving wave models beyond small-amplitude wave theories that are inadequate but still in use, (2) to define the energy evolution and transport, and (3) to identify wave-generation sites, times, and mechanisms. These are all necessary for prediction of wave generation and propagation over the continental shelf. In addition, important efforts include a quantitative physical assessment of surface radar signatures in terms of small-scale sea-surface variability.

Background Oceanographic Conditions and Nonlinear Internal Waves in SW06

While NLIWs appear like clockwork in some parts of the world's ocean (like the South China Sea; Ramp et al., 2004), prediction of the nonlinear internal wave climate over continental shelves is notoriously difficult. During SW06, NLIW packets were observed at all phases of the barotropic tide. This variability in the timing of waves is not unlike previous continental shelf observations (Colosi et al., 2001; Moum et al., 2007). More importantly, and entirely counter to our expectations, larger and more frequent waves appeared during neap tides than during spring tides (which peaked on 11 August). One of the more interesting challenges posed by our data will be to reconcile this curious observation with our initial expectations.

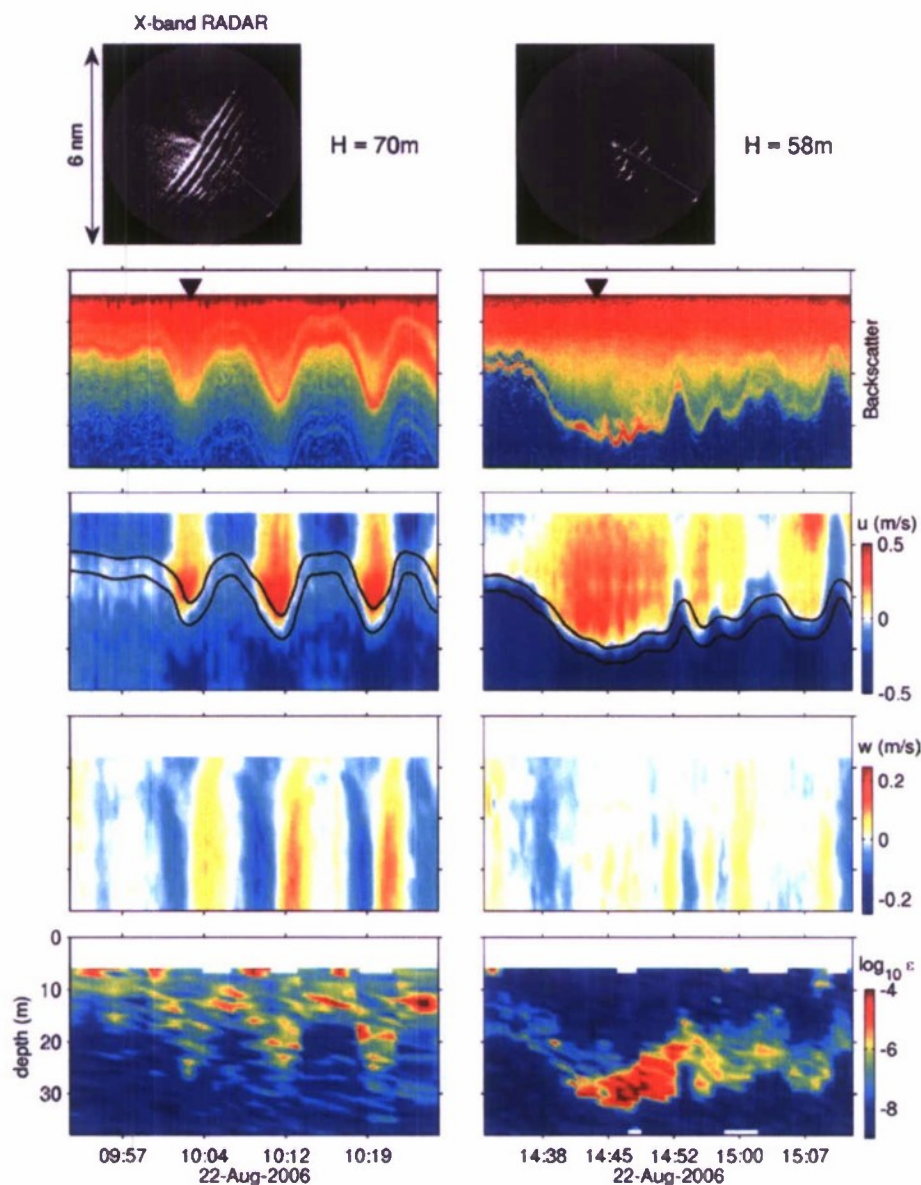


Figure 3. Detailed acoustic backscatter, velocity (components shown are in the direction of wave propagation, u , and vertical, w), and turbulence (ϵ) observations of a nonlinear internal wave packet tracked by R/V *Oceanus* while propagating onshore over the New Jersey shelf during SW06. Two isopycnals are plotted over the u image. The two columns show two stages of wave-packet evolution. During the 5-h separation between these observations, the wave propagated 17 km (wave speed $\approx 0.8 \text{ m s}^{-1}$), or almost 100 wavelengths. The wave-packet evolution is significant; it changes from a well-defined set of radar wave fronts and an internal velocity/density structure that is clearly representative of solitary-like waves to a less-ordered structure marked by extreme turbulence at the base of its velocity core. This in turn is associated with what appear to be small-scale Kelvin-Helmholtz billows (as seen in the acoustic backscatter). These observations were made using shipboard acoustics and the Chameleon turbulence profiler. Figure courtesy Emily Shroyer, Oregon State University

Observations

Intensive moored observations were designed to capture both mesoscale oceanography and the high-frequency wave climate. Water-column velocity, temperature, and salinity were measured with $\sim 10\text{-m}$ resolution from ten dedicated oceanography moorings. Five bottom landers were deployed at 70-, 80-, 85-, 110-, and 125-m water depths to measure near-bottom density, pressure, and turbulence as well as full-water-column velocity structure at 5-s intervals. Two Air-Sea Interaction Spar (ASIS) buoys were deployed at 70- and 80-m water depths to measure atmospheric conditions, to quantify the surface gravity wave field, and to measure near-surface currents and density. Most instruments were sampled at 30-s intervals to resolve high-frequency waves.

Multiple ships were used to chase wave packets across the continental shelf, hopefully from their birth sites to their death sites. Shipboard experiments to track evolving wave groups, including slalomming through the three-dimensional moored array cluster, were conducted from R/Vs *Endeavor* and *Oceanus*. These observations included acoustic Doppler current profilers sampled at high spatial and temporal resolution (to map the NLIW velocity field in detail) and in situ measurements of temperature, salinity, and small-scale turbulence. Highly detailed depictions of wave groups obtained (Figure 3) from these data show the evolving structures of individual waves and how their relative positions within wave groups change as they propagate onshore. Shipboard wave tracking also provided clear observations of so-called “varicose” (mode-2) waves in a geophysical fluid (that is, waves that

both elevate isopycnals above a density interface and depress them below) and the change in sign from depression waves to elevation waves as they shoal.

Shipboard observations also included X-band radar measurements of the sea surface (Figure 3). These records provided depictions of the wave fronts over 3-nm ranges from the ships, extending our understanding of the shapes of the wave fronts beyond their points of intersection with the ships. Wave-front shapes were tracked even further by aircraft radar flights and satellite SAR observations. One of the challenges of NLIWI will be to obtain a first-order understanding of the structure of the evolving wave fronts.

To monitor the critical mesoscale variability, a suite of 10 gliders was deployed with the goal of continually flying six of these through the moored array, a goal that was largely achieved. These observations were augmented by Scanfish surveys extending across the shelf and over the continental slope to provide a broad perspective of the variability of the shelf-

swept acoustics system of four transducers to remotely detect the spectrum of backscattering generated by small-scale sound speed microstructure created by turbulence instabilities within waves.

This measurement augments profiling observations of turbulence by providing a continuous sequence between profiles. It also helps to identify the detailed physical structure of the waves.

High-resolution pressure sensors were deployed on three bottom landers along the array. Results show that the seafloor pressure signal of the NLIWs observed by other means during SW06 is measurable (Moum and Nash, in press). This relatively simple measurement suggests new ways to design NLIW detection antennae.

Modeling

Modeling of currents and stratification (including sound speed) from the synoptic to the wave scale is ongoing. At large scales, the Regional Ocean Modeling System assimilated data from all platforms to provide real-time maps of the relevant fields. At intermediate

the modelers is to represent the sound-speed field from the mesoscale to the small-scale fluctuations caused by the nonlinear waves.

GEOLOGY (LEAR)

The seabed forms the bottom boundary condition for shallow-water acoustic and oceanographic experiments, such as SW06. While understanding the acoustic properties of the seabed is of obvious importance to the acoustic experiments, and the bathymetry and roughness is important to the oceanography, we also seek a geologic understanding of the sediments and the stratigraphic geometries in which they were deposited. This type of information provides context for understanding the results and for applying what we learned to other areas. The stratigraphic geometries can help guide extrapolation of bottom inverse results from one location to other parts of the survey region.

One of the big attractions of the SW06 area was the fact that, in addition to having interesting physical oceanography, the seabed had been examined and characterized by previous experiments, thus saving a large amount of effort and money. Any further geological work and stratigraphic surveying would be answering more detailed questions about the bottom, in accord with SW06's status as a "higher-order effects" type of experiment, not an initial survey.

Much of the previous geological work in this area was sponsored by ONR, in large part as a response to a system of buried, remnant river channels just below the seafloor that were suspected to be the sources of "geo-clutter" (false target backscatter returns due to geology) in Navy sonar systems. Such buried chan-

The seabed forms the bottom boundary condition for shallow-water acoustic and oceanographic experiments, such as SW06.

break front and other mesoscale variations in currents, temperature, and salinity. Author Abbot and co-investigators are preparing a WHOI technical report on these surveys.

Two new types of observations were exploited to investigate the NLIWs. One of these was deployed from a ship and used a broadband (120–600 kHz)

scales, the nonhydrostatic MIT general circulation model was nested within the larger model to provide clues as to how the observed NLIWs are generated. At the scale of the waves, a novel model based on optimized mesh-point placement provides detailed simulations of small-scale tide-topography interaction and wave generation. The challenge to

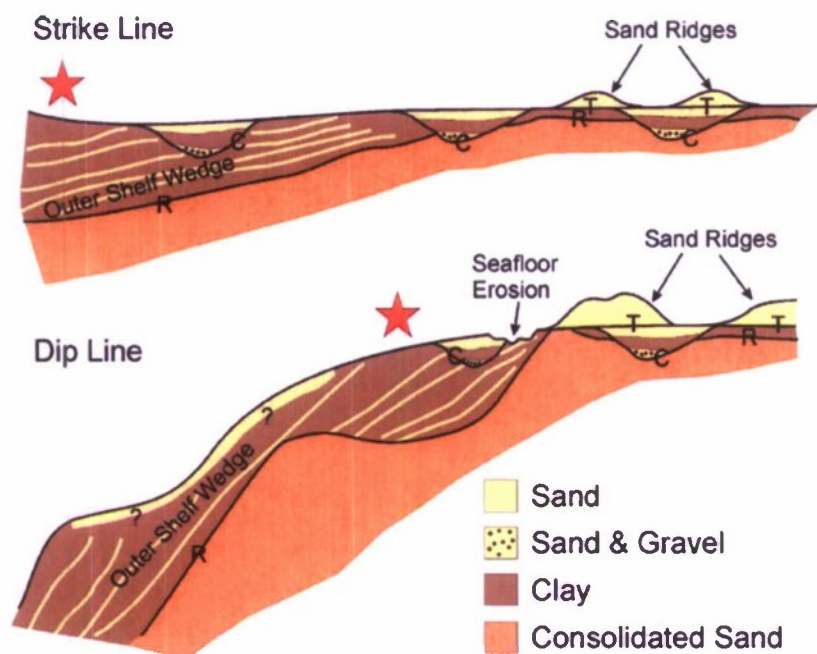


Figure 4. Schematic representation of stratigraphic elements along the strike-and-dip lines (Figure 5) of the SW06 experiment. The strike of a stratum is a line representing the intersection of that feature with the horizontal; the dip is the angle below the horizontal of a tilted stratum. The star represents the approximate location of the "cross-hairs" of the SW06 experiment.

nels are quite common on continental shelves, and so the New Jersey shelf provided a natural laboratory for looking at this effect. The interested reader can find the history of this fascinating work in the following references: initial mapping of fluvial channels (Davies et al., 1992); multibeam surveys and bathymetry (Goff et al., 1999); geophysical and geological sample data (e.g., Goff et al., 2004; Nordfjord et al., 2005, 2006); and long-coring efforts (Nordfjord et al., 2006). As a postscript, it was found that the "geo-clutter," though appreciable, was often swamped by "bio-clutter" (i.e., reverberation returns from schools of fish on the shelf and often near the shelf break [Makris et al., 2006]). A large ONR experiment to study this type of clutter was initiated as a result.

Though our understanding of the

overall geologic history of the SW06 region has grown immeasurably (e.g., Duncan et al., 2000; Goff et al., 2005; Gulick et al., 2005; Nordfjord et al., 2006), major gaps still remain. The "R" horizon is the most prominent and widespread feature in the shallow subsurface (e.g., Milliman et al., 1990; Gulick et al., 2005; Figure 4). We know from sampling and age dating that it is approximately 40,000 years old, but the reasons for its existence are still the subject of much speculation. The new SW06 chirp data and future long coring should provide critical new morphologic and stratigraphic constraints on the origin of R. Lying on top of R is the outer-shelf wedge, composed of alternating layers of sand and mud that are imaged as numerous layered reflections in chirp seismic data. These sediments were most likely

deposited as sea level was falling in the lead-up to the last glacial maximum. In some locations, most notably the central site of the SW06 experiment, the top of the layered outer shelf wedge is very erose, cut by grooves oriented ~ east-west, and then filled with sediments that are acoustically transparent (Fulthorpe and Austin, 2004). This surface may be evidence of some sort of catastrophic flood event, or perhaps the grooves were created by icebergs grounding along an ancient seabed. New core samples should help us to resolve the origin of this boundary.

At some time during the last glacial maximum, while sea level was much lower and almost the entire continental shelf was exposed, dendritic networks of river channels were carved into the mid-shelf wedge (the "C" horizon in Figure 4) and, where the wedge thinned, through R as well. When sea level subsequently rose following the melting of the ice-age glaciers, the channels were filled by a sequence of estuarine sediments: a fluvial lag of sand and gravel at the base, followed by muddy sediments deposited where the river met the tide, followed by beach barrier sands (Nordfjord et al., 2006). These sediments, ~ 12,000 years old in the SW06 region, form recognizable layers in the chirp seismic record of the channel-fill sediments. Continued sea-level rise caused the shoreline to pass over the buried channels, creating a widespread erosion surface referred to as the "T" horizon. Large sand bodies formed in the nearshore environment on top of T, and these were shaped into large bedforms (~ 1–5 m high, 1–4 km wide, and 2–10 km long) called sand ridges. These features are so large that they persist to the present day and can be easily mapped

in the multibeam bathymetry data. But the seabed does not become quiescent with increasing water depth. Evidence in the multibeam and chirp data suggests widespread regions of recent and modern erosion, which has removed the sand sheet in many places, exposing both the T and the R horizons at the seafloor. The result is a seabed with highly variable sedimentary and physical properties, which will be of great importance to the SW06 acoustics experiment results.

ACOUSTICS (LEAR)

Though acoustics was the largest overall component of SW06, it makes sense to discuss it after the oceanography and geology, as these set the context for acoustic propagation and scattering. The SW06 experiment had both low-frequency (100–1000-Hz) and medium-frequency (1000–10,000-Hz) components, and examined issues in forward propagation, scattering, and inverse theory.

Low-Frequency Propagation

In doing the acoustics transmissions, we used both moored and shipboard sources and receivers. The primary moored receiver site for propagation studies was at the along/across-shelf intersection of the T-shaped mooring, as that is where we have the best oceanographic information. At that site, a long-term horizontal/vertical line array with 48 hydrophone channels was deployed, sampling sound from 50–4500 Hz continuously over a six-week period. This array was augmented by other receivers, (mostly) near the same site, as well as five long-term “single hydrophone receiver units” distributed along the across-shelf line. The moored sources were arranged on the along- and across-shelf lines as well, as these are where we had the best environmental support, and, also, these were “limiting cases” for the azimuthal variations of the acoustic path. These moored sources were augmented by some shipboard sources,

which allowed us to fill in the azimuthal propagation direction spectrum.

There are a number of open questions about low-frequency, shallow-water propagation. One of the most interesting of these concerns the azimuthal dependence of shallow-water sound propagation, specifically its strong dependence upon the angle between the acoustic path and the propagation direction of the nonlinear internal wave field (when present). Sound can travel readily in the acoustic duct that is created between individual soliton packet waves, in a manner that keeps the acoustic modes separate and distinct. This leads to higher-intensity regions of the acoustic field, as seen in the top panel of Figure 5. On the other hand, sound that travels perpendicular to the propagation direction of the nonlinear internal waves suffers intense coupling between the modes, which can lead to the severe attenuation of sound (depending upon where one places the source relative to the sur-

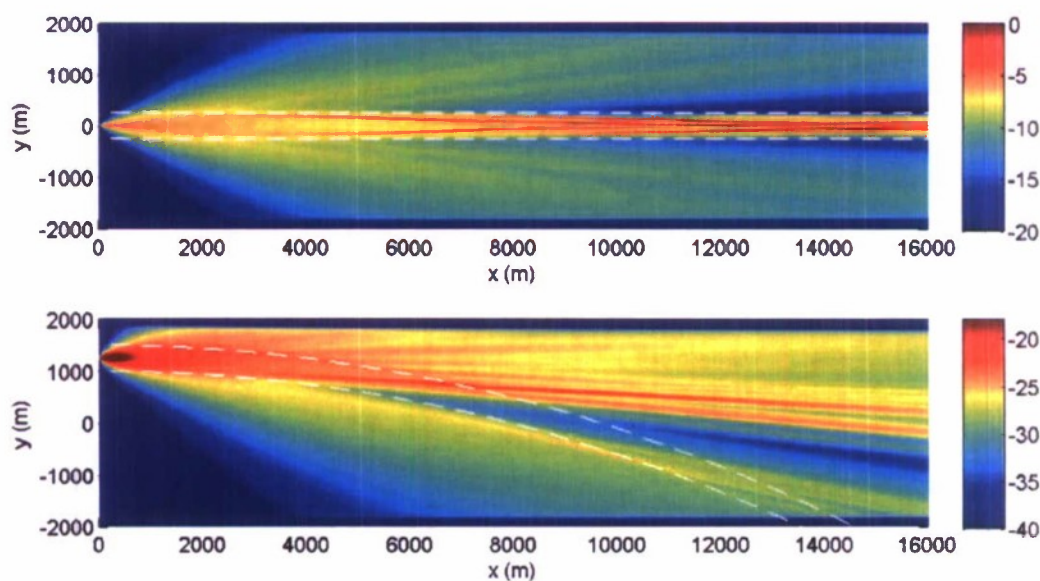


Figure 5. The top panel shows, in a top view, a computer model of ducting of sound between nonlinear internal wave crests (denoted by white dashed lines), a known and experimentally observed phenomenon. The bottom panel shows a top view of the ducting and horizontal dispersion of sound between two curved nonlinear internal wave crests, an effect that should be observable and provable using the SW06 data set. Color gradation denotes (relative) intensity in dB.

face mixed layer and thermocline.) At angles intermediate to these extremes, a combination of these effects occurs, and we presently have a rather limited ability to predict the acoustic field for this case due to both oceanographic and acoustic complexity.

Another interesting question about acoustic propagation in shallow water is how much energy is reflected out of plane by internal waves and coastal fronts when the acoustic path is at low (grazing-angle) incidence to these ocean features. The interference of a straight acoustic track (that does not interact with these ocean features) and a reflected path can cause very large, fully three-dimensional acoustic fluctuations, as have been seen in numerous computer simulations. Verification (or refutation) of such effects is an interesting experimental question, and data from SW06 should shed light on this. Yet another question of great interest to LF acoustics is how the three-dimensional irregularity of fronts and the curvature of nonlinear internal waves (which are often taken as two-dimensional, along-shelf symmetric entities to first order) affect acoustic propagation. There is an example of curvature effects in the bottom panel of Figure 5. These curvature effects can lead to both horizontal ducting and horizontal dispersion of sound rays (or "light pipe" and "rainbow" effects in optical parlance), and, in terms of Navy systems, false target bearings, a major concern.

Medium-Frequency Propagation

Many practical sonar systems operate in the mid-frequency band between 1 and 10 kHz. In shallow-water regions, the performance of such systems is strongly influenced by the bottom, sea surface,

and water column. This influence can be in the form of sound scattering, refraction, and attenuation. Uncertainties in any or all of these categories are common, so knowing the various mechanisms governing acoustic interaction with the environment is essential to improving sonar performance in shallow water. To gain quantitative understanding of how sound interacts with these environmental factors, it is essential to measure all relevant environmental parameters at sufficient spatial and temporal resolutions, which can be quite fine for mid-frequency acoustics.

The mid-frequency efforts of SW06/LEAR were concentrated on receiving arrays moored in the central area, where the water depth is about 80 m. Five major measurements were made there: (1) short-range acoustics interaction with the bottom and surface, (2) in situ measurement of sediment sound speed to a depth of 1.7 m, (3) bottom backscatter, (4) short-range propagation through known internal waves, and (5) long-range propagation to 10 km along the

MORAY1 receiving array from a source deployed from R/V *Knorr*, within the frequency range 1–20 kHz. A second measurement transmitted both mid- and low-frequency sound (0.05–4 kHz) at a range of 200 m around a circular path encompassing the MORAY1 location.

A new sediment acoustics measurement system (SAMS) was developed to measure in situ sediment sound speed to a depth of 1.7 m with 0.1 m depth increments. This is accomplished by using a vibro-core fitted with a hydrophone at its tip to penetrate into the bottom in controlled depth-steps while 10 acoustic sources located above the bottom transmit sound in the band of 2–35 kHz. This source-and-receive arrangement provides many ray paths crisscrossing the sediment volume, so sediment sound speed as a function of depth is directly imaged.

Bottom backscatter in the frequency band of 3–10 kHz was measured by both a parametric source and by an omnidirectional source combined with a 32-element, vertical-line hydrophone array. Supporting this effort, sediment

A major objective in SW06 was to estimate
the regional geoacoustic environment using
the best present-day inversion techniques.

same track with multiple source depths, frequency bands, and different times.

To study bottom and surface reflection coefficients and their anisotropy, short-range bottom/surface interaction measurements were first made at ranges from 50 m to 1000 m from multiple directions with respect to the moored

roughnesses were measured using a sediment conductivity probe that can measure one-dimensional roughness to a resolution of 10 mm in the horizontal direction and 1 mm in the vertical. In addition, a laser scanner was also deployed to provide two-dimensional roughness measurements to a resolu-

tion of 1 mm in both the horizontal and vertical directions.

The effect of nonlinear internal wave trains on mid-frequency sound propagation was measured with the goal of making deterministic assessment of the impact by taking “snap shots” of the internal waves along the acoustic path. This was accomplished by a transmission from a source deployed from R/V *Knorr* to the MORAY1 receiving array stationed 1000 m away. A CTD chain with 50 elements was towed at 6 kt in the vicinity of the source and receiver by a second ship, R/V *Endeavor*. Both acoustics and CTD-chain measurements were made in the presence and absence of internal waves, so the impact of internal waves on mid-frequency sound propagation can be quantitatively evaluated.

Finally, mid-frequency, long-range propagation to a 10-km range along the same track on different days with different bandwidths was studied. This research focused on the temporal variability of propagation loss, and also bottom parameter inversion and mode stripping due to surface scattering.

Low- and Medium-Frequency Bottom Inverses

Underwater acousticians often use “geoacoustic models” (local sediment layers described by their density, compressional and shear wave speeds, and attenuations) to characterize the bottom for making predictions of the sound levels in the sea. A major objective in SW06 was to estimate the regional geoacoustic environment using the best present-day inversion techniques. Several groups collaborated in experiments that used sound sources over a broad band of frequencies to characterize the bot-

tom, especially at sites where there was extensive geological “ground truth” of the ocean bottom. The technical challenge here is to perfect acoustic survey techniques for bottom properties, which, despite much work over decades, are still being refined and improved. Of equally strong interest to marine sedi-

ment acousticians is the opportunity to measure the sediment sound speed dispersion (real and imaginary parts) over a broad frequency band.

The most intensively studied site was the central area at 80-m water depth. As mentioned, this site was first instrumented with a mid-frequency hydrophone array to measure acoustic reflectivity from the seabed at frequencies from 1–20 kHz. On a second visit to the site, we studied sound reflectivity and acoustic propagation at lower frequencies, from 4 kHz down to 50 Hz. The combined set of mid- and low-frequency data and accompanying measurements on geoacoustic properties will provide a unique opportunity to both compare techniques and study dispersion properties.

Another of the current research challenges in doing bottom geoacoustic property inversions, particularly at low frequencies where there are large path lengths between source and receiver, is to eliminate water column fluctuation effects from the inverse for the bottom. Use of inverse methods often requires

dealing with a large component of water-column fluctuation noise in the data. However, it is completely unrealistic to ask inverse methods to present an exact realization of the ocean between the source and receiver. Recently developed methods minimize the effects of water-column fluctuations on such inverses,

Two of the most active and promising technologies in oceanography are powered AUVs and AUV gliders.

based on knowing only the simple statistics of water-column fluctuations. As the SW06 experiment provides both high-quality measurements of ocean fluctuations and independent data on ocean-bottom structure and properties, this method can be tested with some rigor.

Many teams investigated the bottom-inversion issue using different techniques over a wide range of frequencies in this experiment. The combination of all the inversion results offers an opportunity, through a synthesis process, to obtain a consistent bottom model of the area that can be used to evaluate future sonar models.

AWACS

Two of the most active and promising technologies in oceanography are powered AUVs and AUV gliders. As part of SW06, a component of the AWACS (Acoustic Wide Aperture Coverage for Surveillance) project was conducted to utilize both powered and glider AUVs. The objectives were to: (1) conduct oceanographic surveys of an “interest-

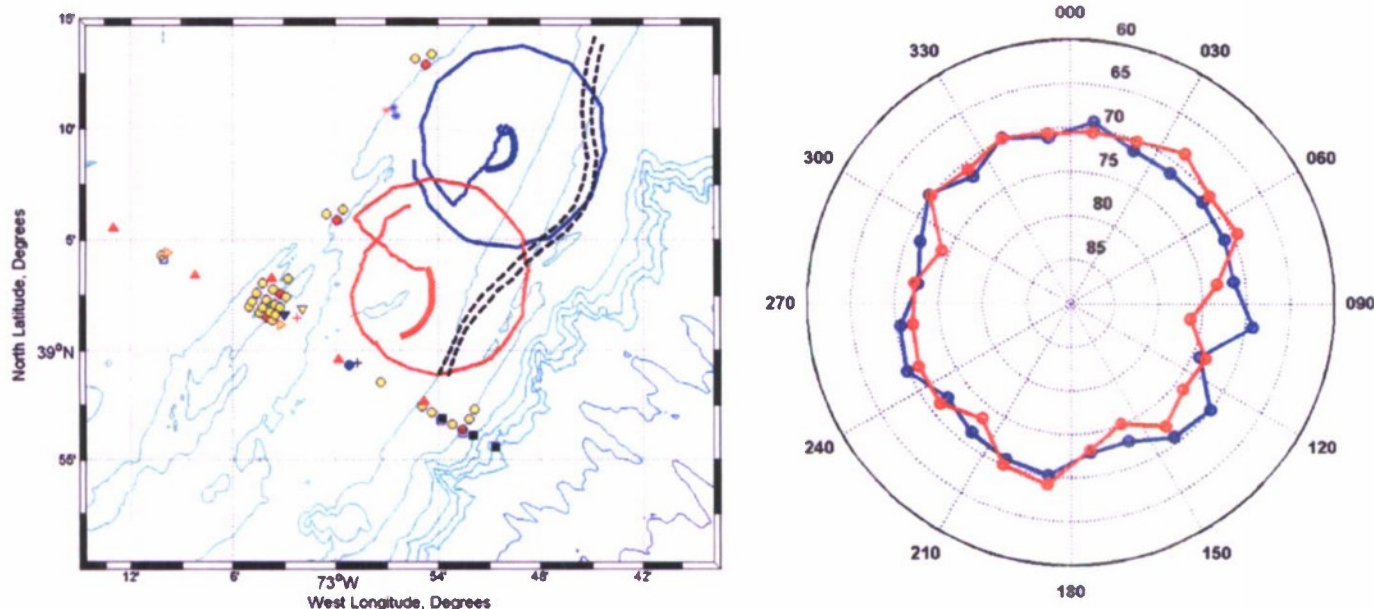


Figure 6. (a) The top panel shows tracks of Oasis mobile acoustic sources (large red and blue circles) emitting sounds to sonobuoy receivers (darker red and blue arc-segments within the circles) in the vicinity of the shelf-break front, in order to study the effects of frontal and shelf oceanography on sound propagation. (b) The bottom panel displays average acoustic propagation loss at 900 Hz and clearly shows: (1) near azimuthal isotropy over the shelf region, and (2) anisotropy (more loss) where the acoustic paths cross the shelf-break front, in the angular sector from (roughly) 90 to 180 degrees. Prediction of the position of the shelf-break front was one of the oceanographic challenges of AWACS.

ing area” of ocean (e.g., near the shelf-break front, or in a packet of solitons), (2) create an oceanographic map of that area based on the data, (3) pick a geometry most favorable for acoustic propagation/detection based on that oceanographic map, and (4) use moored and sonobuoy-based acoustic sources and receivers to demonstrate that the geometry so chosen was indeed an optimal one.

In pursuing this plan, small-boat operations were needed for deploying and recovering the small REMUS 100 AUVs and Webb gliders that were to be utilized. Unfortunately, the fringes of hurricanes Ernesto and Florence prohibited small-boat operations. (But fortunately for future programs, this inconvenient small-boat technique has since been superseded by fully “off the deck” operations!). Thus, we used Scanfish sur-

veys from the ship for oceanography and Oasis mobile acoustic sources and sonobuoy receivers for the acoustics. With this hurricane-induced “Plan B,” we were still able to perform the “adaptive acoustic sampling” part of the project. This succeeded well, with especially interesting results coming from trying to predict the shelf-break front and its acoustic effects, as illustrated in Figures 6a and 6b. In these figures, we show the anisotropy in acoustic propagation loss versus azimuth for propagation in the region of the shelf-break front. The anisotropy effects due to fronts and internal waves were of particular interest in SW06.

POSTSCRIPT

In the year that has passed since the SW06 experiment, great progress has been made in digesting the many tera-

bytes of data collected. We have made movies of acoustic arrivals at the arrays that graphically show their stability in oceanically calm periods and their gyrations during active periods. In addition, motion pictures of the nonlinear internal waves recorded by our “three-dimensional” mooring array are just coming into being. This graphic imagery, and much more analysis (some not quite so flashy), are providing the grist for a number of scientific publications. We have already lined up special sessions in a number of technical society meetings and a special issue in the *Journal of the Acoustical Society of America*. We hope that this “prelude” in *Oceanography* will stimulate readers’ interest in the further publications that will be coming out shortly from this very successful experiment.

ACKNOWLEDGEMENTS

First, we would like to thank our ONR sponsors, particularly Drs. Ellen Livingston, Theresa Paluszkiwicz, and Tom Curtin for their support of the SW06 experiment, and their help in coordinating its efforts. Next, we would like to thank the many co-PIs whose names do not appear on this paper (only direct contributors appear), but whose efforts and research in SW06 are the topic of this paper. Third, we would like to thank the numerous technicians, engineers, programmers, office personnel, students, and others whose efforts underpinned this large effort. Finally, the captains and crews of the research ships that participated in SW06 get our heartiest praise and thanks. Overall, SW06 was executed by a very talented, hardworking, and collegial group, and they made both the experience, and the results, fantastic. We all look forward to the next few years of continued work together on this vast, rich data set. ■

REFERENCES

- Apel, J.R., L.A. Ostrovsky, Y.A. Stepanyants, and J.F. Lynch. 2006. Internal solitons in the ocean. WHOI Technical Report WHOI-2006-04.
- Colosi, J.A., R.C. Beardsley, G. Gawarkiewicz, J.F. Lynch, C.S. Chiu, and A. Scotti. 2001. Observations of nonlinear internal waves on the outer New England continental shelf during the summer shelfbreak PRIMER study. *Journal of Geophysical Research* 106(C5):9,587–9,601.
- Davies, T.A., J.A. Austin Jr., M.B. Lagoe, and J.D. Milliman. 1992. Late Quaternary sedimentation off New Jersey: New results using 3-D seismic profiles and cores. *Marine Geology* 108:323–343.
- Duncan, C.S., J.A. Goff, and J.A. Austin Jr. 2000. Tracking the last sea-level cycle: Seafloor morphology and shallow stratigraphy of the latest Quaternary New Jersey middle continental shelf. *Marine Geology* 170:395–421.
- Fulthorpe, C.S., and J.A. Austin Jr. 2004. Shallowly buried, enigmatic seismic stratigraphy on the New Jersey outer shelf: Evidence for latest Pleistocene catastrophic erosion? *Geology* 32:1,013–1,016.
- Goff, J.A., J.A. Austin Jr., S. Gulick, S. Nordfjord, B. Christensen, C. Sommerfield, H. Olson, and C. Alexander. 2005. Recent and modern marine erosion on the New Jersey outer shelf. *Marine Geology* 216:275–296.
- Goff, J.A., B. Kraft, L.A. Mayer, S.G. Schock, C. K. Sommerfield, H.C. Olson, S.P.S. Gulick, and S. Nordfjord. 2004. Seabed characterization on the New Jersey middle and outer shelf: Correlability and spatial variability of seafloor sediment properties. *Marine Geology* 209:147–172.
- Goff, J.A., D.J.P. Swift, C.S. Duncan, L.A. Mayer, and J. Hughes-Clarke. 1999. High-resolution swath sonar investigation of sand ridge, dune and ribbon morphology in the offshore environment of the New Jersey margin. *Marine Geology* 161:307–337.
- Gulick, S.P.S., J.A. Goff, J.A. Austin Jr., C.R. Alexander Jr., S. Nordfjord, and C.S. Fulthorpe. 2005. Basal inflection-controlled shelf-edge wedges off New Jersey track sea-level fall. *Geology* 33:429–432.
- Jackson, C.R., and J.R. Apel. 2004. An atlas of internal solitary-like waves and their properties. Global Ocean Associates. 2nd ed. Available online at: <http://www.internalwaveatlas.com>.
- Makris, N.C., P. Ratilal, D.T. Symonds, S. Jagannathan, S. Lee, and R.W. Nero. 2006. Fish population and behavior revealed by instantaneous continental shelf-scale imaging. *Science* 311:660–663.
- Milliman, J.D., Z. Jiezo, L. Anchun, and J.I. Ewing. 1990. Late Quaternary sedimentation on the outer and middle New Jersey continental shelf: Result of two local deglaciations? *Journal of Geology* 98:966–976.
- Moum, J.N., J.M. Klymak, J.D. Nash, A. Perlin, and W.D. Smyth. 2007. Energy transport by nonlinear internal waves. *Journal of Physical Oceanography*.
- Moum, J.N., and J.D. Nash. In press. Seafloor pressure measurements of nonlinear internal waves. *Journal of Physical Oceanography* 37:1,968–1,988.
- Nordfjord, S., J.A. Goff, J.A. Austin Jr., and S.P.S. Gulick. 2006. Seismic facies of incised valley-fills, New Jersey continental shelf: Implications for erosion and preservation processes acting during late Pleistocene/Holocene transgression. *Journal of Sedimentary Research* 76:1,284–1,303.
- Nordfjord, S., J.A. Goff, J.A. Austin Jr., and C.K. Sommerfield. 2005. Seismic geomorphology of buried channel systems on New Jersey shelf: Assessing past environmental conditions. *Marine Geology* 214:339–364.
- Ramp, S.R., T.Y. Tang, T.F. Duda, J.F. Lynch, A.K. Liu, C-S. Chiu, F.L. Bahr, H.-R. Kim, and Y.-J. Yang. 2004. Internal solitons in the northeastern South China Sea, Part I: Sources and deep water propagation. *IEEE Journal of Ocean Engineering* 28(4):1,157–1,181.

Acoustic Ducting, Reflection, Refraction, and Dispersion by Curved Nonlinear Internal Waves in Shallow Water

James F. Lynch, *Fellow, IEEE*, Ying-Tsong Lin, *Member, IEEE*, Timothy F. Duda, *Senior Member, IEEE*, and Arthur E. Newhall, *Member, IEEE*

Abstract—Nonlinear internal waves in shallow water have been shown to be effective ducts of acoustic energy, through theory, numerical modeling, and experiment. To date, most work on such ducting has concentrated on rectilinear internal wave ducts or those with very slight curvature. In this paper, we examine the acoustic effects of significant curvature of these internal waves. (By significant curvature, we mean lateral deviation of the internal wave duct by more than half the spacing between internal waves over an acoustic path, giving a transition from ducting to antiducting.) We develop basic analytical models of these effects, employ fully 3-D numerical models of sound propagation and scattering, and examine simultaneous acoustical and oceanographic data from the 2006 Shallow Water Experiment (SW06). It will be seen that the effects of curvature should be evident in the mode amplitudes and arrival angles, and that observations are consistent with curvature, though with some possible ambiguity with other scattering mechanisms.

Index Terms—Horizontal acoustic ducting, horizontal acoustic refraction, reflection, and dispersion, horizontal acoustic shadowing, shallow-water acoustics, 3-D acoustics, curved nonlinear internal waves.

I. INTRODUCTION

NONLINEAR internal waves are common in the shallow waters of continental shelves and in adjacent seas, and have been shown to have strong effects on acoustic propagation and scattering. An early study in the Yellow Sea [1] showed a strong absorption of low-frequency (50–1000 Hz) sound due to scattering by internal wave packets, and this work was the impetus for many later studies. In the 1995 Shallow Water Acoustics in a Random Medium (SWARM) experiment [2], strong mode coupling occurring with across-internal-wave propagation geometry was emphasized, with the main acoustic tracks being directed across shelf. However, also as part of SWARM, Badiey *et al.* [3] performed transmissions in an along-shelf (and thus along the nonlinear internal

wavefronts) geometry. They observed a very strong ducting of low-frequency (roughly 50–500 Hz) sound between nonlinear internal waves. This effect had been predicted by computer modeling [4] and normal mode theory [5], but not previously observed. A strong and acoustically important ducting effect of order 6–10 dB was observed. The ducting and lateral mode scattering due to curved internal waves, previously examined for straight internal waves, will be the main topics of this paper.

In this paper, the acoustic effects of curved internal waves will be examined using theory, numerical modeling, and experimental data. Specifically, we will be looking at: ducting of sound through curved internal wave ducts, dispersive refraction of sound out of such curved ducts, and reflection and refraction of energy for sound sources external to such ducts. To do this, we will provide some basic analytic expressions which can readily show the physics, dependence on system parameters, and propagation effects. These expressions also allow “back of the envelope” estimates of acoustic field effects. With this foundation in place, results from more complicated calculations can be more systematically examined, namely, from fully three-dimensional (3-D) numerical simulation of propagation in and through curved internal waves. Finally, we will look at data from the 2006 Shallow Water Experiment (SW06) [6], which can shed some light on the topics we discuss here. SW06 was not specifically designed to address these issues and does not provide a definitive data set. However, features in the arrival angles and intensities consistent with the effects considered here appear in the data.

Our paper is organized as follows. Following this Introduction, we present in Section II our measurements of wavefront curvature from SW06, taking this to be a “not atypical” continental shelf environment for nonlinear internal waves. In Section III, we present some basic theory for how low-frequency acoustic ducting, reflection, refraction, and dispersion by curved nonlinear internal waves works, using the Weinberg–Burridge [7] formalism as a framework. In Section IV, we present computer modeling results, which give a visual and easy to comprehend depiction of the physical processes. In Section V, we present SW06 data showing just how large this effect is for one particular geometry, frequency, and set of internal wave field realizations using arrival angle fluctuations as the variable of interest. In Section VI, we present our conclusions and recommendations for future work.

Manuscript received May 14, 2009; revised December 01, 2009; accepted December 04, 2009. Current version published February 10, 2010. This work was supported by E. Livingston and T. Pawluskiewicz of the U.S. Office of Naval Research (ONR) under Grant N00014-04-1-0146 and the ONR postdoctoral fellowship award Grant N00014-08-1-0204.

Associate Editor: N. R. Chapman.

The authors are with the Applied Ocean Physics and Engineering Department, Woods Hole Oceanographic Institution, Woods Hole, MA 02543 USA (e-mail: anewhall@whoi.edu).

Color versions of one or more of the figures in this paper are available online at <http://ieeexplore.ieee.org>.

Digital Object Identifier 10.1109/JOE.2009.2038512

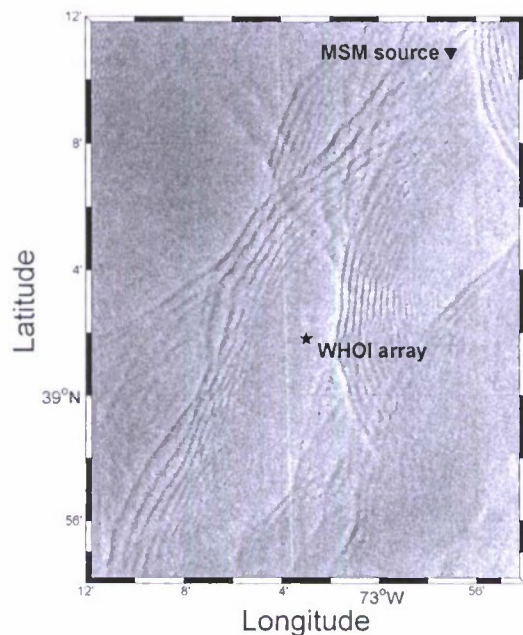


Fig. 1. SAR image of curved nonlinear internal waves in the SW06 experimental area. Range from the University of Miami acoustic source (MSM) to the Woods Hole Oceanographic Institution (WHOI) array is 19.7 km, and orientation is along shelf.

II. MEASUREMENTS OF INTERNAL WAVE CURVATURE

To date, most of the acoustic propagation studies of internal waves have used straight line internal wavefronts for individual waves or packets. (Notable exceptions are the works by Katznelson and Peresl'kov [5] and Duda *et al.* [8].) However, while nearly linear wavefronts have been observed and make sense due to generation at linear shelfbreaks, reasonably curved internal wavefronts are just as commonly observed. This is illustrated using satellite synthetic aperture radar (SAR) images. Fig. 1 shows typical curved wavefronts from a SAR image from SW06. A curved wavefront can arise from wave generation at a strong bathymetric "point feature" (compared to the internal tide wavelength of $\sim 10\text{--}40$ km) such as a submarine canyon like Hudson Canyon, or it can be produced by horizontally varying bathymetry or by flow features (current shear and/or buoyancy frequency variations) refracting an initially plane wave.

Curved wavefronts can be modeled as circular arcs, and that technique is used in this paper, which is focused on understanding the physical effects on acoustics of curved, nonlinear internal waves, rather than providing a detailed numerical/oceanographic model of such waves. We will take the local wavefront curvature to be consistent with field observations, both from SAR and *in situ* observations (see [9] for *in situ* data discussions).

When looking at the SAR images of nonlinear internal wave surface effects, one can employ image processing schemes of varying degrees of complexity. As an example, to identify and map the waves on the surface, Boughan and Siegmann [10] have used fingerprint recognition methodology with reasonable success. Gradient sensing (edge detection) algorithms also have some success in this mapping task (e.g., standard commercial

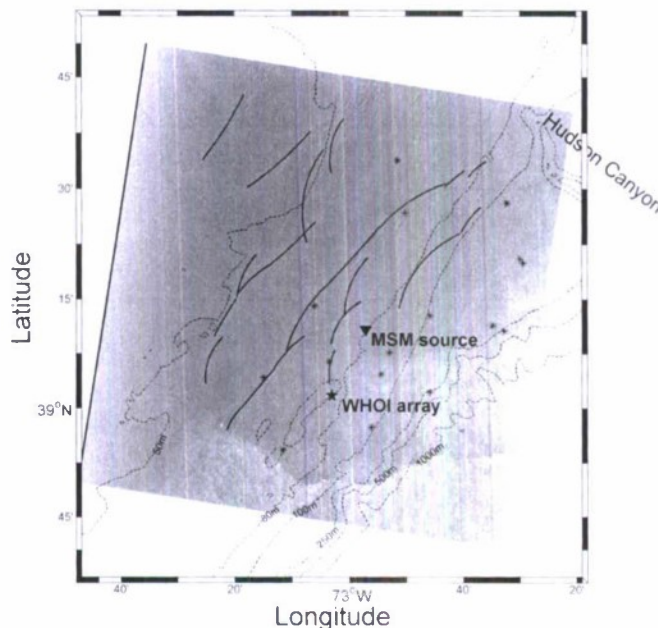


Fig. 2. Curved internal wave train significant wavefronts seen in SW06, from one SAR image (i.e., a "realization"). Fitted circular arcs are shown. Center points of the fitted circles are also shown (*).

signal processing software). However, the most sensitive and discriminating sensor to map these waves may be the trained human eye, which detects low signal-to-noise ratio (SNR) signals well and also recognizes patterns versus clutter better. This point can certainly be argued, but we will take the pragmatic view that for the small number of images that we have available to process (order 10), visual processing on image features is both robust and economical. This approach also can be argued to be subjective—to minimize this, we had several independent observers cross check the imaging results for consistency.

The results of fitting circular curves to prominent and/or significant internal waves in a typical SAR image from SW06 are shown in Fig. 2. In this figure, a number of arcs of various lengths and radii of curvature can be seen. Three things are of first-order interest to us in this picture: 1) the distribution of arc lengths, 2) the distribution of radii of curvature, and 3) the seemingly spatially random distribution of the circle centers. The distribution of radii of curvature, which is most important to this paper as input to the acoustics, shows the forms seen in Fig. 3(a) and (b). We see that these distributions of radii peak at $\sim 20\text{--}25$ km, which intriguingly is the along-shelf correlation scale for the density and current field, and may indicate some of the underlying mechanisms for the curvature (as will be discussed). We note that the distribution for the leading waves of packets [Fig. 3(b)] tends towards a somewhat larger radius of curvature than a more inclusive distribution [Fig. 3(a)], which may reflect the nonlinear "healing or conjoining" of intersecting and nonlinearly interacting waves, as well as the simple "distance from the source" effect. The distribution of arc lengths [Fig. 3(c)] is similarly peaked at $\sim 20\text{--}25$ km, which tells us how long the ducted acoustic track can be. The spatial distribution of where the centers of the arc lie should eventually tell us about the source distribution for the curvature. As mentioned before,

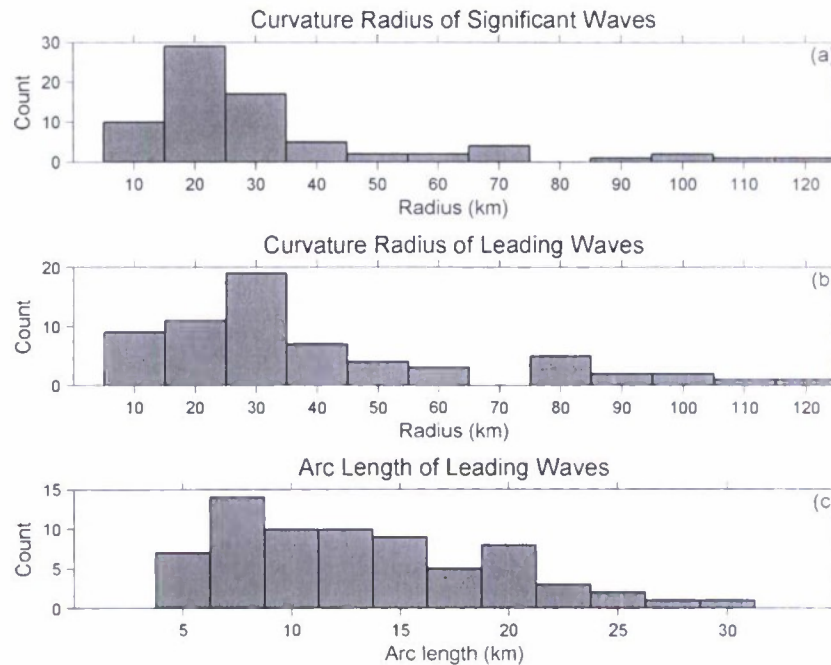


Fig. 3. (a) and (b) Distribution of radii of curvature from a SAR image, like the one shown in Fig. 2. (c) Arc lengths of the leading waves.

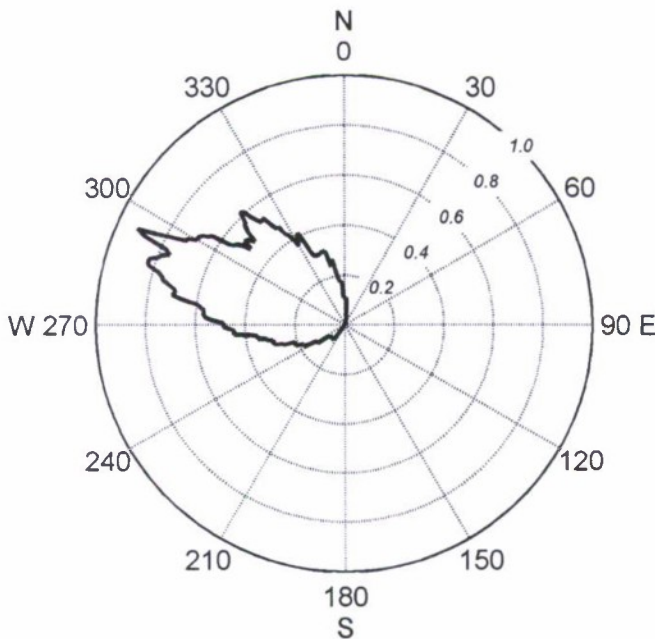


Fig. 4. Curved internal wavefront directionality from SAR images.

this can be due to several effects, and will be looked at in the near future.

Another quantity of interest is the directional spectrum of the nonlinear internal waves, shown in Fig. 4. This figure shows that the waves travel primarily in the 290° direction relative to true north, but also have a spread of about 30° to either side. This is due to both the curvature and the primary direction of the wave trains. This spread also indicates the probability of a unidirectional, along-shelf acoustic track encountering the internal waves at an angle, which can lead to mode coupling effects.

Although the radii of curvature, arc lengths, and somewhat scattered locations of the curvature centers given by the SAR images provide sufficient information for a theoretical acoustics study, there is also the aspect of predicting these numbers from physical oceanographic models. Currently, primitive-equation hydrostatic regional ocean models work routinely at space and time scales of a few kilometers x - y resolution and 12.4 h (M2 tide) time scales, but not at the 10-m and 30-s time scales needed for nonlinear internal waves with nonhydrostatic dynamics. Three-dimensional high-resolution nonhydrostatic models have been developed but are not in routine use for internal wave studies [11], [12]. A “nested internal wave model” superimposed on a mesoscale model is currently close to the state-of-the-art and feasible to do. However, if refraction by mesoscale eddies and generation of curved waves by irregular features (e.g., canyons) near the shelfbreak are the prime sources of the curved internal waves we see, then we can perhaps predict the curvature quantities presented above simply with mesoscale oceanography models, reasonable bathymetry maps, and relatively simple refraction/scattering physics. This approach is currently being pursued [13].

III. THEORETICAL STUDY

In this section, we wish to provide some analytic expressions which show the physics of the ducting, reflection, refraction, and dispersion of sound by curved nonlinear internal waves. Specifically, the derived expressions show the dependence on sonar system and environmental parameters, and predict intensity and arrival angle variations. We start from the Weinberg-Burridge “horizontal rays and vertical modes” picture which can accommodate 3-D adiabatic modes and even some coupled mode effects, when used properly.

A side view of the environment to be used with this model is shown in Fig. 5. Far away from the internal waves there is an

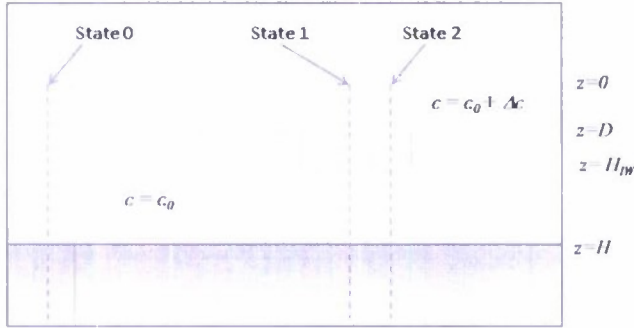


Fig. 5. Background state (state 0) and two perturbation states.

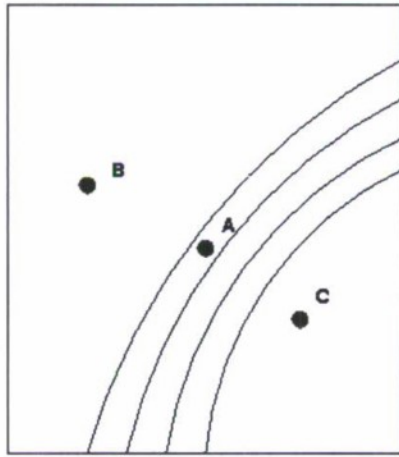


Fig. 6. Useful acoustic source geometries to consider relative to a curved internal wave train.

isosped background state with sound speed c_0 , depth H , and with modal wave numbers k_{0n} . Between two internal waves is perturbation state 1, where a near-surface upper layer of height D having higher sound speed exists, with upper layer speed $c_0 + \Delta c$. In this region, the mode wave numbers are denoted k_{1n} . Inside the internal wave is found perturbation state 2, where the upper layer of elevated sound speed extends to depth H_{IW} and mode wave numbers are denoted k_{2n} . Note that a duct forms between internal waves (state 1 bounded by state 2 on either side).

Fig. 6 is a plan view of possible source positions relative to a curved (circular) internal wave train. There are three distinct geometries to consider: A) a source within the internal wave train, B) a source on the exterior of the circular wavefronts, and C) a source interior to the internal wavefronts. We consider each of these cases.

A. Critical Angle Estimation

In this section, an expression for the critical angle within an internal wave duct will be derived in terms of the internal wave parameters. Local eigenvalues can be computed numerically and used to study ducting directly, but the goal here is to show how the internal-wave parameters govern the ducting process. Perturbation theory will be used to derive an expression governing the total internal reflection within internal wave ducts. Internal wave ducts will be approximated as square waves, for

theoretical convenience. However, this simplification still represents the ducting effects of the waves well.

The chosen Weinberg–Burridge (or “ray mode” for shorthand) approach is initiated by calculating the local vertical mode eigenvalues for the 3-D volume to be considered on a well sampled x - y grid, producing $k_n(x, y, \omega)$ for a given source angular frequency ω . One then interpolates the eigenvalues on this x - y grid for each mode (at the given ω). Doing this, one creates a horizontal index of refraction field that will determine the horizontal trajectories for each vertical mode n , using the simple relation $n_n(x, y, \omega) = k_n(\vec{r})/k_n(0)$. Here we choose the reference point (origin) to be the point $\vec{r} = (x, y)$ with the smallest eigenvalue magnitude, so that $n_n \geq 1$.

Snell’s law, written in terms of grazing angle with respect to the horizontal boundary of an internal wave duct, is $k_{1n} \cos \theta_1 = k_{2n} \cos \theta_2$ for vertical mode number n . Disregarding tunneling effects [14], the critical angle for trapping a mode within an internal wave duct is given by

$$\theta_{1n}^{\text{crit}} = \cos^{-1} \left(\frac{k_{2n}}{k_{1n}} \right). \quad (1)$$

To complete the task of expressing the critical angle in terms of the parameters of depth, internal wave height, and so on, we use perturbation theory. Since we are mainly interested in modeling oceanographic effects due to internal waves, we can take the bottom to be a rigid ($\rho \rightarrow \infty$) boundary for simplicity. (That is not to say that the bottom properties do not affect this problem—they do [15], [16]. However, we will ignore that added complication here.)

Away from the internal waves, the rigid bottom model background-state eigenvalues are found via

$$\gamma_{0n} H = \left(n - \frac{1}{2} \right) \pi \quad (2a)$$

and

$$k_{0n} = \sqrt{k^2 - \gamma_{0n}^2} \quad (2b)$$

where γ_{0n} is the vertical mode eigenvalue/wave number and $k = \omega/c_0$. The vertical mode functions for this model are sinusoids, i.e.,

$$Z_{0n}(z) = \left[\frac{2}{H} \right]^{1/2} \sin(\gamma_{0n} z). \quad (2c)$$

It is the difference between these sinusoids and the mode functions for a more realistic stratified ocean and seabed that actually represent the biggest limitation for our model. In a more realistic ocean, the low modes are pushed down from the mixed layer and the internal waves more than this background model permits. However, this affects the excitation of the modes far more than their horizontal trapping, so it is not a major concern in our treatment here.

To treat the mixed layer (state 1) and internal wave (state 2) situations, we use the well-known perturbation forms [17] to find the mode wave numbers

$$k_{1n} = k_{0n} + \Delta k_{1n}, \quad k_{2n} = k_{0n} + \Delta k_{2n} \quad (3)$$

namely, for state 1

$$\Delta k_{1n} = \frac{1}{k_{0n}} \int_0^H \frac{\Delta q Z_{0n}^2(z) dz}{\rho(z)} \quad (4a)$$

$$\Delta q = -\Delta c(z) \frac{\omega^2}{c_0^3(z)} \quad (4b)$$

where ω is angular frequency. In (4a) and (4b), $c_0(z)$ is the background sound-speed profile (which is isospeed in this case). State 2 produces similar expressions.

Inserting the mode shapes into (4a) and noting that the integration range can be changed because Δc is zero in the lower layer, one can write

$$\Delta k_{1n} = \frac{-2}{k_{0n}H} \frac{\omega^2}{c_0^2} \frac{\Delta c}{c_0} \int_0^D \sin^2(\gamma_{0n}z) dz. \quad (5)$$

The sine squared integral is an elementary one, giving (denoting the integral by I)

$$\begin{aligned} I &= \left[\frac{z}{2} - \frac{1}{4\gamma_{0n}} \sin(2\gamma_{0n}z) \right]_{z=0}^{z=D} \\ &= \frac{D}{2} \left(1 - \text{sinc} \left(\frac{2\gamma_{0n}D}{\pi} \right) \right) \end{aligned} \quad (6)$$

where the sinc function is defined as $\text{sinc}(X) = \sin(\pi X)/\pi X$. In the high-mode limit, as γ_{0n} increases and so does the argument of the sinc function, the second term becomes small with respect to the first, giving the form

$$I \approx \frac{D}{2}. \quad (7)$$

As an example of where the high-mode number approximation is valid, when the value of the sinc function in (6) is less than ~ 0.2 , we can neglect its contribution to the integral I . This criterion can be shown to be equivalent to $5n > H/D$, where n is the mode number. In this level of approximation, the eigenvalue perturbations are

$$\Delta k_{1n} = \frac{-1}{k_{0n}} \frac{\omega^2}{c_0^2} \frac{\Delta c}{c_0} \frac{D}{H}. \quad (8)$$

A procedure identical to that used to derive (8) can be used to find the eigenvalue perturbations for state 2, in the internal wave of depression

$$\Delta k_{2n} = \frac{-1}{k_{0n}} \frac{\omega^2}{c_0^2} \frac{\Delta c}{c_0} \frac{H_{IW}}{H}. \quad (9)$$

Note that although the exact form of the integral I is generally a better approximation to use, the high-mode number approximation shows very clearly the mode number, frequency, layer thickness, and sound-speed perturbation contribution to the wave number perturbation and thus the internal wave induced index of refraction change in the adiabatic mode model.

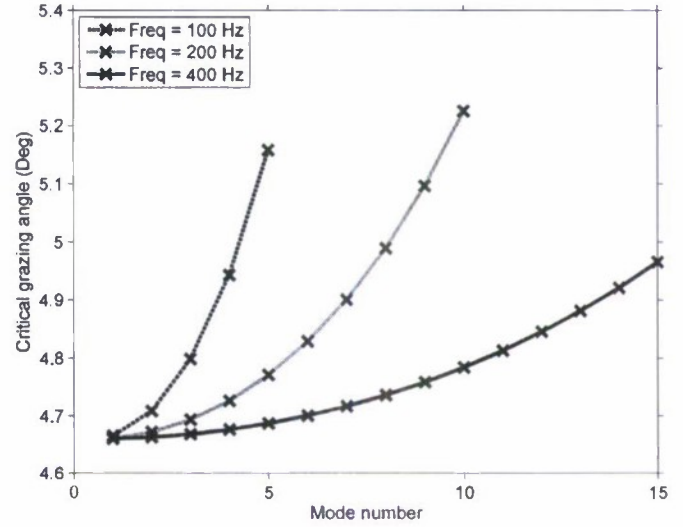


Fig. 7. Critical grazing angle versus mode number and frequency for an idealized internal wave based on the real SW06 internal waves.

Combining (1), (2a), (3), (8), and (9) yields for critical grazing angles

$$\theta_{1n}^{\text{crit}} = \cos^{-1} \left[\frac{\left[k^2 - \left[\frac{\left(n - \frac{1}{2} \right) \pi}{H} \right]^2 \right]^{1/2} - \frac{H_{IW} \Delta c \omega^2}{k_{0n} c_0^3 H}}{\left[k^2 - \left[\frac{\left(n - \frac{1}{2} \right) \pi}{H} \right]^2 \right]^{1/2} - \frac{D \Delta c \omega^2}{k_{0n} c_0^3 H}} \right]. \quad (10)$$

The above formula shows the limit of no trapping by internal waves (critical grazing angle of 0°), when $H_{IW} = D$. When these two dimensions differ, modes having supercritical incidence angle will be trapped. Modes with subcritical incidence angle will dispersively refract as they exit the duct.

The equation for $\theta_{1n}^{\text{crit}}$ can be evaluated for waveguide parameters based on SW06 data. We take $D = 15$ m, $H_{IW} = 25$ m, $H = 80$ m, $c_0 = 1520$ m/s, $\Delta c = 40$ m/s, $f = 100, 200$, and 400 Hz, which results in the critical angle curves seen in Fig. 7. In this figure, a number of interesting features can be observed. First, one sees that the critical angles range from about 4.65° to 5.2° , with mode 1 for all frequencies being at the minimum of 4.65° . Second, we see that the curves are all parabolae, in accordance with (10). Third, we see that as frequency increases, the curves flatten, and will reach a high-frequency asymptote of 4.65° , which is the ray theory limit. Calculations using real SW06 internal wave and waveguide environmental parameters give critical angles close to those seen in Fig. 7, except for some minor differences due to the penetrable bottom.

B. A Source Within the Internal Wave Train

Having created a useful, horizontal index of refraction field $n_n(\vec{r})$ for each mode, we can now turn our attention to the hori-

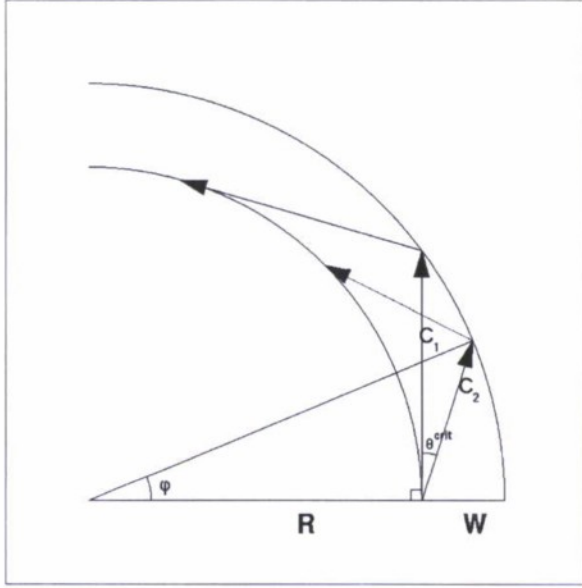


Fig. 8. Geometry of a low-speed duct between two internal waves. Limiting chords for modal-ray propagation are shown.

zonal propagation and scattering effects that are the main focus of the paper.

The point of this section is to determine limitations on curved wave duct width (W) and radius of curvature (R) which must be satisfied for two types of ducting. One type is full ducting, where horizontal modes of the duct interact strongly with both internal wave “walls,” and the other is equivalent to repeated reflection on the exterior (concave) wall. These would be called potential well and whispering gallery effects in physics parlance.

Total internal reflection and leakage of modes in a curved waveguide have been studied extensively in terms of optics (light pipes) and microwave ducts, among other fields [18]. Our treatment here will obviously bear some similarities to these analogous physical systems, as well as some differences due to the specific nature of the ocean acoustic waveguide. To understand the basic physics of a sound source within an internal wave train, consider a single duct, which might be formed by, e.g., the leading edge or strongest wave of an internal wave train and its nearest neighbor. A source in a canonical horizontal duct of this type, where the square-well internal wave approximation is used, is shown in Fig. 8. This figure defines a few parameters that are needed for the analysis. C_1 is the length of a line segment (ray) that is tangent to the inner wall and reflects off the outer wall. C_2 is the length of a ray that reflects off the outer wall at a critical angle while being emitted at the inner wall at the same angle θ . Δ_{nm} is the arc length of the mode-cycle distance for horizontal ducted mode m of vertical mode n . φ is the radian arc length associated with $\Delta_{nm}/2$.

Since internal wave trains have across train extent ~ 100 – 400 m for both the depression-type internal waves and the low-sound-speed (acoustic duct) regions between them, which is many acoustic wavelengths for frequencies above about 50 Hz, it is reasonable to use the square-well approximation. In this approximation, one assumes infinite width of the bounding

internal waves. This is allowable if tunneling is small. This method also treats refractive transmission correctly. Internal waves are also slowly varying in sound speed over their dimensions (except at boundaries, which we treat explicitly by transmission/reflection coefficients), so that our square-well model and horizontal ray theory are also consistent.

The first effect of note due to the curvature of the waveguide is on the angle of reflection off the boundaries of the waveguide. For an infinitely thin waveguide, $W \rightarrow 0$ and there is no local curvature effect, as can be seen examining Fig. 8. However, for finite W , the waveguide exhibits a curve over a horizontal ray/mode cycle distance Δ_{nm} , where n is the vertical mode index, and m is the horizontal mode index. Note that the horizontal mode cycle distance is defined by the interference of two adjacent horizontal modes (m and $m + 1$). The arc length (in radians) over half a cycle distance (the distance from hitting one wall and going to the opposite one) can be estimated with midpoint and small-curvature approximations, and is found to be

$$\varphi_{nm} = \tan^{-1} \left(\frac{\frac{\Delta_{nm}}{2}}{R + \frac{W}{2}} \right). \quad (11)$$

Δ_{nm} can be computed from knowledge of the (straight waveguide) horizontal modes via $\Delta_{nm} = 2W / \tan \theta_{nm}^{\text{hor}}$, which relates Δ_{nm} directly to the horizontal mode angle θ_{nm}^{hor} . This mode angle can be computed for our model using an eigenvalue equation directly analogous to the Pekeris waveguide equation. However, we can replace the Δ_{nm} calculation by its bounding limits by considering chords at C_1 and C_2 . These represent the cycle distance limits for the horizontal modes formed from the sound energy bouncing between the internal wave walls (“bouncing” modes). Note that there should also be horizontal modes of a true “whispering gallery” type (i.e., only reflecting off the exterior wall), as will be discussed. The results of using these limits are shown in

$$C_1 = \sqrt{(R+W)^2 - R^2} \quad (12a)$$

$$C_2 = \frac{W+R}{\sin \left(\frac{\pi}{2} + \theta_n^{\text{crit}} \right)} \times \sin \left(\pi - \left(\frac{\pi}{2} + \theta_n^{\text{crit}} \right) - \sin^{-1} \left(\frac{R \sin \left(\frac{\pi}{2} + \theta_n^{\text{crit}} \right)}{W+R} \right) \right) \\ = \frac{W+R}{\cos \theta_n^{\text{crit}}} \cos \left(\theta_n^{\text{crit}} + \sin^{-1} \left(\frac{R}{W+R} \cos \theta_n^{\text{crit}} \right) \right) \quad (12b)$$

and $C_2 \leq \Delta_{nm}/2 \leq C_1$, where θ_n^{crit} can be calculated from Snell’s law, as discussed previously, and shown explicitly in (10). Substituting (12a) in (11) gives the limits for φ

$$\tan^{-1} \left[\frac{C_2}{R + \frac{W}{2}} \right] \leq \varphi \leq \tan^{-1} \left[\frac{C_1}{R + \frac{W}{2}} \right] \quad (13)$$

which is an explicit formulation for the limits of the angle of internal wave curvature over half a cycle distance of the bouncing horizontal modes. The detailed sound-speed profile and internal

wave structures play a role in these limits because C_2 is a function of the critical angle. Also, it can be shown that for higher vertical modes the lower bound is smaller, which implies a better ducting condition.

Let us further discuss the transition of the ducting physics from straight internal waves to curved internal waves. First, we note that in some cases (the bouncing mode cases), averaged over a cycle distance, the modal energy will hit the interior wall of the curved duct at a lower angle $\theta_{nm}^{\text{hor}} - \varphi/2$ than the exterior wall, which is at $\theta_{nm}^{\text{hor}} + \varphi/2$, where θ_{nm}^{hor} is the horizontal mode angle obtained from a straight duct. This is a “falling away horizon” (interior wall) versus an “approaching horizon” (exterior wall) curvature effect. Thus, losses should occur preferentially at the exterior side of the curved duct. Moreover, all of the bouncing modes should have incoming grazing angles of $\theta_{nm}^{\text{crit}} - \varphi/2$ or below at the exterior side of the curved duct. Sound that is subcritical and reflects at the interior wall of the duct may be supercritical on the outer wall of the wave duct because of this restriction. Some energy will escape via dispersive transmission, with the angle of escape depending on the mode numbers (n and m) and the frequency ω . This effect will be demonstrated later with a computational result. Also note that the forms described above can also be used to identify the energy carrying horizontal rays that such a 3-D parabolic acoustic wave equation (PE) produces.

In the whispering gallery mode situation, the modal energy will hit the exterior wall at $\theta_{nm}^{\text{hor}} + \varphi/2$ on average over a cycle distance. From Fig. 8, it is clear that if this angle is smaller than the tangent angle $\cos^{-1}(R/(R+W))$, at which the reflected sound from the outer wall will just graze the inner wall, one can see a horizontal mode/ray reflecting only from the outer boundary, which leads to the classic whispering gallery effect and its modes.

C. A Source Exterior to Curved Internal Wave Train

Whereas the case of a source within a curved internal wave duct can produce some interesting light pipe and chromatic dispersion effects [18], a source exterior to a curved internal wave train can see some equally interesting horizontal shadow zone and caustic effects. The shadow zone arises because the circular internal wavefront is not transparent to sound below critical grazing angle. The caustic is associated with the edge of the shadow zone.

To examine this case, consider the geometry depicted in Fig. 9. Here, R is the radius of the circular internal wave train, R_S is the distance from the source to a given point on the internal wavefront, and R_{CPA} is the closest point of approach (closest distance) from the source to the circular internal wave train. In terms of angles, θ_0 is the horizontal launch angle of the sound relative to the axis between the original circle and the source, φ is the angle between the radius to the point on the curve of interest and the source/circle origin axis, and θ_{graz} is the grazing angle of the sound with the internal wave train surface, the quantity of prime interest here. Application of the law of sines gives us

$$\frac{R}{\sin \theta_0} = \frac{R + R_{\text{CPA}}}{\sin \left(\frac{\pi}{2} + \theta_{\text{graz}} \right)} = \frac{R_S}{\sin \varphi}. \quad (14)$$

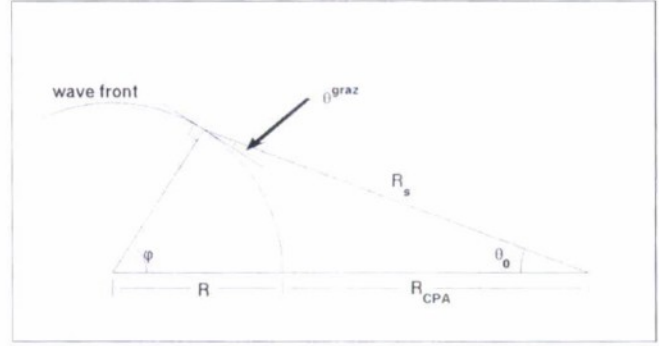


Fig. 9. Example of how “falling away horizon” gives critical angle before the tangent point, and thus a shadow region behind the internal wave.

This can be solved to give

$$\theta_{\text{graz}} = \cos^{-1} \left[\frac{R + R_{\text{CPA}}}{R} \sin \theta_0 \right]. \quad (15)$$

Past critical grazing angle out to the angles where the ray hits the tangent of the circle, there is an acoustic shadow. The latter (tangent) angle is given by

$$\theta_{\text{tangent}} = \cos^{-1} \left(\frac{R}{R + R_{\text{CPA}}} \right). \quad (16)$$

There will be a shadow beyond the internal wave along extensions of the rays that strike the wave duct such that $0 < \theta_{\text{graz}} < \theta_{\text{crit}}$. The interest here is not just that there is critical angle shadowing, which we would get with a straight line internal wavefront as well, but since the “horizon is falling away” due to the internal wavefront curvature, one sees a shadow at a much lower θ_0 than one would for the straight line front case. This also reduces the distance that is required between the source and the internal wave for shadowing to occur, which means less energy lost in transit, making shadowing more important. Again, we note that θ_{crit} can easily be determined given the forms we have derived above.

D. A Source Interior to Curved Internal Wave Train

Looking at Fig. 10, we see that the law of sines and standard triangle identities can be used exactly as in Section VI, so as to give

$$\frac{R}{\sin(\pi - \theta_0)} = \frac{R_S}{\sin \varphi} = \frac{R - R_{\text{CPA}}}{\sin \left(\frac{\pi}{2} - \theta_{\text{graz}} \right)}. \quad (17)$$

Thus, we obtain

$$\theta_{\text{graz}} = \cos^{-1} \left[\frac{R - R_{\text{CPA}}}{R} \sin \theta_0 \right]. \quad (18)$$

Equation (18) is the same as (15), only with a sign change for R_{CPA} (which is now negative, as it is inside the circle).

In this case, there is a concave horizon (approaching) and it is difficult to attain critical grazing angle (impossible when $\theta_{\text{graz}} \geq \theta_{\text{crit}}$). Thus, sources inside the internal wave are less likely to see any critical angle shadowing effects.

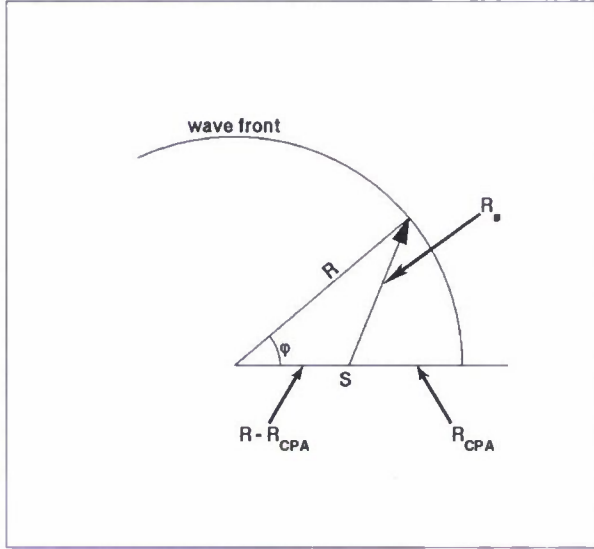


Fig. 10. Source interior to internal wave train.

E. Energetics

From our theoretical analysis, we can conclude that modes can both duct and be bent appreciably in the horizontal. But what do we expect to see in real data? To partially answer that question, we will look briefly at the energetics of the ducted and leaked beams using a sonar equation/geometric approach first used by Lynch *et al.* [19] in the context of ducting within straight internal waves. In the straight-duct picture, one finds that for $\theta < \theta^{\text{crit}}$ (θ is the horizontal grazing angle), ducting occurs and there is no cylindrical spreading, i.e., the $r^{-1/2}$ cylindrical spreading term vanishes, and so one sees a ratio R between the trapped (ducted) and horizontally untrapped (cylindrically spreading) pressures

$$R_{\text{press}} \cong \sqrt{\frac{2r\theta^{\text{crit}}}{W}} \quad (19)$$

where r is the source-to-receiver range and W is the width of the duct. This sonar equation/geometric factor reasonably predicted what was seen in the 1995 SWARM experiment data [2]. We now extend this form to look at the ratio of the higher mode ducted energy to the lower mode unducted (beam-leaked) energy. If we look at our 100-Hz example in Section III-A, this is the ratio of vertical mode 1 to mode 2. Note that in Section III-A a rigid bottom was used, while a penetrable bottom with sound speed 1700 m/s and density 1.8 g/cm³ is used here. If we write down expressions for the pressure of these modes, we have

$$p_1(r) = \frac{1}{\sqrt{k_1 r}} p_{0,1} e^{-\beta_1 r} \quad (20)$$

and

$$p_2(r) = \sqrt{\frac{2\theta_2^{\text{crit}}}{k_2 W}} p_{0,2} e^{-\beta_2 r} \quad (21)$$

where β_1 and β_2 are the modal attenuation coefficients.

Taking the ratio of these two expressions, with $p_{0,1} \approx p_{0,2}$ and $k_1 \approx k_2$ (just to make interpretation easier), we obtain

$$R_{2/1} = \sqrt{\frac{2r\theta_2^{\text{crit}}}{W}} e^{-(\beta_2 - \beta_1)r}. \quad (22)$$

We see that the mode 2 ducting “gain” of the \sqrt{r} should be counteracted by the exponential decrease in mode 2 by exponential attenuation. Thus, at “sufficiently far range,” the curved ducting effect could be lost, and only the initial beaming and refraction of the low modes by the curved duct would be observed. In terms of angular deflection of the energy, the energy that is ducted by the curved duct over large distances, and thus would show a large angle deflection, would likely be lost due to attenuation. Let us put in some numbers for this. Using a normal mode code to calculate β_n , we see that for 100 Hz and the parameters used above, $\beta_2 = 4.38 \times 10^{-5} \sim 3\beta_1$, and for 200 Hz, $\beta_3 = 3.93 \times 10^{-5} \sim 2\beta_2$. If we take $W = 250$ m and use $\theta^{\text{crit}} \sim 4.7^\circ$ for all modes, we obtain that $R_{2/1} = 0.7$ (the 6-dB down point) is at 780 m for 100 Hz and $R_{3/2} = 0.7$ is at 770 m for 200 Hz. These are rather modest distances. Moreover, these estimates do not account for the fact that a curved path from the source to a receiver is always longer than a straight line (geodesic) path, which can make the curved path up to a factor of $\pi/2$ longer for a semicircle. However, on the other hand, it also does not account for the detailed interferences within the duct, which can produce focusing regions of high intensity at ranges greater than one would predict from the preceding sonar equation (average field) type of argument. This discussion points out that the curved ducted path can still be energetically significant compared to a straight line path over a few kilometers, but probably not much more for the size and strength of internal waves seen in SW06. However, stronger ΔC internal waves and larger amplitude internal waves (which are often seen elsewhere in the world’s oceans), could easily make the distances over which curved paths have appreciable ducted energy larger.

We might also look more closely at the energetics of the leaking beams. These modal beams are ducted initially, over about a mode cycle distance, after which they leak out. Thus, they do not spread like the ducted modes up to about Δ_{nm} , and then they spread cylindrically. Thus, past Δ_{nm} , we have

$$p_1 \sim p_{01} \sqrt{\frac{1}{p_1(r - \Delta_{nm})}} e^{-k_1 r} \quad (23)$$

which slightly modifies our previous ratio results. We note that the refraction of the beam upon escape from the duct can also tighten (focus) the escaping beam slightly, but this is expected to be a very small effect.

As a final note in this section, before we proceed to the numerical modeling and data results, we discuss what a “more realistic” curved duct model would entail, again with the acoustics in the context of the Weinberg–Burridge formalism. To begin with, one could use a realistic $c(x, y, z)$ field, based on data, numerical models, or a combination of both. From this, one can create a more detailed $n_n(\vec{r})$ field, using the exact model eigenvalues, as opposed to our perturbation results. From this, one could find slightly more detailed horizontal model ray trajectories, which certainly have some physical insight, but on a

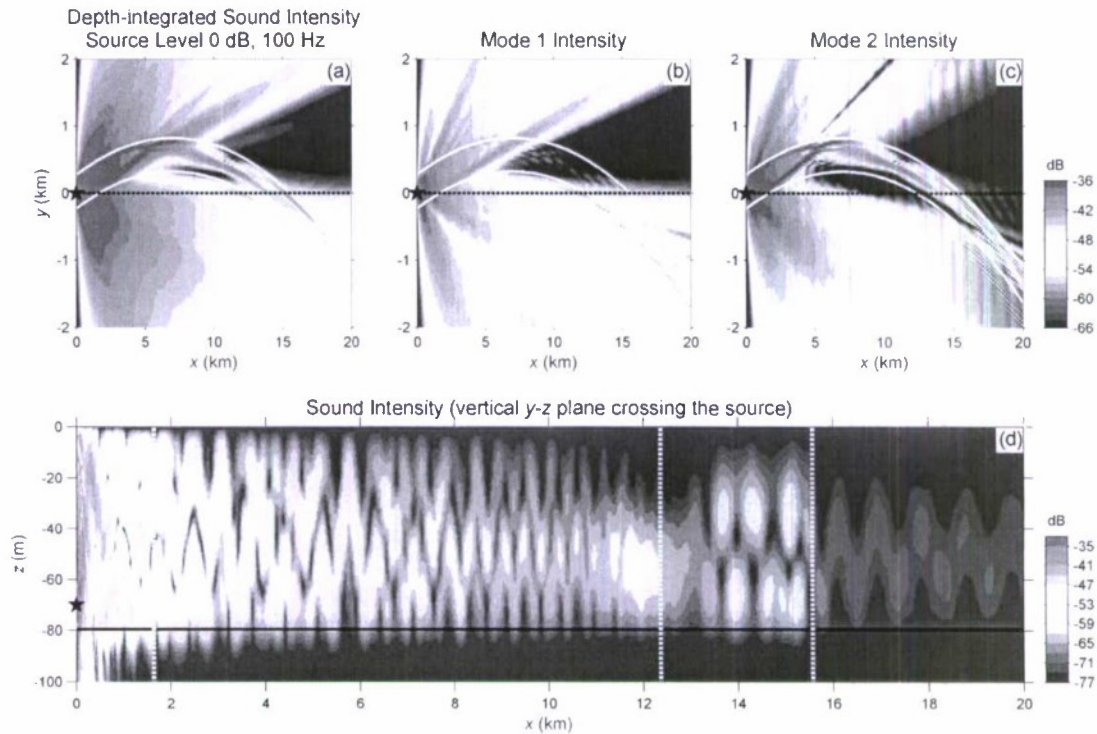


Fig. 11. (a) Depth-integrated sound intensity at 100 Hz. (b) Vertical mode 1 intensity. (c) Vertical mode 2 intensity. (d) Vertical slice of sound intensity at $y = 0$ (all dB units are unity source level). Note clear appearance of mode 1 and 2 between ranges 12 and 15 km (in the internal wave duct). Radius of curvature is 45 km here.

more visual basis. However, the tradeoff for this greater computational fidelity and accuracy is a loss of transparency of the physics, at least in the analytical form sense. With these comments in mind, it is now appropriate to look at the more detailed numerical model.

We also note that the trajectory of mode coupled beams escaping the waveguide can also be described by the ray-mode calculations, simply by having mode $nm \rightarrow nm'$ at the coupling interface and then using the modal index of refraction for nm' after coupling. Given close coupling, these coupled mode trajectories will cluster in a beam around the adiabatic angle for nm . We also note that use of Snell's law using the local modal index of refraction describes the paths incident on and refracting through the internal wave duct boundaries.

IV. NUMERICAL MODELING

In this paper, to handle a realistic ocean case, we employed a Cartesian 3-D parabolic equation acoustical propagation program [20], which is briefly described below, and the reader is referred to the report for further details. This program employs the split-step Fourier (SSF) technique [21] to solve the PE for one-way propagating waves from a monotonic source. The SSF technique divides propagation over each distance increment through a heterogeneous sound-speed environment into step-by-step "free space" propagation through a medium having a fixed reference wave number, and periodically introduced (at each step) phase fluctuations consistent with departures from that fixed speed. The free space propagation is handled in the

wave number domain, and the phase anomalies are introduced in the spatial domain. Amplitude effects such as absorption are introduced with the phase anomalies. Thus, each step requires a 2-D Fourier transform and an inverse 2-D Fourier transform. Note that the wide angle variant of the propagation operator is used [22].

A. Sound Ducting—Source Inside Internal Wave Train

Fig. 11 shows images of mode ducting and dispersive refraction "leaking" created by the numerical model that are quite striking, as well as visually easy to interpret. We show two examples here at 100 and 200 Hz. In Fig. 11(a)–(e), we show a plan view of the depth-integrated total energy, the mode 1 energy, and the mode 2 energy, respectively, at 100 Hz. We see both trapping and leakage from the curved duct, as well as the initial escape of higher angle energy near the source. We also see that (filtered) mode 1 is not trapped by the curved waveguide, but leaks out the higher grazing angle side, as expected. However, mode 2 is trapped by the curved duct, in accordance with our theory which predicts that higher modes trap better.

We also see three other effects in Fig. 11(a)–(c). First, the mode 1 energy that escapes the duct is still tightly beamed, with an initial beamwidth on the order of the duct size (though susceptible to cylindrical spreading after that). Second, the trapped mode 1 energy shows distinct focusing/defocusing patterns within the horizontal duct. This is due to the horizontal modal interferences that occur. Finally, the overall curved wave produces some striking focusing (caustic) and shadow zones, which will be discussed later.

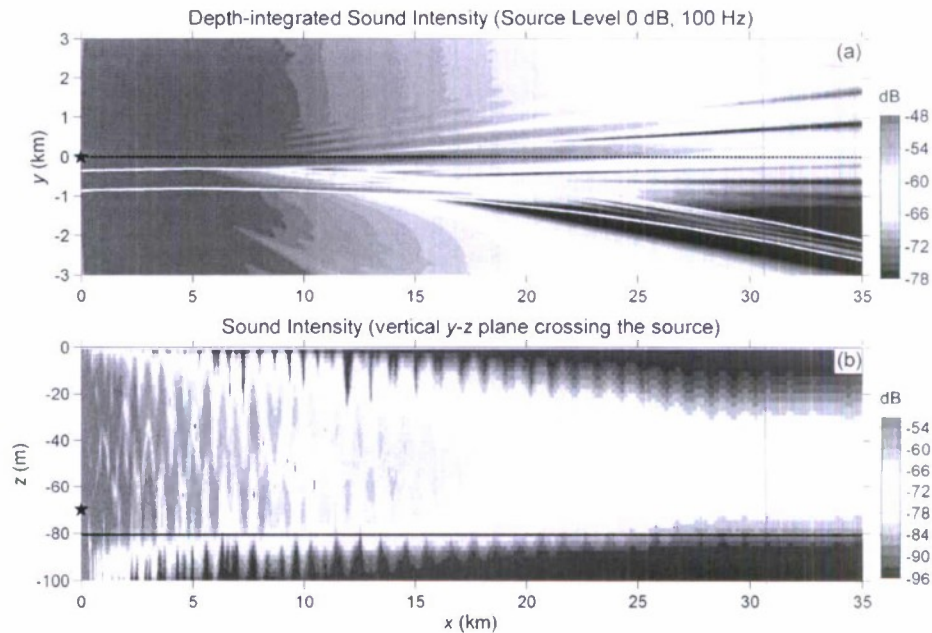


Fig. 14. Shadowing and horizontal Lloyd's mirror effects seen due to a curved nonlinear internal wave of 250-km radius. (a) Depth-integrated sound intensity at 100 Hz. (b) Vertical slice of sound intensity at $y = 0$ (all dB units are unity source level). Note that both shadowing and ducting are seen.

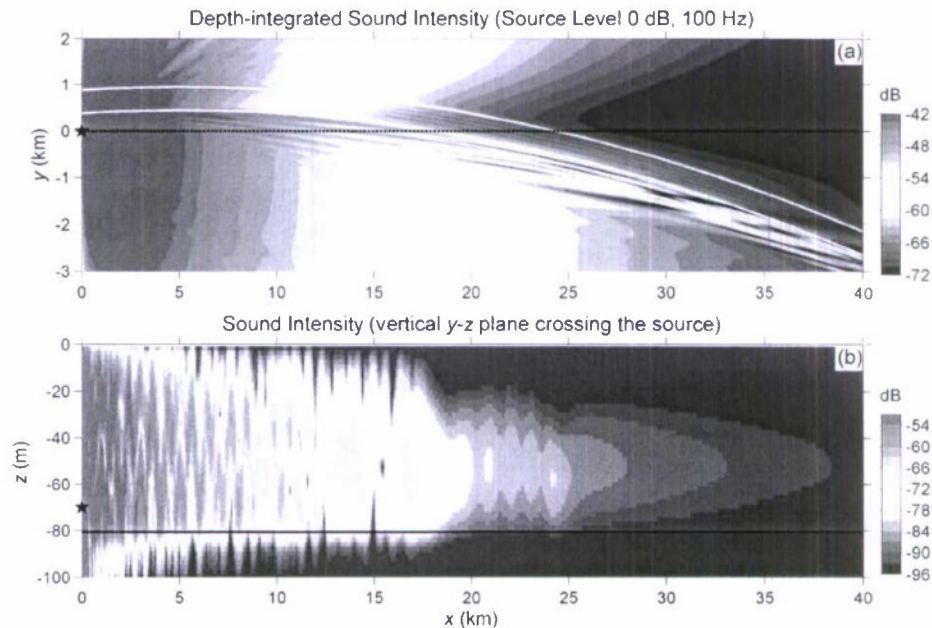


Fig. 15. Whispering gallery, duct penetration, and shadowing effects seen due to a curved nonlinear internal wave of 200-km radius. (a) Depth-integrated sound intensity energy at 100 Hz. (b) Vertical slice of sound intensity at $y = 0$ (all dB units are unity source level).

ference pattern in the upper portion of the figures, due to the interference of the direct and reflected waves, an effect called the "horizontal Lloyd's mirror" [19]. This shadowing of nearby sources might indeed be one of the major causes of amplitude fluctuations seen due to curved nonlinear internal waves. Fig. 14 shows both shadowing and ducting from an outside source.

C. Source Interior to Curved Internal Wave Train

In Fig. 15(a) and (b), we see a plan view and a side view, respectively, of the field due to a source placed on the interior of a curved internal wave field ($R = 40$ km). In the plan view [Fig. 15(a)], most of the acoustic energy through the internal

wave duct penetrates directly until 5-km range where it corresponds to very low grazing angles. At this range, the energy which is transmitted through the internal wave shows a slightly scalloped interference pattern due to internal reflections which are positively or negatively interfering depending on the relative path length across the duct.

The energy reflected on the interior side of the curved internal wave forms a whispering gallery effect. Moreover, we see the horizontal Lloyd's mirror effect again, as the direct and whispering gallery waves interfere. We also see a strong shadow zone in between the exterior and interior regions. Fig. 15(b) illustrates these effects in a vertical plane.

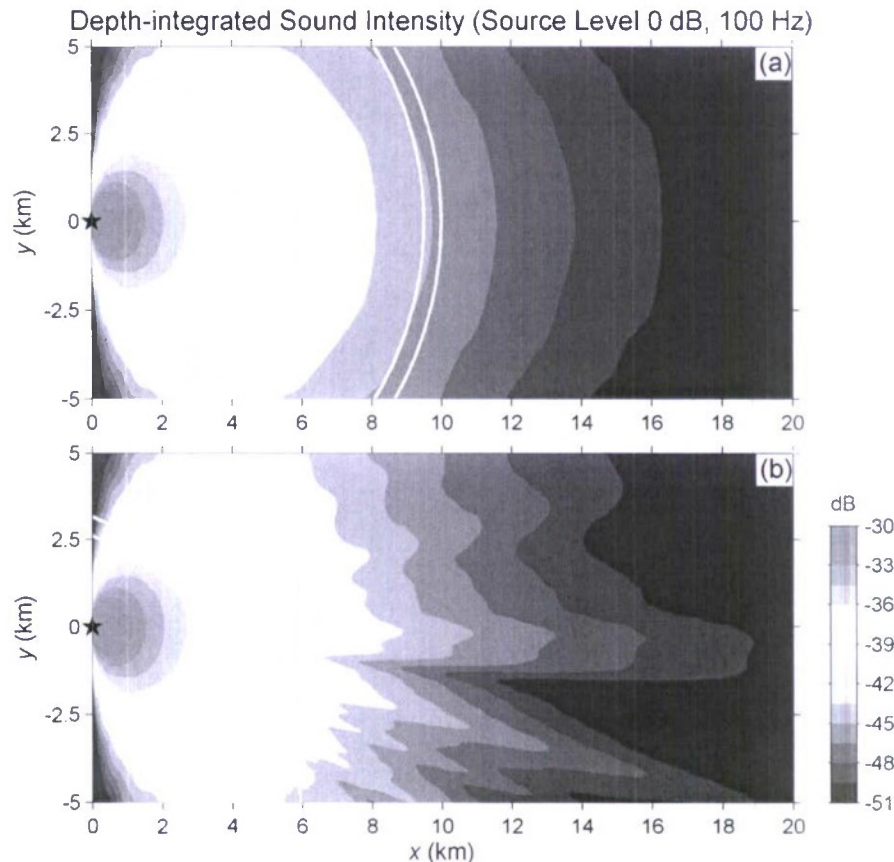


Fig. 16. Source distant from interior to an internal wave duct. (a) Control case showing the source at the center of the curved duct. (b) Energy penetration when the source is not at the center (all dB units are unity source level). The radius of the curved nonlinear internal wave is 10 km.

Fig. 16(a) and (b) shows a slightly different geometry for the “source interior to the internal wave” with the sound source placed more distant from the highly curved internal wave. In Fig. 16(a), we show a horizontal view of the source at the center of a circular internal wave, which is actually a control case. The sound energy should show circularly symmetric transmissions through the wave, which it does. In Fig. 16(b), we again see the slightly scalloped pattern of energy penetrating the internal wave duct, as before, but no interior whispering gallery rays—this is due to the grazing angles now being too high for subcritical angle total reflection to occur.

V. SW06 ARRIVAL ANGLES FIELD DATA

To verify that refractive effects occur when sound is transmitted along paths that are roughly parallel to curved (or straight) packets of nonlinear internal waves, we look at sound transmitted along such a path in SW06. Fig. 1 shows the geometry of this path with respect to a snapshot of wave activity. A source called “The Miami Sound Machine” transmitted 100-, 200-, 400-, 800-, and 1600-Hz phase encoded sequences as part of SW06, and we will consider its transmissions here. In particular, we will analyze the 200-Hz transmissions here, received at a joint horizontal line array (HLA) and vertical line array (VLA). The HLA was oriented close to north/south on the seafloor with the VLA at the southern end. Sound transmitted along this path was analyzed by Collis *et al.* [23] for horizontal

coherence study and further information on the experimental equipment can be found in that paper.

The center of the HLA was 19.2 km from the source. The bearing from the array center to the source was 26.2° . With this along-shelf path geometry, the major internal wave propagation direction across shelf was very nearly perpendicular to the acoustic track. If mean or time-dependent curvature of acoustic paths occurred and was significant, it would be evident as a deflection of the apparent source angle from 26.2° , as well as in intensity fluctuations. Because our paper focuses mainly on angular deflection, and because this should be a more direct indication of deflection effects than intensity fluctuations, we will look at angular wander using SW06 HLA time series of the heading of maximum array gain. We will then correlate this data against measurements of the internal wave at the receiver site to try to understand the angular fluctuations observed.

Fig. 17 shows both internal wave and acoustics data over a three-day time interval. The internal wave activity in Fig. 17(a) (more fully described below) and the acoustic fluctuations in Fig. 17(b)–(e) are visually correlated. The results presented in the panels will first be described in some detail, then they will be interpreted for ducting and scattering effects.

Fig. 17(a) contains a time series of the highpass filtered depth profile of vertical water velocity measured with an acoustic Doppler current profiler (ADCP) moored approximately midway between the source and the receiver. This time

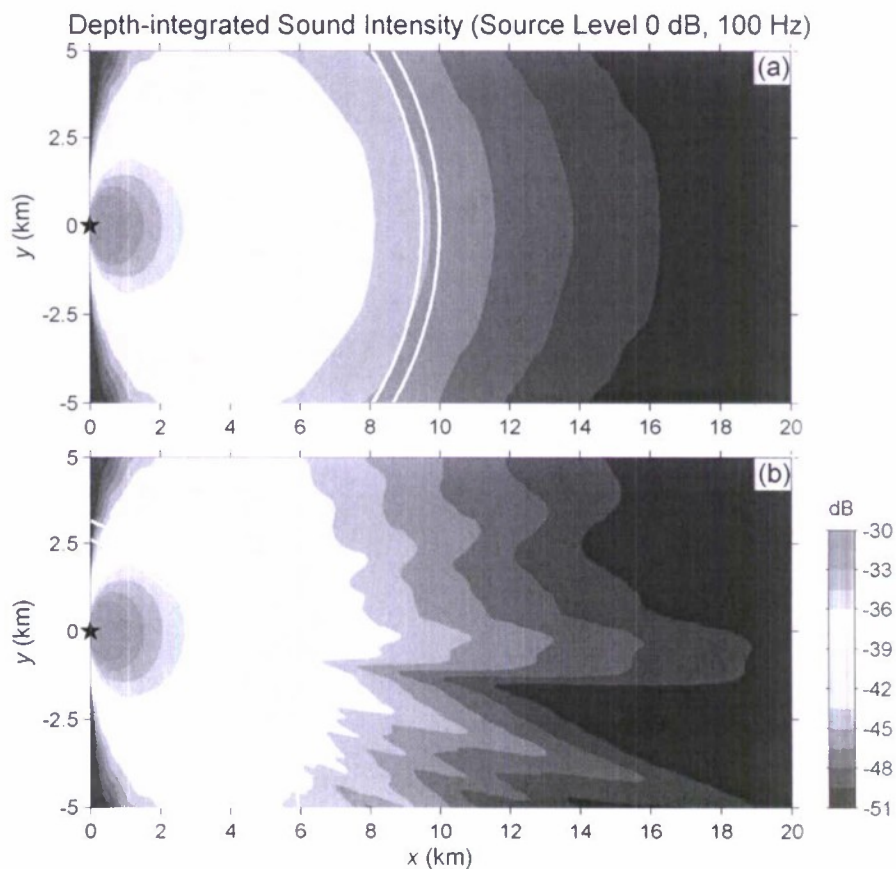


Fig. 16. Source distant from interior to an internal wave duct. (a) Control case showing the source at the center of the curved duct. (b) Energy penetration when the source is not at the center (all dB units are unity source level). The radius of the curved nonlinear internal wave is 10 km.

Fig. 16(a) and (b) shows a slightly different geometry for the “source interior to the internal wave” with the sound source placed more distant from the highly curved internal wave. In Fig. 16(a), we show a horizontal view of the source at the center of a circular internal wave, which is actually a control case. The sound energy should show circularly symmetric transmissions through the wave, which it does. In Fig. 16(b), we again see the slightly scalloped pattern of energy penetrating the internal wave duct, as before, but no interior whispering gallery rays—this is due to the grazing angles now being too high for subcritical angle total reflection to occur.

V. SW06 ARRIVAL ANGLES FIELD DATA

To verify that refractive effects occur when sound is transmitted along paths that are roughly parallel to curved (or straight) packets of nonlinear internal waves, we look at sound transmitted along such a path in SW06. Fig. 1 shows the geometry of this path with respect to a snapshot of wave activity. A source called “The Miami Sound Machine” transmitted 100-, 200-, 400-, 800-, and 1600-Hz phase encoded sequences as part of SW06, and we will consider its transmissions here. In particular, we will analyze the 200-Hz transmissions here, received at a joint horizontal line array (HLA) and vertical line array (VLA). The HLA was oriented close to north/south on the seafloor with the VLA at the southern end. Sound transmitted along this path was analyzed by Collis *et al.* [23] for horizontal

coherence study and further information on the experimental equipment can be found in that paper.

The center of the HLA was 19.2 km from the source. The bearing from the array center to the source was 26.2° . With this along-shelf path geometry, the major internal wave propagation direction across shelf was very nearly perpendicular to the acoustic track. If mean or time-dependent curvature of acoustic paths occurred and was significant, it would be evident as a deflection of the apparent source angle from 26.2° , as well as in intensity fluctuations. Because our paper focuses mainly on angular deflection, and because this should be a more direct indication of deflection effects than intensity fluctuations, we will look at angular wander using SW06 HLA time series of the heading of maximum array gain. We will then correlate this data against measurements of the internal wave at the receiver site to try to understand the angular fluctuations observed.

Fig. 17 shows both internal wave and acoustics data over a three-day time interval. The internal wave activity in Fig. 17(a) (more fully described below) and the acoustic fluctuations in Fig. 17(b)–(e) are visually correlated. The results presented in the panels will first be described in some detail, then they will be interpreted for ducting and scattering effects.

Fig. 17(a) contains a time series of the highpass filtered depth profile of vertical water velocity measured with an acoustic Doppler current profiler (ADCP) moored approximately midway between the source and the receiver. This time

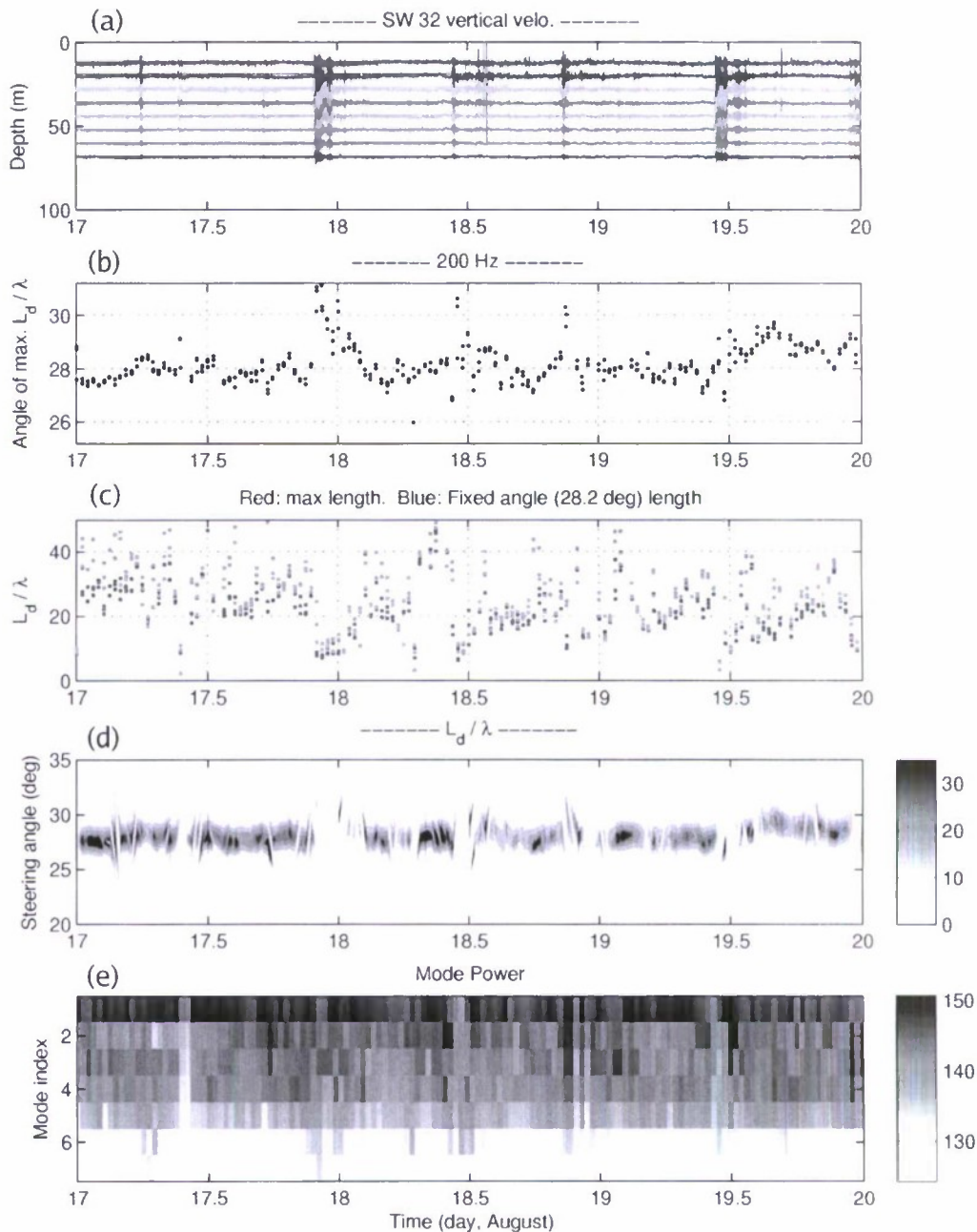


Fig. 17. (a) Highpass filtered vertical velocity time series, indicating times of large internal wave activity. (b) Angle which produces the largest horizontal correlation length of the acoustic signal along the array, a good proxy for angular deflection. (c) Horizontal correlation length along the array compared to the acoustic wavelength. (d) Normalized correlation length/acoustic wavelength. (e) Power in each of the received normal modes (dB re arbitrary reference).

series at representative depth bins clearly shows soliton packet activity, especially on days 18 and 19.5, which correspond to the spring tide phase of the tidal cycle. Moreover, the spacing between the tides shows a rough (on the average) M2 tidal period of 12.42 h, with some deviation, as noted by Colosi *et al.* [24]. This time series is rather typical of Mid-Atlantic Bight continental shelf internal wave data.

Fig. 17(d) is the master panel from which the results in Fig. 17(b) and (e) are obtained. The plotted values are the points where the spatially lagged correlation function of the complex matched-filter arrival waveforms falls to the value e^{-1} . The computation method is described in [23].

In Fig. 17(b), we see a time series of the steering angle yielding the longest horizontal correlation length along the receiving array (as a function of steering angle) of the arriving acoustic pulses. For each time, these values refer to the angles of maximum correlation length, shown as a function of steering angle in Fig. 17(d). This angle is a good proxy for the angular deflection that we wish to examine. Very interestingly, the angular deflections (from $\sim 27^\circ$ to $\sim 31^\circ$) seen during strong internal wave events are consistent with the 4.7° critical angle limit one would expect for ducting. Also, we note that on day 19.45 (before noon August 19, 2006), the array was actually moved along the seafloor by an internal wave packet, with the apparent bearing

to the source changing from 27.5° to 29° . It is critical that the departure of the array shape from rectilinear be included in the correlation length analysis; the shape changed significantly at the time of the strong wave packet, and a trend was introduced.

In Fig. 17(c), a time series of the maximum observed correlation length is shown, in units of an acoustic wavelength. Two values are shown for each analyzed pulse: the maximum value [from those computed over a wide range of steering angles, shown by color in Fig. 17(d)], and the value looking at one particular steering angle. It is seen that these numbers have an average of about 25 wavelengths, in good agreement with the work of Carey [25]. Also, during periods of strong internal wave activity, this correlation length decreases significantly, in agreement with what was found numerically by Finette and Oba [4] and previously found in the limited analysis of Collis *et al.* [23]. This lends further credence to the possibility that ducting was one of the mechanisms strongly affecting the acoustic signal.

In Fig. 17(e), we display the power in each of the received normal modes, obtained by mode filtering at the VLA located at the end of the HLA. Mode analysis procedures are described in [23]. This plot shows that internal wave events are generally accompanied by evidence of mode coupling, i.e., some energy is lost by mode 1 and is coupled into the higher order modes. As mode ducting is an adiabatic effect, this shows that some of the energy is crossing the internal wave crests above the critical grazing angle. This is not surprising in that the internal waves seen in SW06, while propagating in the mean approximately perpendicular to the acoustic track, have a directional spectrum that has an angular spread of a few tens of degrees (which includes curvature effects), as shown in Fig. 4. Thus, when the internal wave packets cross between the source and the receiver, the acoustic track can often be at above the critical grazing angle. As an example, a curved wave with diameter less than or equal to the source–receiver distance R is not an unlikely case for our SW06 data, as $R \sim 20$ km, and the SAR images show many curved internal wave trains of this diameter or smaller. When such a wave propagates between the source and the receiver, some mode coupling will occur. This situation of concurrent refraction and mode coupling causes complications when applying adiabatic mode methods [26] and coupled mode methods [27].

A scenario begins to emerge from the data and theory, and we now present a “first-order guess” as to what the data indicate. To begin with, as suggested by our theory and the data, it seems unlikely that strongly curved internal waves are ducting energy to the receiver at high angles compared to the bearing to the source. Both the modal energetics (coupling) and the relatively narrow directional spectrum of the internal waves seem contrary to that possibility in SW06. Moreover, large angular deflections are rarely seen in the acoustic data, and are more easily ascribed to mode coupling. (Since our array is not broadside to the source, mode coupling can produce this angular effect because of the vertical/horizontal phase trend ambiguity.) Second, looking at the angular deflection data combined with the correlation length data, it is likely that some ducting is occurring along the path. This duct can be: 1) a straight line duct, 2) a weakly curved duct, or 3) a truncated duct [14] and still produce very similar effects, i.e., wobble of the apparent source direction by up to $\pm\theta_{\text{crit}}$ and large amplitude fluctuations. Third and finally, there

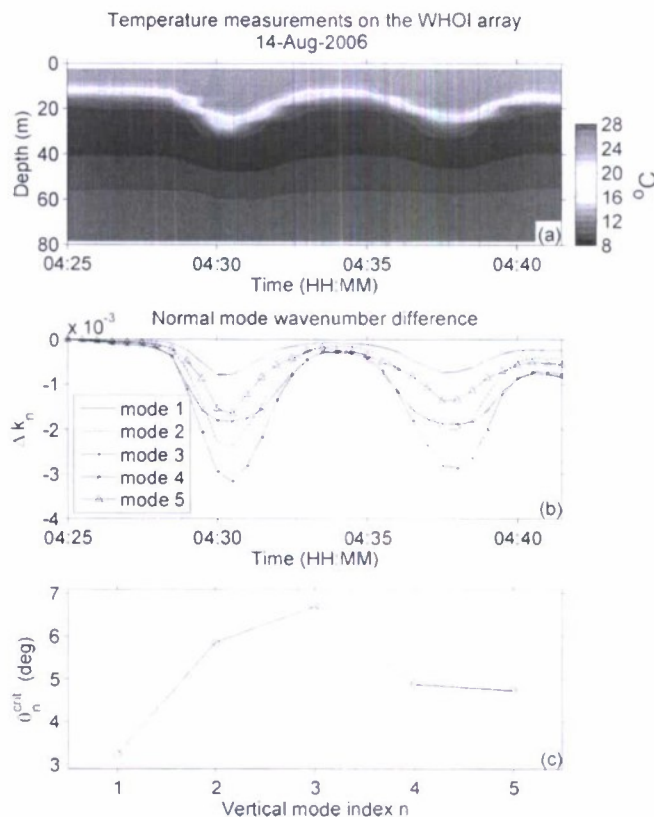


Fig. 18. (a) Internal wave event during SW06. (b) Perturbation of the acoustic mode wave number to the background state at 100 Hz. (c) Critical angle as a function of mode number.

is evidence of time-variable mode coupling in the data, as seen by both the mode amplitude time series and also from the fact that some occasional large angle deflections are seen, which are not due to curved wave ducting (from our previous arguments.) This coupling is likely due to incidence angles upon the internal waves above critical grazing angle, which is supported by the directional spectrum spread of the internal waves.

This scenario is consistent with our data, but we will not claim that it is conclusive proof, as there could be other explanations for the data (though we do not readily see such others.) We think that combining a directional spectrum of nonlinear internal waves, including curved and truncated waves, which induces both ducting and coupling effects, can produce a rather large variety of data effects and that the SW06 data set is just a beginning look at this rich area.

Before leaving the data analysis section, we will consider one more aspect of the SW06 experimental data which is relevant to this analysis, namely, the oceanographic data for the water column and bottom sound-speed profiles. These data show a large variation in the sizes, shapes, and strengths of the nonlinear internal waves, and also show that the bottom is significantly penetrable to sound. These two effects will change the background normal modes from what was used in Section III, as well as the perturbations of those modes by the internal waves. To show how a more realistic profile affects the critical angle calculations presented in (10), we look at a “typical” internal wave duct from SW06 [Fig. 18(a)], and calculate the modes at

100 Hz, their eigenvalue perturbations from the background profile, and the critical angle versus mode number that one sees using the realistic profiles.

Doing this calculation, one obtains the results seen in Fig. 18(b) and (c). In Fig. 18(b), we show the eigenvalue perturbation as a function of time due to a real internal wave. We see that the perturbation time series follows the wave transit for each mode, as expected. More interesting is the critical angle for each mode, shown in Fig. 18(c), which varies from 3.2° to 6.8° . This is somewhat more variability in angle than seen in our "canonical waveguide" example, though the average number is about the same. Also, we see that the critical angle increases for the first three modes, but then decreases and flattens out (to about 4.8°) for modes 4 and 5. This is likely due to these higher modes most strongly feeling the effect of the penetrable bottom, which the low modes do not.

Thus, we see that for an exact description of the ducting effects, the more realistic ocean and bottom models should be considered. Also, this last calculation used a "typical" nonlinear internal wave from SW06, but it is well known that the internal waves vary even within a wave train, as well as with space and time. The bottom also varies spatially. Thus, it would not be amiss to eventually consider a more statistical look at the ducting behavior of the modes in shallow-water internal waves. This will be pursued in a future paper.

VI. CONCLUSION AND FUTURE DIRECTIONS

In concluding this paper, we will look at the three viewpoints that we examined the ducting effects from, i.e., theory, numerical models, and experimental data. We will briefly state what we have accomplished, but more importantly, examine what yet needs to be done to fully understand curved wave ducting phenomena. This is a rich area, and has more depth than one paper could cover.

Regarding theory, we have endeavored to show, in the context of simple perturbation theory and a canonical ocean model, how the physics of trapping and leaking of acoustic energy from curved nonlinear internal waves works. In terms of things that still need more work, we would point to two items. First, there are the "whispering gallery" modes, in which the sound interacts only with the exterior walls. Second, there is theory that should be developed for full wave trains, not just the "single duct" that we considered in the paper. Wave trains, which have (for instance) rank ordering in size, can show additional trapping and leaking effects in addition to the (basic) case that we showed in this paper.

In terms of numerical models, we have been able to show rather clearly the acoustic effects of single ducts, to match the theory we presented here. However, the models can handle more complex environments, and that is where we should be going with them. In addition to wave trains (as mentioned above), we should also be looking at realistic 3-D internal wave fields based on data. This would allow us to get at the scattering statistics (for intensity, arrival angle, etc.) that we will see in the data.

As to data, the SW06 data were able to give us a very good look at the oceanography of the curved internal waves, so that we can create very good input for the acoustics calculations. The acoustics data, while unique and showing some of the effects we discussed in this paper, were not adequate to unambiguously describe all of the effects we discussed. This is for the simple reason that the experiment was not designed completely around the goals of this paper: the horizontal/vertical array had many other purposes to accomplish. Thus, we did not have the array completely broadside to the acoustic path (which would have made the angular deflection signal unambiguous, even in the presence of mode coupling), nor did we concentrate all our oceanography measurements along the acoustic track we discussed. We also could have placed point receivers to look at shadowing effects, etc. These are things that we might consider doing in future experiments.

ACKNOWLEDGMENT

The authors would like to thank H. Graber and N. Williams for providing them with the SAR satellite images they used for this study, and G. Gawarkiewicz for the coastal oceanography input to this paper. They would also like to thank the WHOI SW06 deployment/recovery team, along with the captains and crews of the *R/V Knorr*, the *R/V Oceanus*, and the *R/V Endeavor*.

REFERENCES

- [1] J. Zhou, X. Zhang, and P. H. Rogers, "Resonant interaction of sound wave with internal solitons in the coastal zone," *J. Acoust. Soc. Amer.*, vol. 90, pp. 2042–2054, 1991.
- [2] J. R. Apel, M. Badié, C.-S. Chiu, S. Finette, R. Headrick, J. Kemp, J. F. Lynch, A. Newhall, M. H. Orr, B. H. Pasewark, D. Tielburger, A. Turgut, K. von der Heydt, and S. Wolf, "An overview of the 1995 SWARM shallow-water internal wave acoustic scattering experiment," *IEEE J. Ocean. Eng.*, vol. 22, no. 3, pp. 465–500, Jul. 1997.
- [3] M. Badié, Y. Mu, J. F. Lynch, J. R. Apel, and S. N. Wolf, "Temporal and azimuthal dependence of sound propagation in shallow water with internal waves," *IEEE J. Ocean. Eng.*, vol. 27, no. 1, pp. 117–129, Jan. 2002.
- [4] S. Finette and R. Oba, "Horizontal array beamforming in an azimuthally anisotropic internal wave field," *J. Acoust. Soc. Amer.*, vol. 114, pp. 131–131, 2003.
- [5] B. G. Katznelson and S. A. Pereselkov, "Low-frequency horizontal acoustic refraction caused by internal wave solitons in a shallow sea," *Acoust. Phys.*, vol. 46, pp. 684–691, 2000.
- [6] D. J. Tang, J. F. Lynch, J. N. Moum, P. Abbot, N. R. Chapman, P. H. Dahl, T. F. Duda, G. G. Gawarkiewicz, S. Glenn, J. A. Goff, H. Graber, J. N. Kemp, A. R. Maffei, J. D. Nash, and A. E. Newhall, "Shallow Water '06: A joint acoustic propagation/nonlinear internal wave physics experiment," *Oceanography*, vol. 20, no. 4, pp. 156–167, Dec. 2007.
- [7] R. Burridge and H. Weinberg, "Horizontal rays and vertical modes," in *Wave Propagation and Underwater Acoustics*, J. B. Keller and J. S. Papadakis, Eds. Berlin, Germany: Springer-Verlag, 1977, pp. 86–152.
- [8] T. F. Duda, J. F. Lynch, Y. T. Lin, A. E. Newhall, H. Graber, and M. Caruso, "The effects of non-linear internal wave curvature on acoustic propagation," *J. Acoust. Soc. Amer.*, vol. 123, p. 3588, 2008.
- [9] J. D. Irish, J. F. Lynch, J. N. Kemp, T. D. Duda, and A. E. Newhall, "A moored array for measuring internal solitary waves during Shallow Water '06," in *Proc. IEEE/MTS OCEANS Conf.*, Vancouver, BC, Canada, Oct. 2007, DOI: 10.1109/OCEANS.2007.4449170.
- [10] C. C. Boughan and W. Siegmund, *Private Communication* 2008.
- [11] Y. Matsumura and H. Hasumi, "A non-hydrostatic ocean model with a scalable multigrid Poisson solver," *Ocean Model.*, vol. 24, pp. 15–28, 2008.
- [12] C. Y. Shen, T. E. Evans, R. M. Oba, and S. Finette, "Three dimensional hindcast simulation of internal soliton propagation in the Asian Seas International Acoustics Experiment area," *J. Geophys. Res.*, vol. 114, no. C1, p. C01014, 2009.
- [13] J. F. Lynch, T. F. Duda, Y. T. Lin, A. E. Newhall, and P. F. J. Lermusiaux, "A model for four-dimensional coastal internal waves with applications to acoustics," *J. Acoust. Soc. Amer.*, vol. 126, p. 2305, Oct. 2009.
- [14] Y. T. Lin, T. F. Duda, and J. F. Lynch, "Acoustic mode radiation from the termination of a nonlinear internal gravity wave duct in a shallow ocean area," *J. Acoust. Soc. Amer.*, vol. 126, no. 4, pp. 1752–1765, Oct. 2009.

- [15] T. F. Duda, "Acoustic mode coupling by nonlinear internal wave packets in a shelfbreak front area," *IEEE J. Ocean. Eng.*, vol. 29, no. 1, pp. 118–125, Jan. 2004.
- [16] T. F. Duda and J. Preisig, "A modeling study of acoustic propagation through shallow-water solitary wave packets," *IEEE J. Ocean. Eng.*, vol. 24, no. 1, pp. 16–32, Jan. 1999.
- [17] B. G. Katsnelson and V. G. Petnikov, *Shallow-Water Acoustics*, ser. Books in Geophysical Sciences. New York: Springer-Verlag, 2002, ch. 3.
- [18] E. Hecht and A. Zajac, *Optics*. Reading, MA: Addison-Wesley, 1976, ch. 5.
- [19] J. F. Lynch, J. Colosi, G. Gawarkiewicz, M. Badiey, B. Katsnelson, J. Miller, W. Siegmann, C. Chiu, and A. Newhall, "Consideration of fine-scale coastal oceanography and 3-D acoustics effects for the ESME sound exposure model," *IEEE J. Ocean. Eng.*, vol. 31, no. 1, pp. 33–48, Jan. 2006.
- [20] T. F. Duda, "Initial results from a Cartesian three-dimensional parabolic equation acoustical propagation code," Woods Hole Oceanogr. Inst., Woods Hole, MA, Tech. Rep. WHOI-2006-041, 2006.
- [21] R. H. Hardin and F. D. Tappert, "Applications of the split-step Fourier method to the numerical solution of nonlinear and variable coefficient wave equations," *SIAM Rev.*, vol. 15, pp. 423–423, 1973.
- [22] D. J. Thomson and N. R. Chapman, "A wide-angle split-step algorithm for the parabolic equation," *J. Acoust. Soc. Amer.*, vol. 74, pp. 1848–1854, 1983.
- [23] J. M. Collis, T. F. Duda, J. F. Lynch, and H. A. Deferrari, "Observed limiting cases of horizontal field coherence and array performance in a time-varying internal wavefield," *J. Acoust. Soc. Amer.*, vol. 124, pp. EL97–EL103, 2008.
- [24] J. A. Colosi, J. F. Lynch, R. C. Beardsley, G. Gawarkiewicz, C.-S. Chiu, and A. Scotti, "Observations of nonlinear internal waves on the outer New England continental shelf during the summer Shelfbreak PRIMER," *J. Geophys. Res.*, vol. 106, pp. 9587–9601, 2001.
- [25] W. Carey, "The determination of signal coherence length based on signal coherence and gain measurements in deep and shallow water," *J. Acoust. Soc. Amer.*, vol. 104, pp. 831–837, 1998.
- [26] T. F. Duda, "Examining the validity of approximations to fully three-dimensional shallow-water acoustic propagation through nonlinear gravity waves," in *Proc. OCEANS Conf.*, 2007, DOI: 10.1109/OCEANSE.2007.4302333.
- [27] J. C. Preisig and T. F. Duda, "Coupled acoustic mode propagation through continental shelf internal solitary waves," *IEEE J. Ocean. Eng.*, vol. 22, no. 2, pp. 256–269, Apr. 1997.



James F. Lynch (M'96–SM'02–F'05)

He received the B.S. degree in physics from Stevens Institute of Technology, Hoboken, NJ, in 1972 and the Ph.D. degree in physics from the University of Texas at Austin, Austin, in 1978.

He then worked for three years at the Applied Research Laboratories, University of Texas at Austin (ARL/UT) from 1978 to 1981, after which he joined the scientific staff at the Woods Hole Oceanographic Institution (WHOI), Woods Hole, MA. He has

worked at WHOI since then, and currently holds the position of Senior Scientist in the Applied Ocean Physics and Engineering Department. His research specialty areas are ocean acoustics and acoustical oceanography, but he also greatly enjoys occasional forays into physical oceanography, marine geology, and marine biology.

Dr. Lynch is a Fellow of the Acoustical Society of America, the former Editor-in-Chief of the *IEEE JOURNAL OF OCEANIC ENGINEERING* and recent chairman of the Applied Ocean Physics and Engineering Department at WHOI.



Ying-Tsong Lin (M'10) received the B.S. degree in hydraulic and ocean engineering from National Cheng Kung University, Tainan, Taiwan, in 1996 and the M.S. degree in naval architecture and ocean engineering and the Ph.D. degree in engineering science and ocean engineering from National Taiwan University (NTU), Taipei, Taiwan, in 1998 and 2004, respectively.

From 2002 to 2003, he was a Guest Investigator at the Applied Ocean Physics & Engineering (AOP&E) Department, Woods Hole Oceanographic Institution (WHOI), Woods Hole, MA. After receiving his Ph.D. degree, he began a half-year postdoctoral appointment at Underwater Acoustics Laboratory, NTU, after which he worked at WHOI as a Postdoctoral Researcher. He currently holds the position of Assistant Scientist at the AOP&E Department, WHOI. His research interests include shallow-water acoustic propagation, acoustical oceanography, geoacoustic inversion, and underwater sound source localization.

Dr. Lin is a member of the IEEE Oceanic Engineering Society and the Acoustical Society of America.

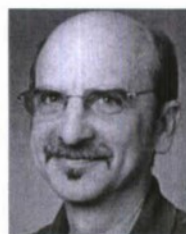


Timothy F. Duda (M'05–SM'09) received the B.A. degree in physics from Pomona College, Claremont, CA, in 1979 and the Ph.D. degree in oceanography from the Scripps Institution of Oceanography, University of California, San Diego, in 1986.

He worked at the University of California, Santa Cruz, from 1986 to 1991. He has been a Scientist at the Woods Hole Oceanographic Institution (WHOI), Woods Hole, MA, since 1991. His three primary fields of study are ocean acoustic propagation, ocean internal gravity waves, and ocean mixing processes.

His research has included physical process studies, development of new measurement tools, and computational acoustic modeling.

Dr. Duda is a member of the IEEE Oceanic Engineering Society. He is also a member of the American Meteorological Society, the American Geophysical Union, and the Acoustical Society of America.



Arthur E. Newhall (M'07) received the B.S. degree in mathematics from the University of Maine at Orono, Orono, in 1985.

He is a Research Specialist at the Applied Ocean Physics and Engineering Department, Woods Hole Oceanographic Institution (WHOI), Woods Hole, MA. His current interests include ocean acoustic propagation modeling, acoustical oceanography, software engineering, and music.

Mr. Newhall is a member of the IEEE Oceanic Engineering Society and the Acoustical Society of

America.